Impact of ocean waves on deep waters mixing and large-scale circulation

Oceane Tess Richet

NNT : 2017SACLX082

THESE DE DOCTORAT
DE L'UNIVERSITE PARIS-SACLAY

préparée à

L'ÉCOLE POLYTECHNIQUE

Laboratoire d'hydrodynamique de l'Ecole polytechnique

ÉCOLE DOCTORALE N°579
Sciences Mécaniques et Energétiques, Matériaux et Géosciences (SMEMaG)

Spécialité de doctorat : Mécanique des fluides

par

Océane Richet

Impact of ocean waves on deep waters mixing and large-scale circulation.

Thèse présentée et soutenue à Paris, le 06 Décembre 2017.

Après avis des rapporteurs :

Chantal Staquet	(LEGI)
Sonya Legg	(GFDL - Princeton University)

Composition du jury :

Pascale Bouruet-Aubertot	(LOCEAN)	Présidente du jury
Chantal Staquet	(LEGI)	Rapportrice
Sonya Legg	(GFDL)	Rapportrice
Jean-Marc Chomaz	(LADHYX)	Directeur de thèse
Caroline Muller	(LMD-ENS)	Co-directrice de thèse
Sabine Ortiz	(IMSIA)	Examinatrice
Gurvan Madec	(LOCEAN)	Examinateur

Doctoral thesis

Impact of ocean waves on deep waters mixing and large-scale circulation

prepared by

Océane Richet

under the supervision of

Caroline Muller and Jean-Marc Chomaz

Academic year 2017 - 2018

To my grand-father Henri,
For our long conversations at breakfast.

Remerciements

Je ne peux que commencer par vous remercier Caroline et Jean-Marc. Sans vous rien de tout cela n'aurait eu lieu. Merci de m'avoir donnée ma chance. Et puis commencer une thèse par un entretien dans un café ça ne présageait qu'une bonne ambiance (de travail) ! J'ai adoré travailler avec vous deux. A tous les 3 on forme une bonne équipe ! C'était très enrichissant d'avoir vos deux points de vue. Vous m'avez également donnée la possibilité de vraiment découvrir le monde de la recherche au travers de toutes les conférences, des échanges avec d'autres labo, des écoles d'été et tout simplement au travers vos propres expériences. J'espère qu'on aura encore l'occasion de travailler ensemble, ou juste d'aller boire un verre de temps en temps !

Bêêêêêêêêêh !!!!! Bêêêêêh !!!!! Baaaaalle !!!! Bêêêêêh !!!!! Balle aléatoiiiiiiire !!!! Voilà ce qui se cache derrière la porte du bureau invisible ! Une bonne thèse ne va jamais sans de géniaux cobureaux ! Merci Gaétan de m'avoir fait visité le Ladhyx pour me convaincre de venir. Finalement, tout s'est joué lors du lâché de ballon devant le labo ! Merci aussi d'avoir fait irruption dans le bureau pour la fin de ta thèse, tu as bien élevé le niveau des conversations au son de tes bêêêêêêh ! Merci Julien et Tristan d'avoir été mes premiers cobureaux pour entamer cette longue épreuve au milieu de tous ces X et au bout du monde. Merci Guillaume et Elizabeth pour vos sacrées Munstiflettes et Tartiflettes ! Je retiendrai les lardons cuits au beurre. Merci Léopold pour avoir toujours envie de jouer à la balle et de veiller à ce qu'on ait notre quota de sport par jour ! Merci Vincent pour avoir remplacé Guillaume même si on ne sait toujours pas si tu es un espion du préfa ou si tu as fini par prêter allégeance aux numériciens. Merci Tristan pour avoir été souvent partant pour me suivre dans mes weekends rando improvisés et finalement revenir plus fatigués qu'avant le weekend. Sans toi je me serai sentie un peu seule comme lève tard et comme profiteuse de grands weekends. Il te reste une mission : prendre soin de Charlotte en espérant qu'un jour elle refleurisse! Je rajouterai merci Eunok pour tes passages furtifs dans le bureau. Merci pour ces weekends au soleil à regarder les poulpes. Et oui, un jour on aura notre château plein de chats sur la corniche à Marseille !

Bien sûr, je n'oublie pas toutes les autres personnes du ladhyx que je remercie. Vous avez tous participé à cette super ambiance au labo. Notamment le préfa avec toutes vos inventions un peu folles mais toujours super utiles. D'ailleurs j'espère bien un jour goûter à une de vos pizzas ! merci aux personnes de "l'autre bâtiment" d'avoir répondu à mes quelques invitations pour réunir tous les thésards du labo autour d'un bon repas au resto ! En tout cas, je ne pouvais pas rêvé plus enrichissant que d'être dans un labo aussi diversifié.

Mes petits chats, merci de m'avoir fait une place dans votre bureaux ! Vous êtes les meilleurs cobureaux pour finir une thèse !!!! Tout autre ambiance que celle au ladhyx mais tout aussi sympathique ! A vous, monsieur Perrot et monsieur Laxenaire. Merci aussi à Claire qui a tenté de me motiver à aller faire du sport. Bon on n'a pas été super efficaces mais la volonté était là !

Raphaela, that was so nice to meet you at the MIT. I loved the time I spend with you to listen classic music, to discover Boston and our long chats under the sun! I remember our cycling

trip, the snake on the road and the well-diserved hot chocolate at the end! You illuminated my time in Boston. Qi, you was the best roomate ever but also my favorite big sister! You are petite but so funny!!!! I enjoyed our girl talks and to discover China through you! You are a great chef! Thank you to teach me how to cook your famous dumpling!

Et puis, il y a vous tous, mes petites cacahuètes, ma famille de substitution depuis toutes ces années : Valérie (cacahuète number one), Anne So, Chlochlo, Miloune, Stefan, Anaïs, Mot Mot, Marthouille, Clara, Rafiki ! On en a partagé des choses entre nos diners de retour de vacances et de Noël, les soirées jeux et les aventures dans lesquelles je vous ai souvent entrainés ! Cacahuète, Anne So, Chlochlo, Anaïs et Mimi, heureusement que vous étiez là quand j'étais toute tapata, comment est-ce que j'aurais pu survivre sans vous ?! Cacahuète, j'espère que dans 10 ans et même plus encore on arrivera à se retrouver pour nos goûter blabla à la Jacobine ! Anne So, je compte sur toi pour toujours avoir une bonne bière au frais au cas où je débarquerai. Au pire on ira pécher des crocodiles ! Chlochlo, que dire à part qu'on a vaincu la monté de la mort ensemble, les sapins et les bouquetins s'en souviennent encore ! Anaïs, mini cacahuète à l'emploi du temps de ministre, n'oublies pas que l'on doit toujours partir en vacances ensemble ! En attendant je suis très fière de te prêter mon anniversaire pour ta soutenance ! Ma Miloune d'amour, j'ai tellement de choses à raconter, au moins de quoi écrire une nouvelle thèse ! En même temps ça fait 12 ans que l'on parle de nourriture, ça n'est pas rien ! Mot Mot, à nos conversations jusqu'au petit matin à finir toutes ces bonnes bières alors que tout le monde a déserté depuis un bout de temps ! Clairement le temps n'avance pas pareil entre minuit et 6h du matin ! Tu as toujours été là pour écouter mes histoires. Marthouille, ma petite Marthemotte, promis la prochaine fois je te ferai une rando avec juste des plats et des descentes ! Clara, heureusement que tu étais là pour programmer et organiser nos soirées jeux et diners ! Ça représente plein de souvenirs mais au jour le jour, dans une thèse, ces moments passés avec vous sont des grandes bouffées d'air et de fous rire ! Une thèse ce n'est rien si on n'a pas les amis qui vont avec, le reste du temps !

Doubi, merci de m'avoir supportée tout ce temps et surtout merci de continuer à être là pour moi. Tu es souvent mon sauveur lors de mes petites galères de thèse ! Tout ça compte énormément pour moi et j'espère que j'arrive à te rendre la pareille !

Un grand merci à toute ma famille qui est derrière moi depuis toutes mes années étudiantes. Votre soutien a été indispensable dans ce travail de longue haleine même si je sais que pour la plus part d'entre vous je parle chinois et que ma vie ressemble plus à carnet de voyage ! Je vous dois beaucoup pour en être arrivée jusque là ! Je vous remercie d'être toujours présents même quand je suis au bout du monde (ce qui arrive finalement plus souvent que prévu) !

Tilili ! Tilili ! Tililiiiiiiiiii !!!!!!! TILILILILILILILILILILILILILILILILI

(\ (\
(-.-)
O_(")(") Pine.

Contents

Preamble

Bill Watterson, 23 July 1987

In the context of global warming, the ocean is the main receptacle having absorbed more than 90 % of the anthropogenic energy surplus. The effects induced by the warming become detectable and impact the structure of the ocean, its circulation as well as atmospheric [Lambaerts et al. 2013] and oceanic ecosytems [Villar et al. 2015]. A better understanding of the local and global oceanic circulation will permit to improve the predictions from global climate models.

To gain better fundamental understanding of the ocean, it is natural to begin by describing the **structure of the ocean** and to introduce the **concept of water mass**. This vision of the ocean is a schematic vision of the ocean used by oceanographers to understand the exchanges between the different basins. A brief description of the two principal water masses relevant for this study is given in chapter 1.

This project encompasses oceanic motions at very different time scales. These include slow time scale of the thermohaline circulation, a quasi static vision of the ocean. Other faster processes, like winds, tides or waves, play an important role in maintaining the overturning circulation. A description of the diverse **theories for the global overturning circulation** is given in chapter 1, allowing to introduce

the role of waves in maintaining and modulating the oceanic circulation.

At this point, a physical description of the **oceanic waves**, involved in the studies presented in this thesis, is salutary for the rest of the manuscript. The end of chapter 1 thus details the specific conditions for the development of internal waves and more specifically of internal tides, Kelvin waves and topographic Rossby waves, and their principal characteristics.

This introduction to the global context of the study is followed in chapter 2 by a first study on the **mechanisms leading to the dissipation of the internal tides** (also called baroclinic tide) in an idealized ocean. Internal tides are internal waves at the tidal frequency generated by the action of the barotropic tide in a stratified fluid. In this study, we focus on the semi-diurnal lunar tide (M2) interacting with a sinusoidal topography in a 2D high resolution numerical model. This study has been submitted for publication in the *Journal of Geophysical Research: Oceans*.

Once the mechanisms behind the dissipation of internal tides are clarified, we study in chapter 3 the **effect of a background mean current** like mesoscale eddies or large-scale currents, **on the latitudinal distribution of internal tide energy dissipation**. Using a 2D numerical model and, a realistic or an idealized rough topography, we impose a weak mean current which does not affect the generation of internal tides. The results of this study have been published in the *Journal of Physical Oceanography*.

The last chapter is part of an ongoing research project developed at the *Geophysical Fluid Dynamics summer school (Woods Hole)* in collaboration with Renske Gelderloos, Larry Pratt and Jiayan Yang. The problem of water export from a marginal sea toward open ocean is well known in oceanography. In this study, we propose to investigate **how upstream disturbances influence the upstream circulation of a hydraulically controlled sill** in a 1.5-layer reduced gravity model. This study is still in preparation and will be published in the near future.

The last chapter summarizes the key results of this thesis, and provides a discussion of ongoing and future work.

1

Introduction

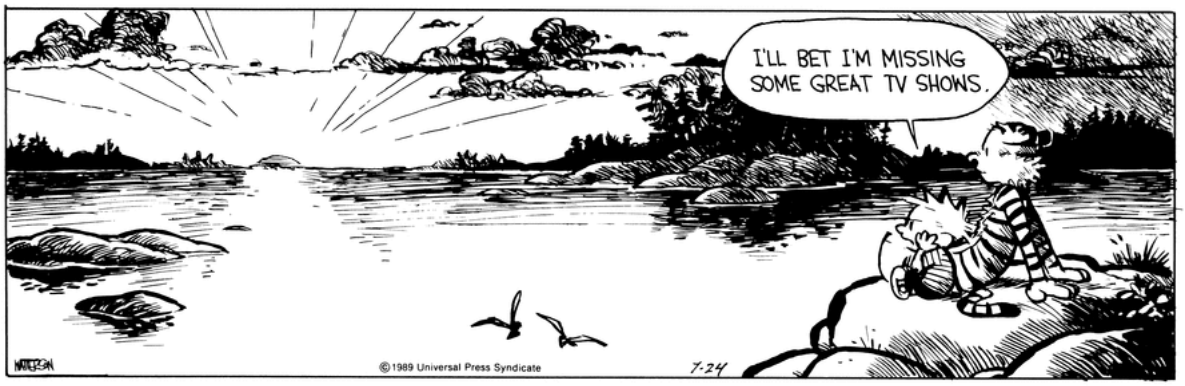

Bill Watterson, 24 July 1987

1.1 Ocean water masses: description

The ocean is something that most of people know and have experienced someday at the beach. The first contact teaches, right away, that the ocean is a salty fluid with a varying temperature: warmer at the surface and colder at depth. Once the swim is over, it has happened to many of us, wistfully gazing out the ocean, to realize how vast and unknown it is.

To improve our common vision of the ocean, most of the time restricted to the coast, oceanographers do measurements all over the world revealing what is under the surface. Through the measurements of temperature, salinity, oxygen and other tracers, they give a global vision of the time varying structure of the ocean.

1.1.1 The oceanographers' view

The ocean is a stratified fluid whose density varies with temperature and salinity of the fluid. The densest fluids (cold and salty) fill the bottom and lightest fluids (fresh and warm) are at the surface. A variation of temperature can be induced, for example, by interaction with atmosphere or geothermal fluxes. On the other hand, salinity varies with precipitation/evaporation, fresh water from rivers or formation/melting of sea ice. The different forcings correspond globally to the thermohaline forcing.

These processes are not homogeneous in space and time, which induces variations of temperature and salinity, and thus density in the ocean. In order to understand the structure of the ocean, oceanographers develop the concept of water masses. A water mass is an identifiable body of water with a common formation history whose physical properties (temperature and salinity, among others) are distinct from surrounding water. Each water mass has a name reflecting its origin and its depth location. Commonly in oceanography, we use their acronyms and the first summary and review is given by [Emery and Meincke 1986]. We first restrict the discussion to the Atlantic basin, before moving on to the circulation between four connected basins.

Figure 1.1 shows the same meridional section of the Atlantic for potential temperature [1], salinity and neutral density[2]. In these figures, we can easily identify

[1] **Potential temperature:** temperature of a water parcel that it would acquire if adiabatically brought to a standard reference pressure.

[2] **Neutral density** is a variable commonly used in oceanography to identify water mass. In fact, a neutral density surface is the surface along which a given water mass will move, remaining neutrally buoyant. The neutral density is a function of temperature, salinity pressure and time. It

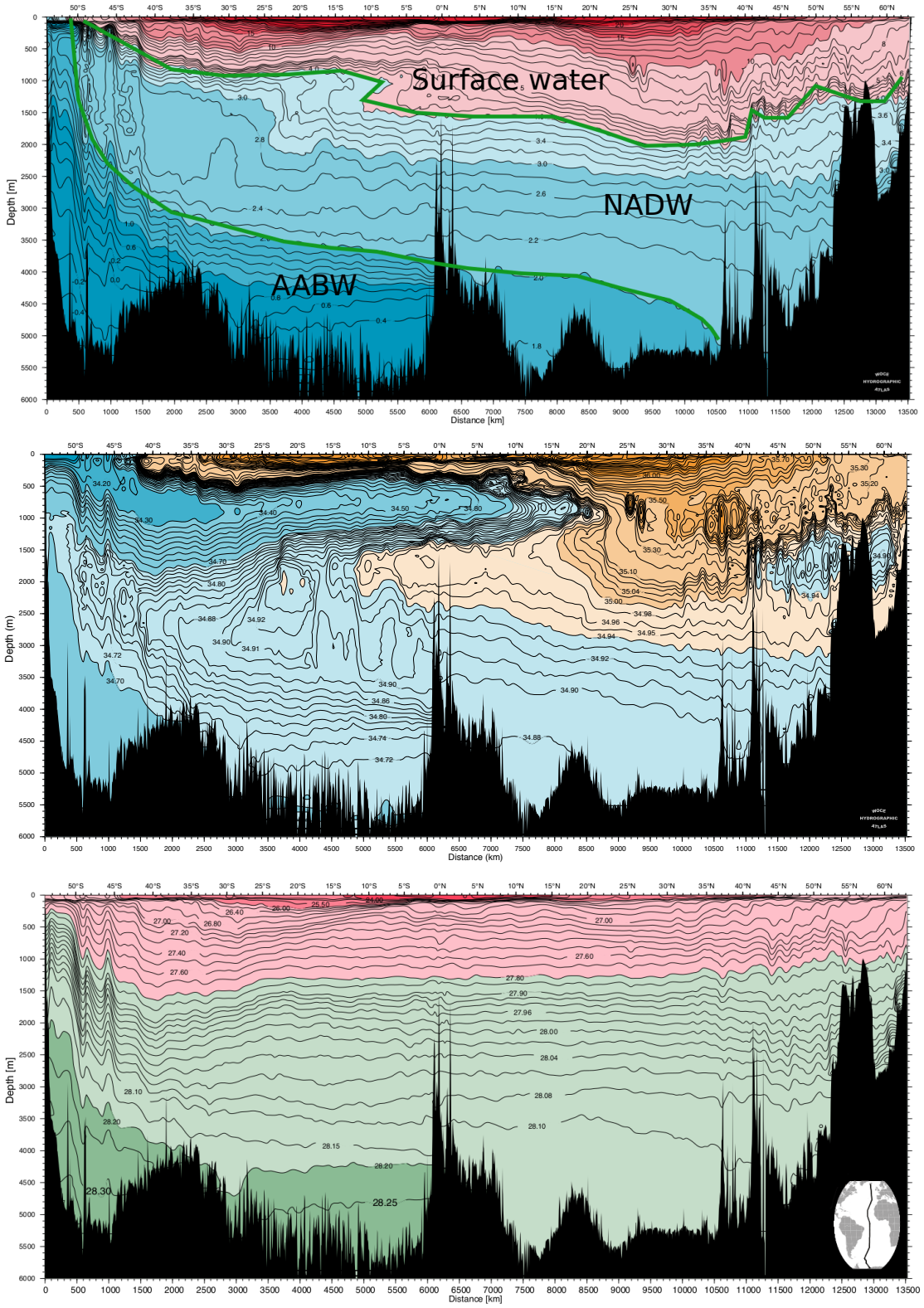

Figure 1.1: (top) Potential temperature (°C), (middle) salinity (PSU) and (bottom) neutral density (kg m^{-3}) for the Atlantic basin from 54°S to 63°N (see medallion). Areas of surface water, North Atlantic Deep Water (NADW) and Antarctic Bottom Water are roughly defined. From www.woceatlas.ucsd.edu

areas with similar ranges of temperature and salinity defining their density; they compose the water masses present in the Atlantic Ocean. At first glance, we can identify a warm, salty and light surface water and two cold and salty tongues coming from the north and south edges, corresponding to the formation of dense water in the northern Atlantic and bottom water in the Southern Ocean (southern Atlantic).

All the water masses in the ocean will not be described in the present document, only the two important water masses for our studies: the North Atlantic Deep Water (NADW) and the AntArctic Bottom Water (AABW). These two water masses form the two densest waters in the ocean and play a major role in the overturning thermohaline circulation and in the climate. Indeed, before sinking, they are in direct interaction with the atmosphere permitting, among others, the absorption and sequestration in deep ocean of anthropogenic carbon. The rate of deep water formation can vary strongly with atmospheric condition. Global warming could inhibit deep water formation inducing a slow-down of 20-50% [Rahmstorf et al. 1999] or even a break-down of the thermohaline circulation [Broecker 1987].

1.1.2 North Atlantic Deep Water

North Atlantic Deep Water has a temperature of 2-4°C, a salinity superior to 34.9 PSU and a neutral density superior to 26.76 kg m^{-3} (see Fig. 1.1). North Atlantic Deep Water is well described by Hansen and Østerhus [2000].

North Atlantic Deep Water is mainly formed in the Nordic Seas (Greenland and Norwegian seas) from Atlantic water during strong winters (see Fig. 1.2). The warm and light Atlantic surface water loses heat by exchange with the cold atmosphere. The water becomes colder at the surface and so sufficiently dense to induce a convective movement: the cold surface water sinks and lighter deep water comes up to the surface where it will be cooled (see Fig. 1.3). At the end of the winter, the newly formed dense water fills the bottom of the Nordic Seas. Additionally, water from the Arctic basin enters in the Nordic Seas from the Fram Strait and mixes with the cooled surface Atlantic water acquiring its final characteristics before overflowing equatorward through the Greenland-Iceland-Scotland ridge in the Atlantic basin as a deep water (see Fig. 1.2 - dashed curves on the eastern flank of Greenland).

---

can be seen as the most natural layer interface in the deep ocean.

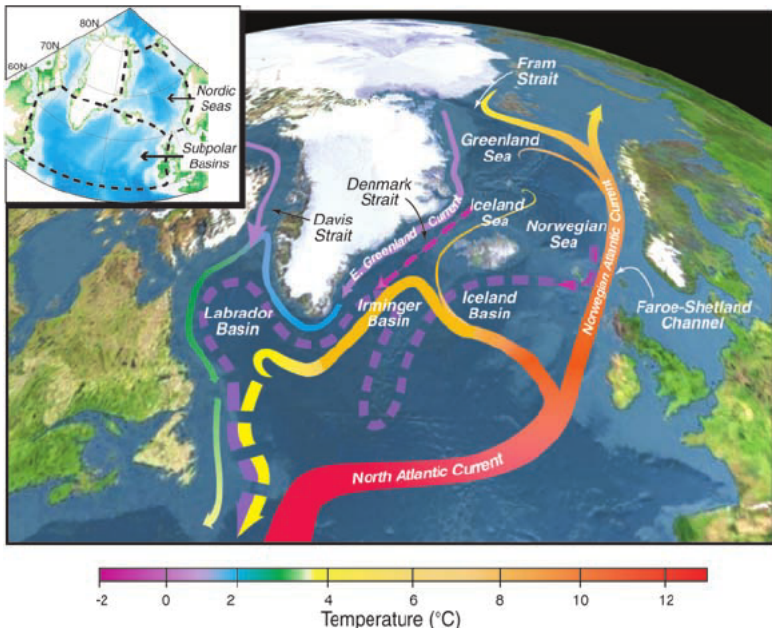

Figure 1.2: Schematic circulation of surface currents (solid curves) and deep currents (dashed curves) in the North Atlantic and in the Nordic Seas. Colors of curves indicate approximate temperatures. Figure adapted from [Curry and Mauritzen 2005].

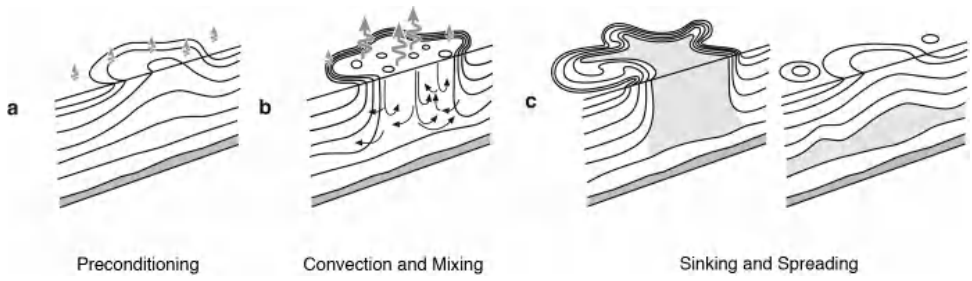

Figure 1.3: Sketch of the three phases of ocean deep convection: (a) preconditioning, (b) deep convection and mixing, and (c) sinking and spreading. Buoyancy flux through the sea surface is represented by curly arrows, and the underlying stratification/outcrops are shown by continuous lines. The volume of fluid mixed by convection is shaded. From [Marshall and Schott 1999].

The export of dense water from the Nordic Seas into the Atlantic basin is controlled by the presence of sills (see Fig. 1.2): the Denmark Strait between Greenland and Iceland (sill depth 620 m and volume exported 3 Sv, 1 Sv = 10^6 m^3s^{-1}), the ridge between Iceland and Faroe Islands (840 m, 1 Sv) and Scotland and the Faroe Bank Channel between Faroe Islands (420 m, 2 Sv). These sills are hydraulically controlled [Whitehead et al. 1974; Nikolopoulos et al. 2003; Girton et al. 2006] which means that the flow upstream of the sill is laminar (river regime)

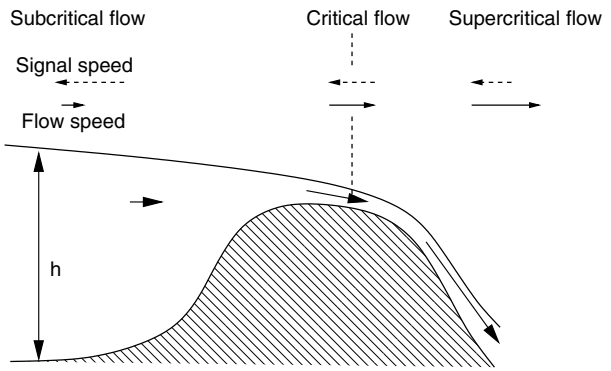

Figure 1.4: Sketch of an overflow from a marginal sea (Nordic Seas) to the open ocean (Northern Atlantic) [Huang 2010].

and downstream of the sill the flow is highly turbulent (torrential regime) [3] (see Fig. 1.4). The regime change is induced by a change in the relative importance of the kinetic energy compared to the potential energy of the fluid and quantified by the Froude number $Fr = U/\sqrt{g'h}$, where U is the fluid velocity, $g' = g\Delta\rho/\rho_0$ the reduced gravity, ρ_0 is the reference density, $\Delta\rho$ the density difference between the two layers and h the fluid thickness, which is the ratio between the kinetic energy and the potential energy. When the Froude number is greater than 1, for supercritical flow, which corresponds to large U, small h, and kinetic energy dominated regime (downstream of sill, torrential regime). When it becomes less than 1, for small U, large h, and hence potential energy dominated regime (upstream of sill, river regime).

In the case of an overflow, a propagating wave upstream of the sill can not propagate downstream due to the torrential regime ($Fr > 1$). Then, this wave is reflected at the sill and propagates backward modifying the upstream flow. The hydraulically controlled sill exerts a feedback on the upstream flow through the propagation of waves. This property can modulate the volume of overflow water exported in the northern Atlantic inducing a temporal variability in the North Atlantic Deep Water feeding. This mechanism will be further investigated in chapter 4 of this thesis.

In addition to North Atlantic Deep Water formed in the Nordic seas, there are two other (smaller) sources: the Labrador sea (see Fig. 1.2) and the Mediterranean Sea. The latter is at the upper edge (warmer water) of the water mass. North Atlantic Deep Water flows southward between 1 000 and 4 000 m and outcrops in

[3] It corresponds to the case of a waterfall where the river is gentle on the plateau and falls when the ground disappears.

the Southern Ocean (see Fig. 1.1).

Its origins are directly linked to the atmospheric conditions through the formation of sea ice in the Arctic and Labrador Seas, the cooling in the Nordic Seas and to the evaporation in the Mediterranean Sea.

1.1.3 Antarctic Bottom Water

Antarctic Bottom Water is less salty (34.8 PSU), colder ($T < 2°C$) and denser (28.27 kg m^{-3}) than the North Atlantic Deep Water.

Figure 1.5: Map of Antarctica showing the Southern Ocean and its connexions with the other basins. The Ross and Weddell Seas are two spots of Antarctic Bottom Water formation. From www.worldatlas.com

Antarctic Bottom Water is produced from the salty North Atlantic Deep Water and a portion of light fresh surface water mainly in the Weddell and Ross Seas in the Southern Ocean (see Fig. 1.5). The latter water cools by heat exchange with the cold atmosphere and during austral winter is enriched in salt by formation of sea ice and brine rejection. Cooling and enrichment in salt take place all over the winter due to the presence of polynyas in the Weddell and Ross Seas. A polynya is an open water area surrounding by sea ice, partly maintained by strong offshore katabatic winds which push seaward the newly formed sea ice (see Fig. 1.6). Without the sea ice lid, water continues to exchange heat with the atmosphere and to cool. During the same time, sea ice is continually produced in the polynya and pushed

away by the winds, enriching the water in brine rejection and thus producing the densest water mass. This dense water overflows the continental slope and fills up the Atlantic, Indian and Pacific basins below 4.5 km depth [Johnson 2008].

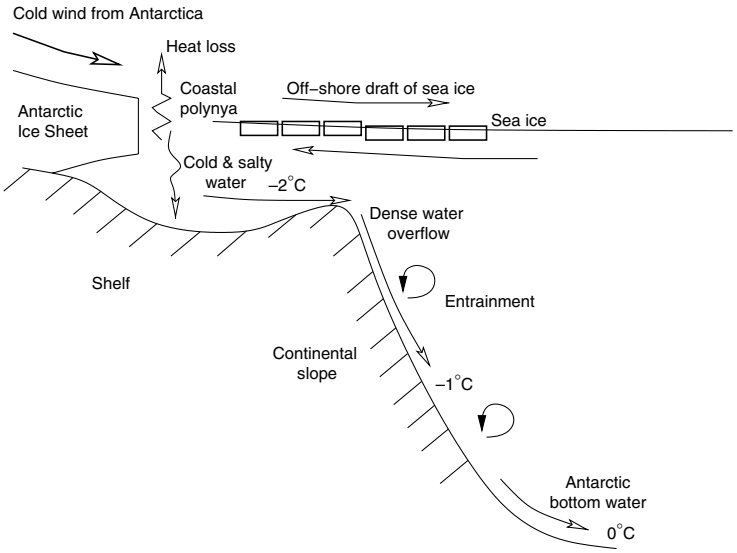

Figure 1.6: Sketch of a polynya and formation of Antarctic Bottom Water [Gordon 2002].

The newly formed Antarctic Bottom Water entrains and mixes with ambient Southern ocean waters to reach a maximum northward flow of about 20-30 Sv near 30°S [Ganachaud and Wunsch 2000; Lumpkin and Speer 2007; Talley et al. 2003; Talley 2008; 2013].

As for North Atlantic Deep Water, Antarctic Bottom Water formation is strongly influenced by the atmospheric condition around Antarctica but also by the characteristics of North Atlantic Deep Water. In a way, the formation of Antarctic Bottom Water is the result of a connexion between Arctic and Antarctic climates.

The circulation of the two main water masses and the northward return flow of surface water in the Atlantic Ocean is summarized in figure 1.7. We now turn to a full 3D description of water masses and circulation in the whole ocean.

1.1.4 A 3D ocean

The Atlantic basin is a good first step in understanding the ocean circulation, but the overall picture is more complex. The global ocean is inherently 3D and the

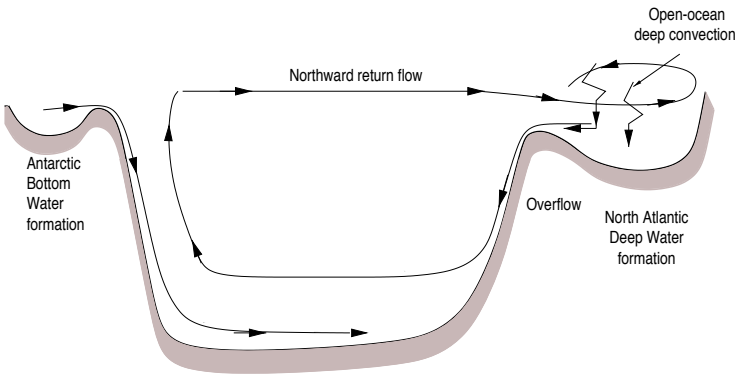

Figure 1.7: Sketch of the thermohaline Atlantic ocean circulation showing the formation of dense waters in the North and the South and the presence of surface water. This sketch has been adapted from [Huang 2010].

four main basins are connected by the central and circular Southern Ocean. A rapid overview of the global ocean is given here.

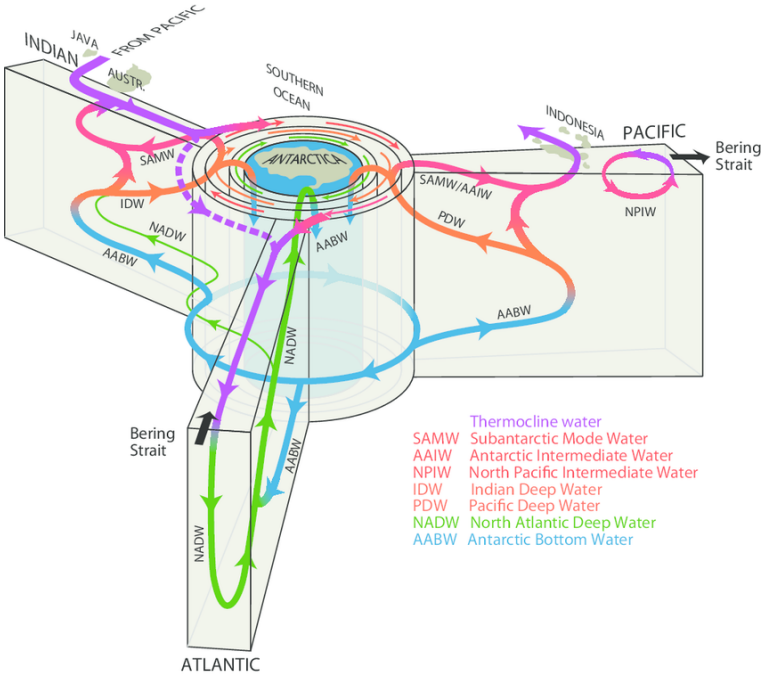

Figure 1.8: Sketch of the 3D thermohaline circulation [Lumpkin and Speer 2007; Talley 2011]

Indian and Pacific oceans do not have a source of deep water as in the Atlantic ocean but their circulation is connected with the other basins through the Southern Ocean. In fact, Antarctic Bottom Water flows into the three basins, Atlantic, Indian and Pacific, where it is modified before coming back in the Southern ocean (see Fig. 1.8).

The journey of the water masses in the different basins permits the erosion of their characteristics but also to efficiently exchange nutrients, carbon and other tracers all around the world. As we will see later, the consumption of Antarctic Bottom Water in the diverse basins is an important aspect of the overturning circulation.

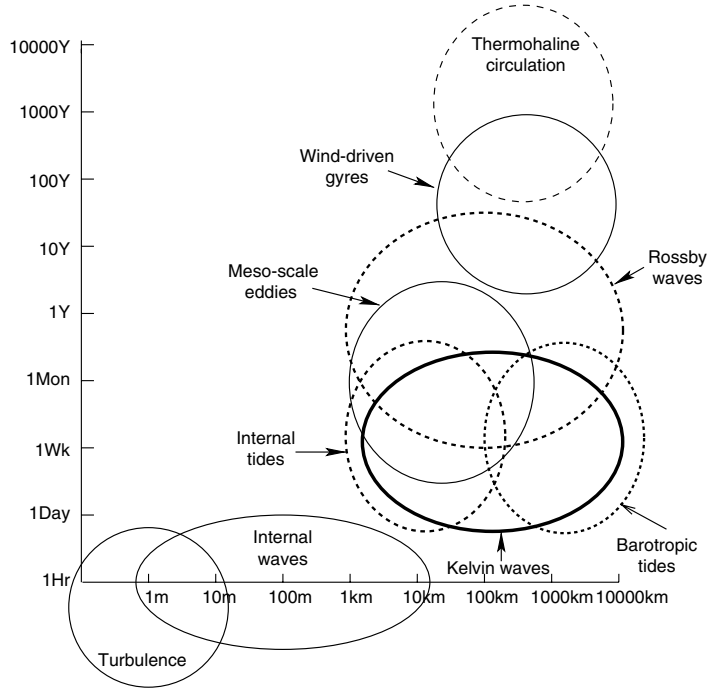

Figure 1.9: Time and spatial scales of motion in the ocean. From [Huang 2010].

The thermohaline circulation is a slow averaged circulation driven by a differential in temperature and salinity. It can be also defined as a balance of water masses in the ocean. To balance the water masses there are two processes: water mass formation and erosion. Most of the water masses are formed near the surface and sink. Furthermore, through either transformation or erosion, water mass properties are continually transformed (for example Indian Deep Water or Pacific Deep Water in figure 1.8). The thermohaline circulation is the slowest movement in the ocean with a time-scale of 100 to 10 000 years taking place all over the ocean from 100 km to 10 000 km (see Fig. 1.9). We note that this time scale only pertains to the extent and spreading of water masses. In fact, the formation of deep/bottom water happens seasonally. The long time-scale of the thermohaline circulation compared

to other faster processes allows one to consider this circulation as steady.

1.2 Meridional overturning circulation: pushed of pulled?

In the previous section, we described the ocean in terms of water masses but it was impossible to dissociate their origin and their future without talking about movement and circulation. But how does the ocean move?

The first thing that comes to mind is the action of the wind at the surface of the ocean. Then, from our personal experience, comes the souvenir of low tides revealing large areas suitable for catching shellfish.

Two schools exist to explain the meridional overturning circulation: the school of pushing, for whom the main mechanism is the formation of deep water at high latitudes, and the school of pulling which considers that the overturning circulation is mainly driven by external sources of mechanical energy, such as wind stress or tidal dissipation.

1.2.1 The school of pushing: Deep water formation pushes the deep current

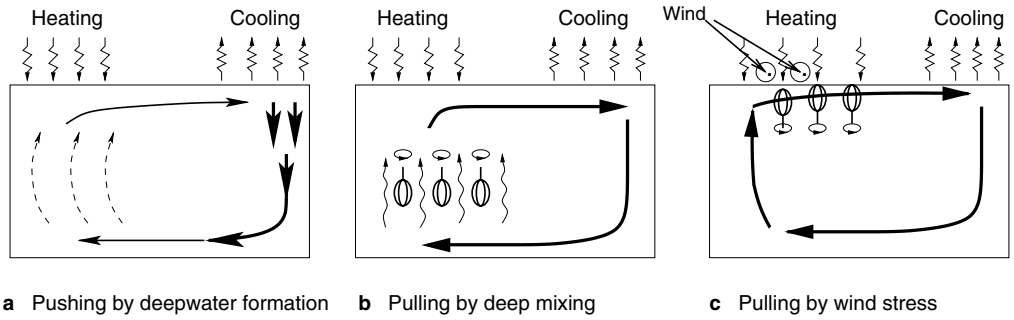

Figure 1.10: The three schools of the overturning circulation [Huang 2010].

A first glimpse of the global overturning circulation can be given by a conceptual model of the thermal overturning circulation driven by sea-surface differential heating (precipitation/evaporation can be taken into account as well without changing the results and when both effects are considered we talk about the thermohaline circulation). In this experiment, developed by Sandstrom [1908; 1916], only the thermal forcing is considered, with a cooling at one edge of the basin, representing a pole, and a heating at the other edge, representing the equator. A schematic

evolution of this experiment is given in figure 1.10a. The heating at the low latitudes expands the water and induces a sea surface uplift. Conversely, at high latitudes, water contracts and the sea surface declines. This differential in sea level creates a pressure gradient which induces a poleward movement of the surface water (in this simple experiment we do not take into account the role of Earth's rotation). The convergence of surface water at high latitude, yields an equatorward return flow in the interior ocean. At the end, the circulation is strong only near the high latitude and confined close to the surface. The surface thermal forcing alone drives a circulation that is so weak that it is not be able to penetrate to the deep ocean. At the end, the basin has a warm layer at low latitudes, and a thick cold deep layer.

In this system, the convective transfer of dense water to the bottom of the ocean is a mechanism for decreasing the potential energy; the center of mass is continually lowered. Later, Paparella and Young [2002] reformulate the discussion to show that a flow driven by buoyancy forces applied only at the surface can not generate an interior turbulence to maintain the circulation. To maintain this thermal circulation, an external source of gravitational potential energy is required. This source should be vertical mixing. Vertical mixing in a stratified fluid pushes light (heavy) water downward (upward), raising the center of mass. Vertical mixing is also called diapycnal mixing because it corresponds to a mixing across isopycnals.

1.2.2 The school of pulling by deep mixing: Deep mixing removes cold water from the abyss

In the school of pushing, dense water piles up at the bottom. With a source of mechanical energy to sustain mixing, as described below, deep mixing transforms cold water into warm water in the deep ocean, creating space for newly formed deep water (see Fig. 1.10b and 1.11). And therefore, deep mixing pulls the thermohaline circulation [Munk and Wunsch 1998; Huang 1999].

By a simple one-dimensional scale analysis and considering that temperature, salinity and density are local functions and horizontal velocities are negligeable, Munk [1966] shows that the downward diffusion of heat or salt is balanced by the upward advection of cold water. With an upward velocity estimated from the production of dense water, he obtains a diffusivity (variable related to the mixing) on the order of 10^{-4} m^2s^{-1} needed to sustain the formation of dense water. This order of magnitude for turbulent processes in the deep ocean is derived by assuming

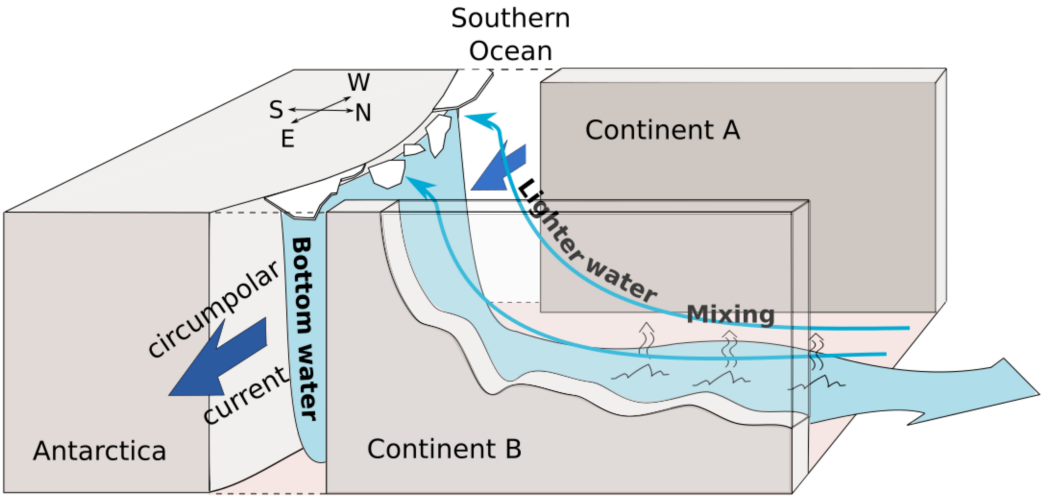

Figure 1.11: Sketch of consumption of Antarctic Bottom Water by diapycnal mixing.

that the vertical upwelling is spatially uniform. But numerous studies point out the inhomogeneity of mixing and diverse sources of diapycnal mixing exist in the deep ocean.

a. Lee waves and internal tides

The ocean is filled with ubiquitous internal waves [Garrett and Munk 1979; Staquet and Sommeria 2002]. Internal waves are waves within interior of a stratified fluid and in the ocean can be generated by interaction of currents with topography. Idealized studies of ocean internal waves focus on two limits. The first case is a constant current impinging a seafloor topography, as mesoscale eddies, and in that case internal waves are called lee waves. The second case is a periodic current impinging a seafloor topography, for example tides, and in that case, internal waves are called internal tides. The presence of internal tides in the ocean has been detected by altimetry [Egbert and Ray 2000] and tomography records [Dushaw et al. 1995].

Several mechanisms are at the origin of the generation of lee waves: mesoscale eddies and large-scale circulation over topography. Garrett and Kunze [2007] estimate that 0.5 TW is supplied by large-scale currents impinging bottom topography.

An estimated value of energy input by the tides into the ocean is 3.5 TW. Internal tides are internal waves generated by a tidal current, whose frequency is given by the tide at the origin of its generation. Munk and Wunsch [1998] estimate

that 1 TW should be available to mix the abyssal ocean.

b. Geothermal heating

The geothermal heating is able to influence the circulation by heating the abyssal water from below. The heat entering in the ocean is transported into the ocean above the sea floor by molecular processes through the porous or solid seabed and by hydrothermal flux of heat carried by fluid circulating through the seabed. Nevertheless, geothermal heating is inhomogeneous in space and the estimated net energy input is only 0.05 TW [Huang 1999; Wunsch and Ferrari 2004].

c. Drag forcing on the sea floor

Drag forcing provides energy input by mechanical interaction of the mean circulation and the eddies with the topography. It could contribute 0.1 TW [Stammer et al. 2000].

In the 1990s, high accuracy measurements of diffusivity (variable related to turbulent mixing) showed weak mixing over the abyssal plains ($O(10^{-5})$ m^2s^{-1}) and enhanced mixing up to two order of magnitude higher above rough topography [Polzin et al. 1997; Ledwell et al. 2000; Kunze et al. 2006]. Far from the Southern ocean and the other places with strong eddy kinetic energy, the principal current in the deep ocean is the barotropic tidal flow. Those two results suggest that the main source of diapycnal mixing in the deep ocean is the breaking of internal tide generated by the interaction of a tidal flow above rough topography.

1.2.3 The school of pulling by wind stress: The Southern westerlies pull cold water from the deep ocean

Two example of wind conditions over the ocean

Winds acting on the sea surface produce direct conversion of the atmospheric kinetic energy into oceanic kinetic and potential energies. Lueck and Reid [1984] estimate a net transfer of kinetic energy from the wind field to the ocean surface-layer between 7-36 TW.

In this section, two examples of wind effect on the ocean circulation are developed in relation with the studies presented in this thesis.

a. Nordic Seas circulation: westerlies and easterlies

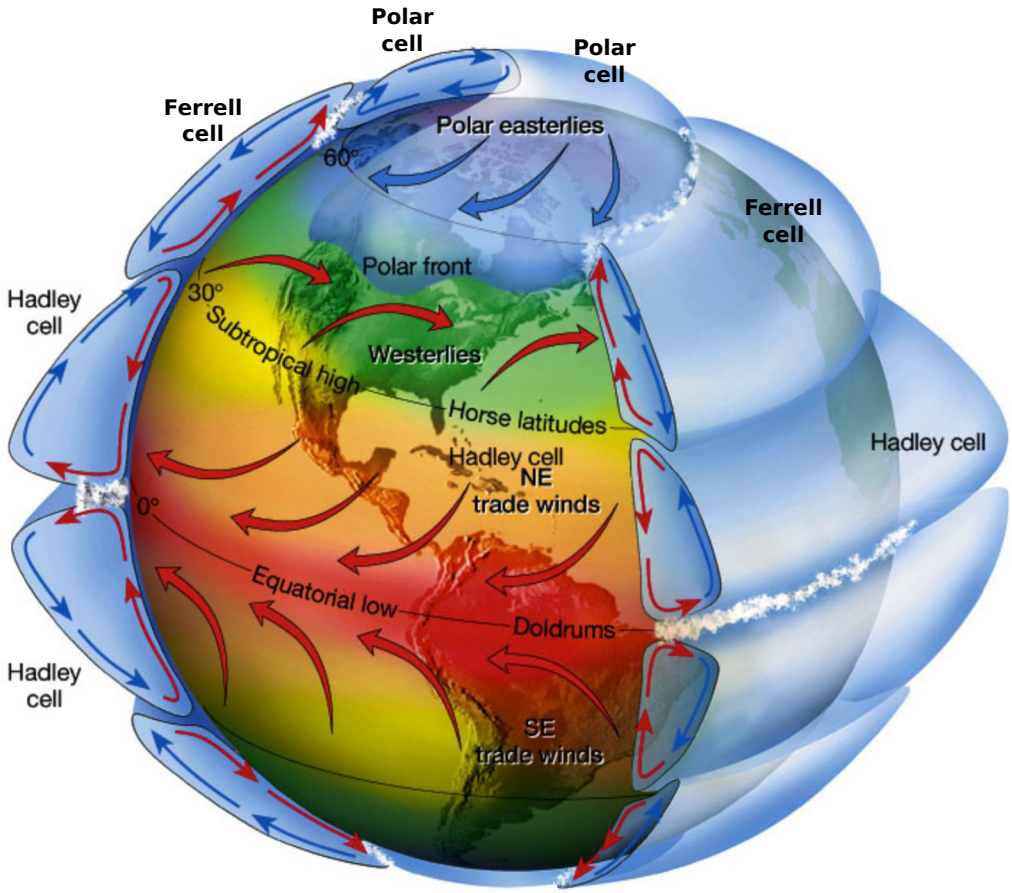

Figure 1.12: Idealized view of the large scale flows in the atmosphere showing the easterlies linked to the polar cell and the westerlies linked to the Ferrell cell. From [Lutgens and Tarbuck 2001]

The Nordic Seas are located at the confluence of the Ferrell and polar cells (see Fig. 1.12). The Ferrel cell is associated to northwesterly winds at the surface while the polar cell has southeasterly winds at the surface. The mean wind circulation in the Nordic Seas is cyclonic [Aagaard 1970]. By friction with the water surface, water is entrained and forms a cyclonic gyre in the Nordic Seas (actually several cyclonic gyres exist in the sub-basins).

Wind stress is communicated to the ocean surface layer through viscous processes. The ocean is affected by the Coriolis acceleration and both effects (Coriolis acceleration and wind stress) permit the development of an Ekman layer. Velocity

in the Ekman layer is strongest at the sea surface (due to wind stress) and decreases exponentially downward. The Coriolis acceleration induces a velocity vector spiral with increasing depth. The transport associated with the Ekman layer is exactly perpendicular to the right (to the left) of the wind in the Northern Hemisphere (in the Southern hemisphere).

The cyclonic circulation in the Nordic Seas induces an Ekman transport toward the coasts and then an upwelling in the center of the Nordic Seas, bringing deep water to the surface. The cyclonic wind-driven circulation implies that the cooling of Atlantic water happens in the middle of the gyre while the sinking of the newly formed cold water happens along the boundaries.

b. Southern circulation: westerlies and easterlies

The circulation in the Southern Ocean is strongly linked to the winds: westerlies between 40°S and 60°S and easterlies south of 60°S, closer to Antarctica. Westerlies are particularly strong due to the absence of land and entrain the water by friction (wind-stress), generating a strong Ekman flow. The Ekman flow induces an upwelling yielding a horizontal buoyancy gradient leading to a strong geostrophic current named the Antarctic Circumpolar Current (ACC). The Antarctic Circumpolar Current is affected by the seafloor like the Drake Passage, which is a semi-open boundary, allowing the flow to pass. The Antarctic Circumpolar Current is highly variable in time and space, and depends strongly on the atmospheric conditions.

In Antarctica, katabatic winds blow seaward and due to the Earth's rotation, are deviated on the left forming the easterlies. By the same processes as the westerlies, they entrain the water below and produce a westward current close to Antarctica coasts.

In the case of easterlies in the Southern Hemisphere, this implies that the Ekman transport associated to the westward current along Antarctica is southward (toward Antarctica), inducing a downwelling at the boundary. For the westerlies, the Ekman transport associated with the Antarctic Circumpolar Current is equatorward. Both Ekman transports produce a divergence around the latitude of 50-60°S implying the presence of an upwelling.

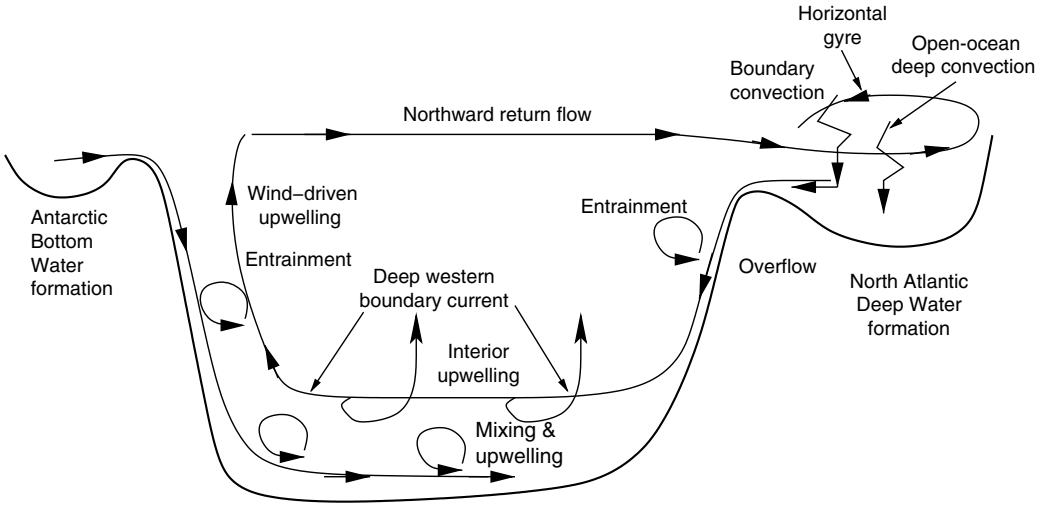

Figure 1.13: Sketch of the diverse mechanisms behind the overturning thermohaline circulation in the Atlantic basin [Huang 2010]. The lower cell can be transposed in the Indian and pacific basins.

Effect of the wind around Antarctica on the global overturning circulation

The atmospheric conditions around Antarctica induce an Ekman upwelling around the latitude of 50-60°S. Due to this upwelling, North Atlantic Deep Water is pulled up to the upper ocean where its properties are modified. Wind-driven upwelling is believed to represent a significant part of the globl overturning circulation and water mass transformation (see Fig. 1.10c). The wind stress energy input to the ocean is in fact larger (7-36 TW) [Lueck and Reid 1984] than the energy input due to tides (3.5 TW) [Toggweiller and Samuels 1995; Talley 2013].

1.2.4 Combination of the two schools of pulling

The total amount of mechanical energy required to sustain upwelling in the Southern ocean is estimated as 2 TW, including the estimation of tidal dissipation in the deep ocean and wind stress energy input to surface geostrophic currents [Munk and Wunsch 1998]. An emerging picture is that the upwelling is sustained by both wind stress driven Ekman transport and deep mixing [Wunsch and Ferrari 2004; Kuhlbrodt et al. 2007].

In the ocean, all the processes presented in this section exist and participate to the global overturning circulation. However, they do not contribute equally, and

wind stress and deep mixing are two keys ingredients to maintain the global overturning circulation.

1.3 Waves

The ocean is a stratified fluid in salinity and temperature. A perturbation in this fluid, like a rock thrown in a pond, generates waves by energy transfer from the perturbation source to the waves. Once, the waves are generated, they can propagate through the ocean and transfer energy from one point to another. Thus, the waves become a local or a remote source of energy able to generate mixing or to modify the flow.

We propose in this section to revisit three types of waves relevant to this thesis: internal waves and internal tides, Kelvin waves and topographic Rossby waves.

1.3.1 Stratified ocean: the Brunt Väisälä frequency

The action of gravity on a fluid generates a vertical pressure gradient within the fluid. For a fluid at rest, this pressure gradient is equal to the product of gravity acceleration g by the density of the fluid ρ. This equilibrium can be applied in dynamics when we consider movements essentially horizontal; more precisely it applies when the horizontal scales are much larger than the vertical scales of motion. This is the so called hydrostatic equilibrium

$$\partial_z P = -\rho g, \tag{1.1}$$

where the vertical axis is oriented upward, ∂_z denotes partial derivative with respect to z, and P the hydrostatic pressure. Now, if we immerse a body in a fluid submitted to gravity, the action of the hydrostatic pressure on this body corresponds to a vertical force equal to difference in weight between the body and the displaced volume; this has been demonstrated by Archimedes. In the case of a fluid volume with density ρ_1 immersed in an homogeneous fluid of density ρ_2, the Archimedes' thrust per unit volume is

$$\mathbf{F}_A = (\rho_2 - \rho_1) g \mathbf{z}, \tag{1.2}$$

where z is the unit vector in the vertical direction positive upward. In the case of the ocean, the stratification is continuous with height $\rho(z)$, and at a given height this force will point downwards for fluid parcels heavier than the mean, and upwards for fluid parcels with density lower than the mean. This results in an equilibrium distribution of density as a function of depth with heavier, denser waters at depth. Supposing that a mean stratification $\rho(z)$ is established, a volume dV of water with

density ρ_0 will be at equilibrium at depth z_0 if $\rho(z_0) = \rho_0$. Out of this position of equilibrium, the acceleration $\mathbf{a}$ of the volume is

$$\rho_0 dV \mathbf{a} = -(\rho_0 - \rho(z))dV g\mathbf{z}. \tag{1.3}$$

Taking the origin of the vertical axis at $z = z_0$, we obtain

$$\mathbf{a} = \partial_{tt} z = -\frac{g}{\rho_0}\partial_z \rho z = -N^2 z. \tag{1.4}$$

This equation is the equation of a harmonic oscillator at pulsation with frequency N, called the Brunt-Väisälä frequency. According to this equation, if $N > 0$, the fluid parcel oscillates with period $2\pi/N$. In reality where viscous effects are present, it would oscillate with smaller and smaller amplitude, and eventually go back to its position of equilibrium due to the action of viscosity.

1.3.2 Internal gravity waves

We discussed previously the impact of mixing for the global overturning circulation. One particular type of waves is crucial to the spatial distribution of mixing, namely internal gravity waves. In this section, we introduce their main properties.

The ocean is a continuously stratified fluid and far from the thermocline and the upper ocean, the deep ocean can be considered stably and linearly stratified. Therefore a water parcel that is displaced in the vertical, for example upward, encounters water with lower density and accelerates back downward. The water parcel starts to oscillate before going back to its original position. This oscillation generates an internal gravity wave. The restoring force is the buoyancy force, which is the product of gravity and the difference in density between the displaced water parcel and the environment at the same pressure.

In the case of stratified fluid, it is common to use the Boussinesq approximation which means we consider that the fluctuations of density around the mean value are weak. In other words, we consider that the fluid has a constant density in the horizontal to leading order, with a smaller density perturbation σ: $\rho(x, y, z, t) = \rho_0 + \rho_s(z) + \sigma(x, y, z, t)$, $\rho_0 \gg \rho_s \gg \sigma$. The vertical stratification $\rho_s(z)$ is the most important external ocean property with the Coriolis frequency f, for internal gravity waves. The stratification is characterized by the Brunt-Väsiälä frequency, $N^2 = -\frac{g}{\rho_0}\partial_z \rho_s$. Because internal waves can have a period on the order of hours, internal gravity waves are influenced by the Earth's rotation.

Let us now derive the dispersion relation of internal gravity waves. We consider a rotating and stratified ocean with a constant Brunt Väisälä frequency N. The unapproximated mass conservation equation is

$$\partial_t \rho + u\nabla\rho + \rho\nabla\cdot\mathbf{u} = D_t\rho + \rho\nabla\cdot\mathbf{u} = 0, \tag{1.5}$$

where $\mathbf{u} = (u, v, w)$ is the velocity vector. In this equation the time scales advectively (D_t scales in the same way as $\nabla\cdot\mathbf{u}$), then we may approximate this equation by

$$\nabla\cdot\mathbf{u} = 0. \tag{1.6}$$

The motion of the fluid is governed by the Navier-Stokes equation

$$\rho\left(\partial_t\mathbf{u} + \mathbf{u}\cdot\nabla\mathbf{u} + f\mathbf{k}\wedge\mathbf{u}\right) = -\nabla P + \rho\mathbf{g} + \nu\Delta\mathbf{u}, \tag{1.7}$$

where f is the Coriolis frequency. These three equations define the dynamics of rotating and stratified fluids. To derive the dispersion relation of internal waves, we neglect the diffusive term. In general the viscous term is small compared to the other terms in the interior of the fluid, though as we will see in the next chapters it can become important for the smallest-scale internal waves. We introduce the buoyancy perturbation $b = -g(\sigma/\rho_0)$. Rewriting the above equations under the Boussinesq approximation, we obtain

$$\partial_t u + \mathbf{u}\cdot\nabla u - fv = -\frac{1}{\rho_0}\partial_x p, \tag{1.8}$$

$$\partial_t v + \mathbf{u}\cdot\nabla v + fu = \frac{1}{\rho_0}\partial_y p, \tag{1.9}$$

$$\partial_t w + \mathbf{u}\cdot\nabla w = -\frac{1}{\rho_0}\partial_z p + b, \tag{1.10}$$

$$\partial_t b + \mathbf{u}\cdot\nabla b + wN^2 = 0, \tag{1.11}$$

$$\nabla\cdot\mathbf{u} = 0, \tag{1.12}$$

$$\tag{1.13}$$

where p is the nonhydrostatic pressure, and the total pressure $P = p_{hyd} + p$ is composed of a part p_{hyd} in hydrostatic equilibrium with $\rho_0 + \rho_s$, and a non-hydrostatic part p. This set of equations describes the nonlinear dynamics of rotating and stratified fluids. We simplify the computation to the case of two-dimensional waves, which are the most relevant to the following chapters. We

thus work in the (x,z) plane but allowing a constant velocity v in the y direction. We also linearize the equations around a state of rest, neglecting the nonlinear terms. The above equations can then be reduced to a single equation for the streamfunction ψ, defined as $u = \partial_z\psi$ and $w = -\partial_x\psi$,

$$\partial_{tt}\Delta\psi + f^2\partial_{zz}\psi = -N^2\partial_{xx}\psi. \tag{1.14}$$

This equation is the linear equation of internal wave propagation in the absence of viscosity. We look for wave solutions of the form $\psi_0 e^{i(\mathbf{k}\cdot\mathbf{x}-\omega t)}$, where $\mathbf{k} = (k, 0, m)$ is the wave vector, ω the wave frequency and $\mathbf{x} = (x, y, z)$. The resulting dispersion relation is

$$\omega^2 = \frac{k^2N^2 + m^2f^2}{k^2 + m^2}, \tag{1.15}$$

rewritten in terms of slope

$$\frac{k}{m} = \pm\sqrt{\frac{\omega^2 - f^2}{N^2 - \omega^2}} = \pm tan\theta. \tag{1.16}$$

The angle θ can vary between 0 and $\pi/2$ and represents the angle of the wave vector $\mathbf{k}$ with the horizontal. There are four possible sign combinations for k and m, corresponding to the four directions of propagation for the internal wave. An important point from equation (1.16) is that the frequency of a propagative wave has to be between the Coriolis and the Brunt-Väisälä frequencies, $f < \omega < N$.

Lee waves versus internal tides

As mentioned earlier, theoretical studies of internal waves consider the two limits of constant steady flow (lee waves) and periodic oscillating flow (internal tides). Here we described those two limits.

a. Lee waves

In the case of the lee waves, the forcing source is a steady flow with an amplitude U_0. The time dependence in the previous set of equations (Eq. 1.8-1.12) disappears

$$U_0 u_x - fv = -\frac{1}{\rho_0}\partial_x p, \tag{1.17}$$

$$U_0 v_x + fu = 0, \tag{1.18}$$

$$U_0 w_x = -\frac{1}{\rho_0}\partial_z p + b. \tag{1.19}$$

$$U_0 b_x + wN^2 = 0, \tag{1.20}$$

$$u_x + w_z = 0. \tag{1.21}$$

$$\tag{1.22}$$

The set of equations can be reduced to a single equation for the vertical velocity w,

$$U_0^2(w_{xx} + w_{zz})_{xx} + N^2 w_{xx} + f^2 w_{zz} = 0. \tag{1.23}$$

The wave solution is of the form $w \sim e^{i(kx+mz)}$ and the dispersion relation becomes

$$m^2 = k^2 \frac{N^2 - U_0^2 k^2}{U_0^2 k^2 - f^2}. \tag{1.24}$$

Lee waves can radiate away if their frequency $U_0 k$ is in the range $f < U_0 k < N$ so that m is real.

b. Tides and internal tides

Tides are well known since 1687 and 1775 with Newton's [Newton 1687] theory of equilibrium tides and Laplace's [Laplace 1775] formulation of the tidal equation. The origin of tides comes from gravitational forces exerted by the sun and the moon on Earth, including the ocean.

The presence of continents blocks the westward propagation of the tide as the Earth turns. The result is a complex pattern of tides that move around each basin. The tide in any location is unique because it is a function of the lunar and solar tidal forcing but also of the basin and coastline geometry. The relative amplitude of the tide depends on the location (see Fig. 1.14). The amplitude is zero where the cotidal lines intersect, and these points are called amphidromes.

The primary tidal frequencies observed in terms of amplitude are the semi-diurnal and diurnal. The characteristics of the tidal signal is an oscillatory movement of the whole water column, hence the name barotropic tide. It induces a back and

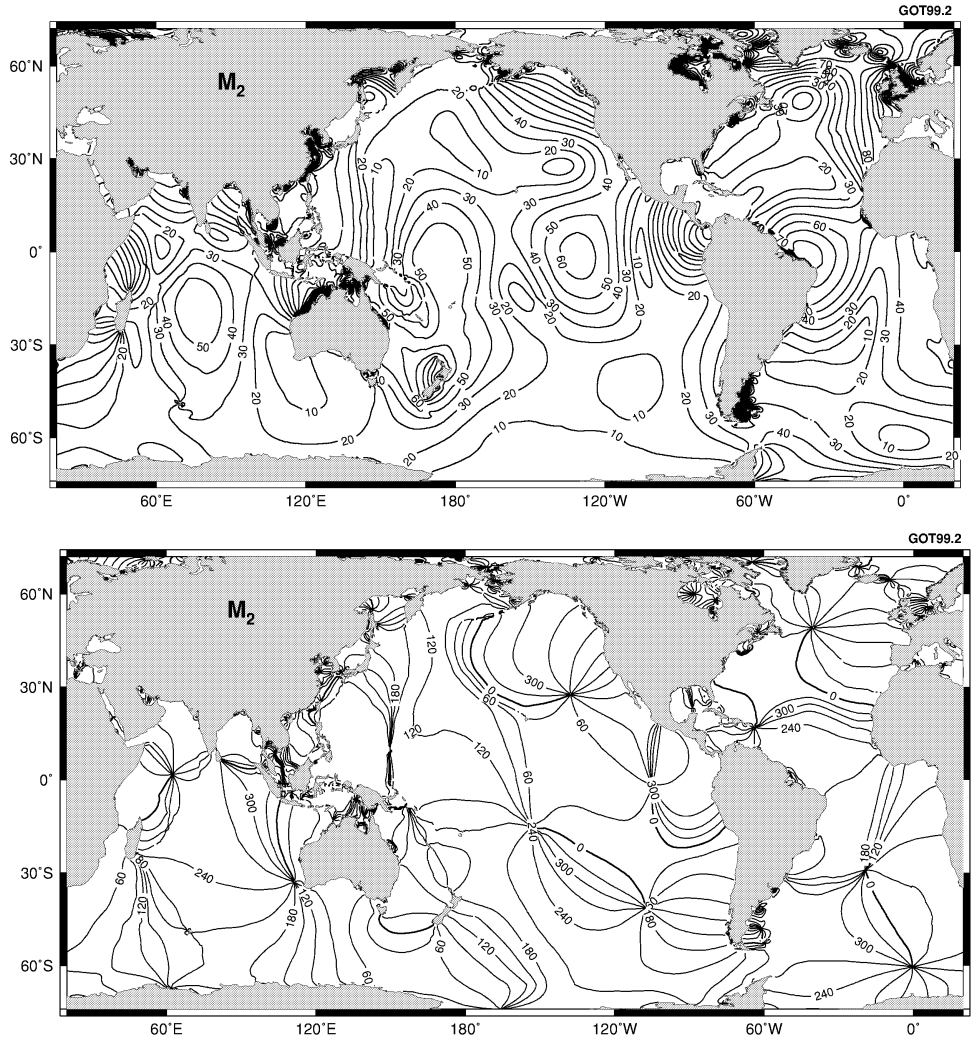

Figure 1.14: Maps of (top) cotidal (phase) lines (in °) and (bottom) tidal amplitude (cm) for the semi-diurnal tide M2 Ray [1999].

forth horizontal motion of the whole water column.

Considering the semi-diurnal tide in a narrow zonal channel of uniform depth H, narrow enough that the planetary rotation may be ignored, the equations of the movement are

$$\partial_t u = -g\partial_x(\eta - \eta_e) \tag{1.25}$$

$$\partial_t \eta + H\partial_x u = 0, \tag{1.26}$$

where η_e is the equilibrium tide. In a zonal channel, this has the form

$$\eta_e = A\sin(kx - \omega_{tide}t), \tag{1.27}$$

where ω_{tide} is the frequency and k is the wavenumber of the semi-diurnal tide. This represents the back and forth motion.

For the internal tides, the frequency of the waves ω is equal to the frequency of the tide ω_{tide} and the dispersion relation is given by (1.15).

1.3.3 Kelvin and topographic Rossby waves

Kelvin and topographic Rossby waves are believed to play an important role for the ocean transport, a hypothesis that will be further investigated and quantified in this thesis. In this section, we introduce the main properties of these waves.

In the case of a reverse 1.5-layer reduced gravity model, where we consider a thick and motionless upper layer and a thin and active bottom layer, the equations governing the dynamics (momentum equation, mass conservation equation and incompressible fluid) are

$$\partial_t \mathbf{u} + \mathbf{u} \cdot \nabla \mathbf{u} + f\mathbf{u} \wedge \mathbf{k} = -g'\partial_x h + \nu \Delta \mathbf{u}, \tag{1.28}$$

$$\partial_t h + \mathbf{u} \cdot \nabla h + h \nabla \cdot \mathbf{u} = 0, \tag{1.29}$$

$$\nabla \cdot \mathbf{u} = 0, \tag{1.30}$$

where $\mathbf{u} = (u, v)$ is the horizontal velocity, f the Coriolis frequency, $g' = g\Delta\rho/\rho_0$ the reduced gravity, h the displacement of the interface and ν the viscosity. Making the assumption that the nonlinear terms and the viscosity can be neglected, the momentum and the mass-conservation equations become

$$\partial_t u - fv = -g'\partial_x \eta, \tag{1.31}$$

$$\partial_t v + fu = -g'\partial_y \eta, \tag{1.32}$$

$$\partial_t h + [\partial_x (hu) + \partial_y (hv)] = 0, \tag{1.33}$$

Where $h(x, y, t) = H + h'(x, y) + \eta(x, y, t)$.

After calculations and using the vorticity equation $(\partial_x(1.32) - \partial_y(1.31))$ and the divergence equation $(\partial_x(1.31) + \partial_y(1.32))$, we obtain

$$\frac{\partial}{\partial_t}\left[\partial_{tt}\eta + f^2\eta - \nabla \cdot (g'h\nabla\eta)\right] + g'fJ(\eta, h) = 0, \tag{1.34}$$

where $J(a, b) = \partial_x a \partial_y b - \partial_y a \partial_x b$ is the Jacobian operator.

The scale analysis of the equation gives

$$\frac{\eta}{T^3}, \quad \frac{f^2\eta}{T}, \quad \frac{g'H\eta}{L^2T}, \quad \frac{H\delta g' f\eta}{L^2},$$

where T is the time-scale of the waves, L the horizontal length scale, H the mean depth and $H\delta$ is the typical size of topographic mountain heights at the horizontal scale L.

a. Kelvin waves

Kelvin waves are another type of waves whose particularity is to be "trapped" to the coastlines, which means that their amplitude is highest at the coast (y=0) and decreases exponentially seaward. Kelvin waves propagate with the coast to the right in the Northern Hemisphere (and to the left in the Southern Hemisphere).

The Kelvin wave is a high frequency wave, so the equation is dominated by the first term. The Kelvin wave is trapped to the coast so the no-normal flow boundary condition implies that $v = 0$ at $y = 0$. This result suggests that we look for a solution with $v = 0$ everywhere. One last thing, we consider the water depth constant and equals to H. The Kelvin wave equation is

$$\partial_{tt}u = c^2\partial xxu. \tag{1.35}$$

where $c = \sqrt{g'H}$, the phase of shallow water waves. The solution of the previous equation is

$$u = F_1(x + ct, y) + F_2(x - ct, y), \tag{1.36}$$

giving a surface displacement of the form

$$\eta = \sqrt{\frac{H}{g'}}\left[-F_1(x + ct, y) + F_2(x - ct, y)\right]. \tag{1.37}$$

The solution is a superposition of two waves, one (F_1) travelling in the negative $x-$direction, and the other in the positive $x-$direction. The y dependence of the wave is obtain using equation 1.32, with $v = 0$, which gives

$$\partial_y F_1 = \frac{f}{\sqrt{g'H}}F_1, \tag{1.38}$$

$$\partial_y F_2 = -\frac{f}{\sqrt{g'H}}F_2, \tag{1.39}$$

with solutions

$$F_1 = F(x + ct)e^{y/L_d}, \tag{1.40}$$

$$F_2 = G(x - ct)e^{-y/L_d}, \tag{1.41}$$

where $L_d = \sqrt{g'H}/f$ is the length of decay (radius of deformation) in the $y-$direction. The solution F_1 grows exponentially away from the coast, and so fails to satisfy the condition of boundedness at infinity. The remaining solution is

$$u = G(x - ct)e^{-y/L_d}, \tag{1.42}$$

$$v = 0, \tag{1.43}$$

$$\eta = \sqrt{\frac{H}{g'}}G(x - ct)e^{-y/L_d}. \tag{1.44}$$

The Kelvin decays exponentially away from the boundary.

b. Topographic Rossby waves

The topographic Rossby wave is a particular case of Rossby wave. The existence and radiation of Rossby waves require variations of potential vorticity. In fact, Rossby waves undulate on the background potential vorticity gradient shearing and reshaping the background potential vorticity. A variation of vorticity can be induced by a variation in latitude or in the case of a topographic Rossby wave, a variation of the fluid depth (presence of a slope).

The topographic Rossby wave is a low frequency wave and in equation (1.34), the first term can be neglected. Now, for the topographic Rossby waves, we consider that $h'(x, y) = -\alpha y$, where α is the slope of the topography. Neglecting η in the equation for h and the second order terms, equation (1.34) becomes

$$\frac{f^2}{g'}\partial_t\eta - \partial_t\left[(H - \alpha y)\left(\partial_{xx}\eta + \partial_{yy}\eta + \frac{-\alpha}{(H - \alpha y)}\partial_y\eta\right)\right] - f\alpha\partial_x\eta = 0. \tag{1.45}$$

Scale analysis of the equation gives the following terms

$$\frac{f^2\eta}{g'T}, \quad \frac{(H + \alpha L)\eta}{L^2T}, \quad \frac{(H + \alpha L)\eta}{L^2T}, \quad \frac{\alpha\eta}{LT}, \quad \frac{f\alpha\eta}{L}.$$

We consider the topographic height small compared to the fluid height ($\alpha L \ll H$), so we neglect the αy part in terms 2, 3 and 4. Then, the equation for the topographic Rossby wave is

$$\partial_t \Delta\eta - \frac{f^2}{g'H}\partial_t\eta + \frac{f\alpha}{H}\partial_x\eta = 0. \tag{1.46}$$

We look for solutions of this equation of the form $\eta = \eta_0 e^{i(\mathbf{k}\cdot\mathbf{r}-\omega t)}$, where $\mathbf{k} = (k, l, 0)$ is the wave vector and ω the wave frequency. The resulting dispersion relation is

$$\omega = -\frac{\beta_{topog} k}{k^2 + l^2 + \frac{1}{R_{bc}^2}}, \tag{1.47}$$

where $\beta_{topog} = (f\alpha/H)$ is the topographic beta and $R_{bc} = \sqrt{g'H}/f$ is the baroclinic Rossby radius.

After introducing the global context of the following studies and the main properties of the waves treated in this thesis, the introduction is followed by two parts on the dissipation of internal tides generated at the topography in 2D numerical simulations and a third part on the role of Kelvin and topographic Rossby waves on the circulation of an upstream basin controlled by a hydraulically controlled sill. The last part concludes on those three projects.

2

Internal tide dissipation at topography: triadic resonant instability equatorward and evanescent waves poleward of the critical latitude

The first project presented in this thesis is about the mechanisms behind the latitudinal dependence of the internal tide energy dissipation. In others words, we propose a mechanism to explain the dissipation of the semi-diurnal lunar tide (M2) in the deep ocean. This study is based on theoretical results and idealized numerical simulations where a tidal current is impinging a sinusoidal topography.

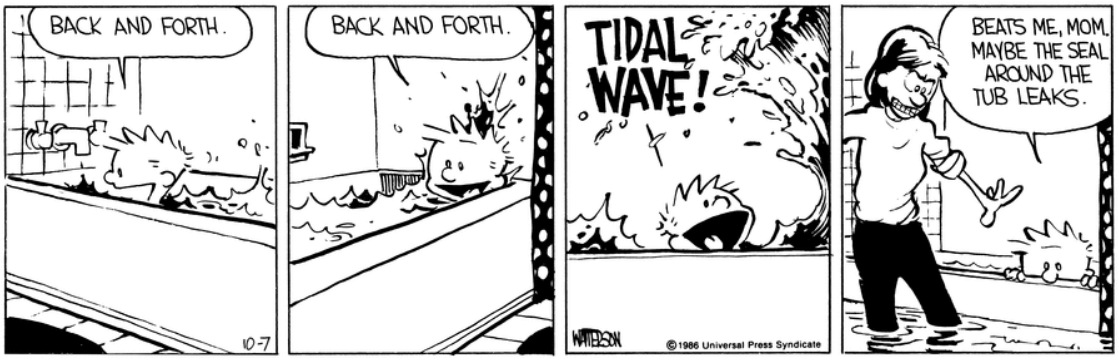

Bill Watterson, 7 October 1986

Confidential manuscript submitted to *JGR-Oceans*

Internal tide dissipation at topography: triadic resonant instability equatorward and evanescent waves poleward of the critical latitude

O. Richet [1], J.-M. Chomaz [1], and C. Muller [2]

[1]LadHyX, École polytechnique, Palaiseau, France
[2]Laboratoire de Météorologie Dynamique, École Normale Supérieure, Paris, France

Abstract

Several studies have shown the existence of a critical latitude where the dissipation of internal tides is strongly enhanced. Internal tides are internal waves generated by barotropic tidal currents impinging rough topography at the seafloor. Their dissipation and concomitant diapycnal mixing are believed to be important for water masses and the large-scale ocean circulation. The purpose of this study is to clarify the physical processes at the origin of this strong latitudinal dependence of tidal energy dissipation. We find that different mechanisms are involved equatorward and poleward of the critical latitude. Triadic resonant instabilities are responsible for the dissipation of internal tides equatorward of the critical latitude. In particular, a dominant triad involving the primary internal tide and near-inertial waves is key. At the critical latitude, the peak of energy dissipation is explained by both increased instability growth rates, and smaller scales of secondary waves thus more prone to break and dissipate their energy. Surprisingly, poleward of the critical latitude, the generation of evanescent waves appears to be crucial. Triadic instabilities have been widely studied, but the transfer of energy to evanescent waves has received comparatively little attention. Our work suggests that the nonlinear transfer of energy from the internal tide to evanescent waves is an efficient mechanism to dissipate internal tide energy near and poleward of the critical latitude. The theoretical results are confirmed in idealized high-resolution numerical simulations of a barotropic M2 tide impinging a sinusoidal topography in a linearly stratified fluid.

2.1 Introduction

Internal waves are ubiquitous in the ocean and they play a key role in the circulation and the stratification of the oceans [Garrett and Munk 1979]. They permit energy transfer from mesoscale flows to small spatial scales, where they are dissipated and induce diapycnal mixing [Munk and Wunsch 1998; Wunsch and Ferrari 2004]. Interest in internal waves dynamics has been enhanced in the last decades with parametrization of internal waves-driven mixing in the global climate models. The consumption of Antarctic Bottom Water (AABW) in the ocean interior is strongly influenced by wave-induced diapycnal mixing [Talley 2013; Melet et al. 2016] and more precisely by mixing at the topography [Ferrari et al. 2016]. Far from the Antarctic Circumpolar Current (ACC), diapycnal mixing is primarily induced by internal tides [Nikurashin and Ferrari 2013; De Lavergne et al. 2016b;a], which are

internal waves generated by barotropic tide current impinging rough topography [Garrett and Kunze 2007]. Estimates of AABW upwelling can differ by a factor two or more depending on the spatial distribution of internal tide dissipation and the associated mixing [De Lavergne et al. 2016b].

For the purpose of understanding the dynamics of internal tides, several numerical studies considered the dissipation of semi-diurnal internal tide (generated by topography interacting with the semi-diurnal baropotropic M2 tide). They showed a strong latitudinal distribution and the existence of a critical latitude where dissipation is strongly enhanced. This critical latitude exhibits enhanced dissipation of both low-mode [MacKinnon and Winters 2005] and high-mode internal tide [Nikurashin and Legg 2011; Richet et al. 2017]. The critical latitude corresponds to the latitude where the Coriolis frequency f matches half the tidal semi-diurnal frequency ω_0: $f \approx \omega_0/2$. Observations confirm the enhancement of dissipation near the critical latitude, albeit with weaker amplitude than expected from numerical studies [Alford et al. 2007; MacKinnon et al. 2013]. One possible explanation for this amplitude discrepancy is the Doppler effect due to background oceanic currents, which spreads the dissipation over a wider range of critical latitudes [Richet et al. 2017]. MacKinnon and Winters [2005], Hazewinkel and Winters [2011] and Nikurashin and Legg [2011] suggest that the mechanism to explain the latitudinal dependence of internal tide dissipation is the Parametric Subharmonic Instability (PSI). In this paper, we propose to complete Nikurashin and Legg [2011]'s numerical study and investigate in detail the physical processes leading to the distribution of M2 internal tide dissipation with latitude.

PSI is a weakly nonlinear resonant phenomenon [McComas and Bretherton 1977; Young et al. 2008] in which the energy is transferred, from large scales to smaller scales, from the primary internal tide to two secondary waves at approximately half the tidal frequency. The instability of a primary wave producing two secondary waves which match the resonant conditions of triadic resonant instability (TRI) has been confirmed experimentally in a rotating tank [Maurer et al. 2016]. However, the constraints associated with laboratory experiments, in particular size contraints, imply that the Reynolds number is low, in other words viscous effects are much stronger than in the ocean, and this can impact energy transfer in triads. Here we revisit and expand the generation of triads via the TRI observed in Maurer et al. [2016], in numerical simulations more representative of the oceanic conditions.

Equatorward of the critical latitude, we investigate whether TRI is the most efficient mechanism that dissipates internal tide energy, and which triads are involved in these energy transfers. Two candidates in the literature are triads with secondary

waves at frequencies $\omega_1 = f$ and $\omega_2 = \omega_0 - f$ [Nikurashin and Legg 2011], or $\omega_1 = \omega_2 = \omega_0/2$ [MacKinnon and Winters 2005]. Note that in both cases, these secondary waves satisfy the resonance conditions $\omega_0 = \omega_1 + \omega_2$ (see Section 2.4 for more details on the triadic resonant instability theory). Poleward of the critical latitude, one of the waves has a frequency below f for both of those triads, which is then not within the range of internal wave frequencies (internal waves have frequencies between f and the stratification frequency N), so there is no resonant triad. Another dissipation mechanism has been proposed and will be investigated here, the "$2f$-pump" [Young et al. 2008; Korobov and Lamb 2008]. The $2f$-pump is an extension of PSI in a rotating frame, with the generation of near-inertial secondary waves which are *evanescent*. This physical process can extract energy from the primary internal tide at ω_0 to evanescent secondary waves at $\omega_0/2$. We will investigate whether this process plays a role in our simulations and whether it can lead to strong dissipation poleward of the critical latitude.

Section 2.2 of the paper describes the equations governing the motion of internal waves and the setup of the numerical simulations. Section 2.3 is an overview of the results, where we split the latitudinal dynamics of internal tides into two parts: part I, equatorward of the critical latitude, where internal tides are propagating waves and transfer their energy through triadic resonant instabilities, and part II, poleward of the critical latitude, where there is the possibility of energy transfer to secondary evanescent waves. Sections 2.4 and 2.5 investigate in detail the mechanisms of dissipation in these two parts. Results are summarized and conclusions are offered in section 2.6.

2.2 Methods

2.2.1 Theoretical background: equations of motion

Internal waves are waves found in stratified fluids. In this section, we derive their dispersion relation from a simplified set of equations, namely the Boussinesq equations on the f-plane assuming constant stratification. Under the Boussinesq approximation, the total density is $\rho(x, z, t) = \rho_0 + \rho_s(z) + \sigma(x, z, t)$, where ρ_0 is assumed constant, and ρ_s is linked to the background vertical stratification corresponding to the Brunt-Väisälä frequency N satisfying $N^2 = -(g/\rho_0)(d\rho_s/dz)$ assumed constant. We introduce the buoyancy related to the density perturbation $b = -(g/\rho_0)\sigma$. Internal waves are governed by the nonlinear Boussinesq equations of motion on the f-plane:

$$\frac{D}{Dt}\mathbf{u} + f\hat{\mathbf{z}} \times \mathbf{u} = -\frac{1}{\rho_0}\nabla p + b\hat{\mathbf{z}} + \nu\nabla^2\mathbf{u}, \tag{2.1}$$

$$\frac{D}{Dt}b + N^2 w = 0, \tag{2.2}$$

$$\nabla \cdot \mathbf{u} = 0. \tag{2.3}$$

We reduce the set of equations to the 2D case (x, z), considering $\partial/\partial y \equiv 0$. Nevertheless, we allow for a velocity v constant in the y direction. The model is a 2D model with three components. This assumption is relevant if we consider that roughness of ridges is nearly two-dimensional. D/Dt denotes the Lagrangian derivative, and we solve the equations for flow velocity $\mathbf{u} = (u, v, w)$ and buoyancy b. ν denotes the viscosity.

If we linearize this set of equations about a state of rest neglecting viscosity, and look for wave solutions of the form $\propto e^{i(kx+mz-\omega t)}$, we obtain the dispersion relation of internal waves:

$$\omega^2 = N^2 \sin^2\theta + f^2 \cos^2\theta = \frac{N^2k^2 + f^2m^2}{\kappa^2}, \tag{2.4}$$

with ω the frequency of the internal wave, θ is the angle of energy propagation with the horizontal such that $\mathbf{k} = (k, 0, m) = \kappa(\sin\theta, 0, \cos\theta)$ where κ is the magnitude of the wavevector $\mathbf{k}$. We see that propagating waves (i.e. with real ω, k and m), necessarily have their frequency $\omega \in [f, N]$ ($f < N$ typically in the ocean). Note also that for a given horizontal scale, i.e. for a given k, the vertical scale of the waves decreases when the frequency decreases. In other words lower frequency waves have smaller scales, and are hence more likely to break and dissipate their energy, yielding the mixing ultimately relevant to the large-scale ocean circulation [Staquet and Sommeria 2002].

2.2.2 Numerical simulations configuration

For the numerical simulations, we use the Massachusetts Institute of Technology Global Circulation Model (MITgcm; Marshall et al. [1997]), a high-resolution numerical model in nonhydrostatic configuration. The nonhydrostatic configuration allows the explicit representation of processes such as hydraulic jumps or Kelvin-Helmholtz instabilities. The model is developed with the finite-volume method to provide the treatment of irregular geometries like the topography using the MITgcm partial cells' architecture. The bottom boundary is treated with a no-slip condition.

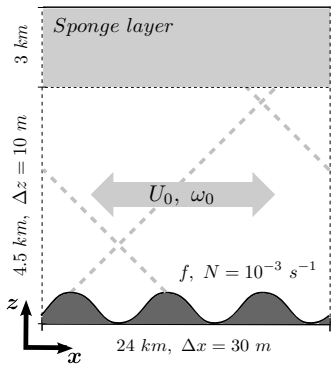

Figure 2.1: Schematic of the numerical setup. The barotropic tidal current, with amplitude U_0 and frequency ω_0 interacts with a one-dimension sinusoidal topography in a linearly stratified (N constant) and rotating (f constant) fluid and generates internal tides (oblique dashed lines). The gray shaded area at the top of the domain represents the sponge layer.

The main characteristics of the domain are synthetized in Figure 2.1. The domain is two-dimensional and periodic in the x direction. The horizontal size of the domain is 24 km with a uniform resolution of 30 m. The vertical extent of the domain is equal to 7.5 km, organized in two layers: the 4.5 km bottom layer and the 3 km sponge layer at the top. Indeed, the goal of this paper is to highlight the mechanisms by which internal tides dissipate locally near their generation site, so we neglect the reflection of the waves at the ocean surface and their interactions with the thermocline. In other words, we consider a semi-infinite ocean, and for this purpose we impose a sponge layer at the top of the ocean interior to absorb upward-propagating waves which are not dissipated locally. In the sponge layer, momentum and buoyancy are damped with a linear drag with a time scale of 1 hour. The bottom layer corresponding to the ocean interior has a uniform resolution of 10 m. The resolution of the sponge layer is progressively stretched from 10 m at the base of the layer to 70 m at the top. The model time step is 30 seconds. These high-resolution idealized simulations are designed to allow the resolution of a wide range of spatial and temporal scales of the turbulence.

In the simulations, the fluid is linearly stratified in the vertical with constant buoyancy frequency $N = 10^{-3}$ s^{-1}, representative of the deep-ocean stratification. Following Nikurashin and Legg [2011] and Richet et al. [2017], the viscosity (horizontal and vertical) is equal to $\nu = 2\times10^{-3}$ m^{2}s^{-1} and the diffusivity (horizontal and vertical) is set to $\kappa = 10^{-4}$ m^{2}s^{-1}. The Coriolis frequency f is set to be constant for each given simulation. To investigate the latitudinal variation of internal tide dissipation, we vary f between simulations.

The simulations are initiated from a state of rest and run for 30 days (a statistically steady state is reached in 5 to 10 days). The tidal barotropic flow is imposed by adding a body force to the momentum equations, yielding a barotropic semi-diurnal lunar M_2 tide, $U(t) = U_0 \sin(\omega_0 t)$ with an amplitude $U_0 = 2.5$ cm s^{-1} and the tidal frequency $\omega_0 = 1.4 \times 10^{-4}$ s^{-1}.

Internal tides are generated by the barotropic flow interacting with an idealized sinusoidal topography. The choice of a simple idealized sinusoidal topography is motivated by the fact that the dissipation profiles and magnitudes are found to be similar to those obtained with a realistic topography spectrum, as long as the vertical and horizontal Froude numbers are the same [Richet et al. 2017]. We therefore use the realistic horizontal and vertical Froude numbers $\mathrm{Fr}_h = U_0/(N 2\pi/k_0) \approx 4 \times 10^{-3}$ and $\mathrm{Fr}_v = U_0/(Nh) \approx 10^{-1}$, where $k_0 = 0.8 \times 10^{-3}$ m^{-1} is the horizontal wavenumber and $h = 110$ m is the rms height of the sinusoidal topography. With this choice, we expect the sensitivity of dissipation to latitude and the physical processes involved in our simulations to be relevant, at least qualitatively, to more realistic conditions representative of the deep ocean in the region of the Brazil Basin [Nikurashin and Legg 2011; Richet et al. 2017].

2.3 Overview of numerical results: latitudinal distribution of tidal dissipation and physical processes involved

The purpose of this study is to explain the physical mechanisms behind the latitudinal distribution of internal tide energy dissipation. From numerical results, we give a first glimpse of possible mechanisms and their repartition with latitude before studying them in detail and validate their existence and their efficiency for the dissipation of internal tide energy in following sections.

Nikurashin and Legg [2011] and Richet et al. [2017] show a strong dependence of internal tide energy dissipation with latitude. Figure 2.2 summarizes these results. Each point corresponds to a simulation at a given latitude (f constant) and the viscous energy dissipation is averaged over x direction and over the last 10 days of simulation, and integrated over 0 m to 50 m above topography for the bottom boundary layer, and over 50 m to 2 km for the ocean interior. The critical latitude (28.8° corresponding to $f = 0.7 \times 10^{-4}$ s^{-1}) is defined as the latitude where $f = \omega_0/2$ and is found to be close to the maximum of energy dissipation. From the equator toward the critical latitude, the energy dissipation increases slowly at the beginning

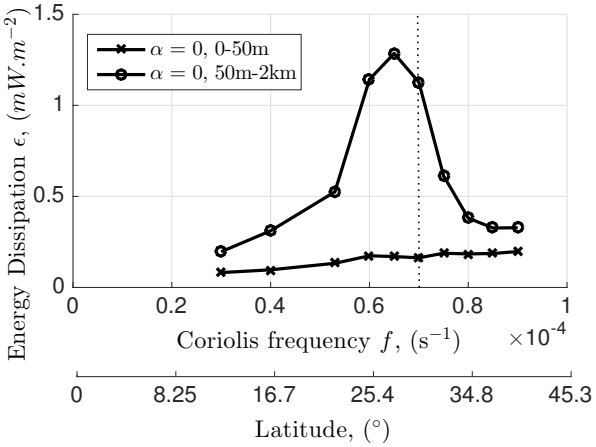

Figure 2.2: Energy dissipation rate integrated in the bottom 50 m (cross) and between 50 m and 2 km (circle). The vertical black dotted line materializes the critical latitude when $f = \omega_0/2$.

and strongly after ∼22° of latitude ($f = 0.53 \times 10^{-4}$ s^{-1}). Poleward of the critical latitude, energy dissipation decreases and becomes constant after ∼35° of latitude ($f = 0.8 \times 10^{-4}$ s^{-1}). We divide the curve into two parts: part I equatorward of the critical latitude where secondary waves, in particular at $\omega_0/2$ or $\omega_0 - f$, are propagating, i.e. their frequency is in the internal wave range $[f, N]$ see Eqn. (2.4); and part II poleward of the critical latitude where those secondary waves are evanescent, i.e. for a given horizontal wavenumber k, their vertical wavenumber m is imaginary and the waves are evanescent in the vertical direction z (Eqn. 2.4).

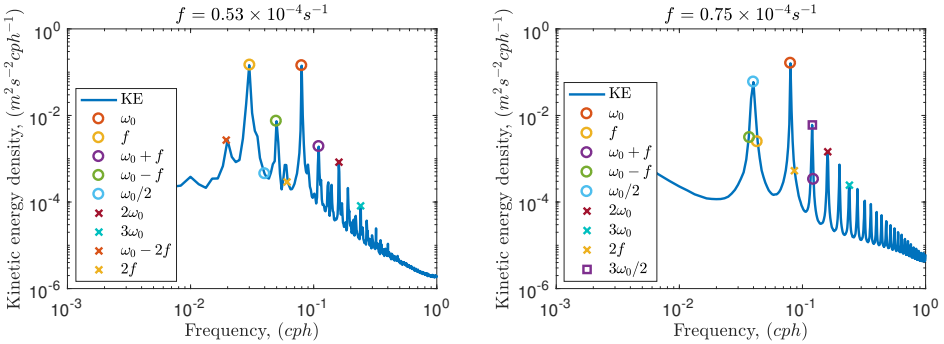

Figure 2.3: Kinetic energy density spectra from simulations at (a) $f = 0.53 \times 10^{-4}$ s^{-1} and (b) $f = 0.75 \times 10^{-4}$ s^{-1}. Spectra are calculated over the period of 5 to 30 days and averaged zonally and over the region 500 m above topography.

Figure 2.3 shows kinetic energy density spectra from simulations at $f = 0.53 \times 10^{-4}$ s^{-1} and $f = 0.75 \times 10^{-4}$ s^{-1} averaged over 5 to 30 days. Equatorward of the critical latitude (Figure 2.3a), dominant frequencies in the domain are ω_0, the primary internal tide, but also waves at frequency f, i.e. inertial waves, and at

frequencies $(\omega_0 - f)$ (and with smaller amplitude $\omega_0 + f$). These results suggest that the physical mechanism responsible for the energy transfer from internal tides to smaller-scale secondary waves is the formation of resonant triads between the primary internal tide, inertial waves and waves at frequencies $(\omega_0 - f)$, and to a lesser extent $(\omega_0 + f)$. Poleward of the critical latitude (Figure 2.3b), the dominant frequencies in the kinetic energy spectrum are the primary internal tide at ω_0 and the evanescent wave at $\omega_0/2$ ($\omega_0/2 < f$). This result suggests the transfer of energy to smaller-scale evanescent near-inertial waves as the dominant physical process leading to the dissipation of the primary internal tide.

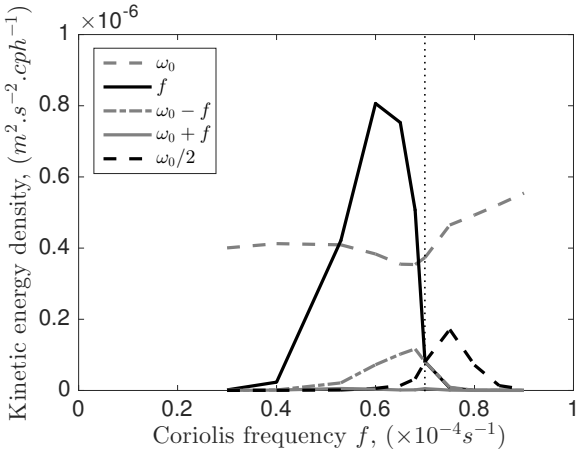

Figure 2.4: Latitudinal evolution of the kinetic energy density for the leading frequencies in the domain: the primary internal tide ω_0 (gray dashed), inertial waves f (black plain) and waves at frequencies $(\omega_0 - f)$ (gray point-dashed), $(\omega_0 + f)$ (gray plain - here nearly indistinguishable from the axis) and $\omega_0/2$ (black dashed). The vertical black dotted line materializes the critical latitude.

The latitudinal evolution of the main wave frequencies are summarized in Figure 2.4. Equatorward of the critical latitude, the enhancement of energy dissipation seems to be linked to a strong generation of inertial waves accompanied by waves at $\omega_0 - f$. The waves at $\omega_0 + f$ do not play a leading-order role. It should be noted here and it will be proved later that the triad involving $\omega_0 + f$ is not an unstable triad. Poleward of the critical latitude, the dissipation seems to be dominated by energy transfers to secondary waves at $\omega_0/2$.

These results suggest two different mechanisms for internal tides dissipation in the two regions previously defined: equatorward of the critical latitude (part I) and poleward of the critical latitude (part II). Equatorward of the critical latitude, dissipation of internal tides seems to involve triadic resonant instabilities. Poleward of the critical latitude, dissipation seems to be linked to the energy transfer to

evanescent waves. In the next sections, we investigate in detail those physical mechanisms and provide further evidence for their key role in the dissipation of tidal energy.

2.4 Part I - Equatorward of the critical latitude: Triadic Resonant Instabilities (TRI)

In order to explain the latitudinal dependence of the energy dissipation equatorward of the critical latitude, we investigate theoretically resonant triads. We will see that the energy transfers occur in three stages. During the first stage, corresponding to the beginning of the simulation, secondary waves with a wide range of frequencies are generated by triadic resonant instability from the primary internal tide. A second stage consists of an accumulation of inertial waves close to topography. Finally, in a third stage, the dominant triadic resonant instability appears between the primary internal tide and the inertial waves, generating waves at frequencies $(\omega_0 - f)$.

2.4.1 Stage I: TRI

Triadic resonant instability theory

In the following, we consider that only the primary wave with streamfunction amplitude Ψ_0 (See appendix A for the streamfunction form of Equations (2.1-2.3)) with frequency $s_0\omega_0$ (by convention, we consider $\omega_0 > 0$ and s_0 is its sign), wavevector $\mathbf{k_0} = (k_0, m_0)$ and sign s_0, is present initially in the system. We impose $m_0 < 0$ to match the numerical simulation where the primary internal tide is generated at the topography and propagates upward (i.e. has positive vertical group velocity, which for internal waves is equivalent to negative vertical phase velocity). The secondary waves with amplitudes $\Psi_{1,2}$ are present as noise. The two secondary waves $(s_1, \omega_1, \mathbf{k_1})$ and $(s_2, \omega_2, \mathbf{k_2})$ form a resonant triad with the primary wave, satisfying the spatial resonant condition

$$\mathbf{k_0} = \mathbf{k_1} + \mathbf{k_2}, \tag{2.5}$$

and the temporal resonance condition

$$s_0\omega_0 = s_1\omega_1 + s_2\omega_2. \tag{2.6}$$

In all calculations, we consider that wave frequencies $\omega_{0,1,2}$ are positive,while $s_{0,1,2}$ are their signs. Using the dispersion relation for internal waves Eqn. (2.4), the resonant conditions lead to

$$s_0\sqrt{\frac{k_0^2N^2+m_0^2f^2}{\kappa_0^2}}=s_1\sqrt{\frac{k_1^2N^2+m_1^2f^2}{\kappa_1^2}}+s_2\sqrt{\frac{(k_0-k_1)^2N^2+(m_0-m_1)^2f^2}{(k_0-k_1)^2+(m_0-m_1)^2}}. \quad (2.7)$$

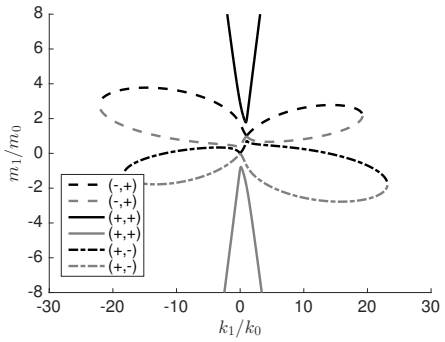

Figure 2.5: The curves represent the location of (k_1, m_1) satisfying Equation 2.7 at $f = 0.53 \times 10^{-4}$ s^{-1} for the three possible combinations of signs and for the realistic parameter values used in our simulations. Plain lines represent unstable branches associated to (+,+) combination signs, while dashed lines correspond to neutrally stable cases.

Without loss of generality, we can set $s_0 = +1$. For a given primary wave (s_0, k_0, m_0), the solution of this equation for each sign combination $(s_0 = +1, s_1, s_2)$ is the curve in the (k_1, m_1)-plane shown on Figure 2.5 using the stratification value $N = 10^{-3}$ s^{-1} representative of the deep ocean, and a value of f equatorward of the critical latitude $f = 0.53 \times 10^{-4}$ s^{-1}. We use the same sign convention on wave frequencies as Bourget et al. [2013] and Maurer et al. [2016], leading to similar results. But Figure 2.5 as well as the growth rates in Figure 2.6 show differences compared to these observational studies. This is because of the oceanic parameter values used here, while their values were constrained by the laboratory experiments. In particular, Maurer et al. [2016] are constrained by the limited spatial scales allowed in experiments, and have a Reynolds number $Re \sim 200$. In our simulations, the Reynolds number is more turbulent and thus closer to the oceanic regime with a $Re \sim 10^4$.

As the sign of the primary wave is imposed, we have to consider four sign combinations for (s_1, s_2): (-,-), (+,+), (-,+) and (+,-). First of all, no solution exists for the combination (-,-). To know which branch, defined by the sign combination, is stable or unstable, we calculate the associated growth rate σ given by (see full calculation and definition of coefficients I_1 and I_2 in Appendix A):

$$\sigma=-\frac{\nu}{4}\left(\kappa_1^2+\kappa_2^2+\frac{f^2m_1^2}{\omega_1^2}+\frac{f^2m_2^2}{\omega_2^2}\right)+\sqrt{\frac{\nu^2}{16}\left(\kappa_1^2-\kappa_2^2+\frac{f^2m_1^2}{\omega_1^2}-\frac{f^2m_2^2}{\omega_2^2}\right)^2+I_1I_2\mid\Psi_0\mid^2}. \quad (2.8)$$

A negative growth rate corresponds to a stable branch (dashed curves on Figure 2.5) and is not relevant for this study, which is the case for combinations (+,-) and (-,+). The study will focus only on the (+,+) combination which has a positive growth rate and hence corresponds to an unstable branch (plain curves on Figure 2.5). In the simulations, we expect to observe a transfer of energy to the most unstable secondary waves (i.e. with the largest growth rate).

Without loss of generality, we can limit our analysis to the upper branch: the upper and lower branches (+,+) correspond to exchanging the labels 1 and 2 between $(\omega_1, \mathbf{k}_1)$ and $(\omega_2, \mathbf{k}_2)$, and thus show the same triad (ω_0 primary wave yields ω_1 and ω_2 secondary waves). It follows from Eqn. 2.5 that they are obtained from one another by symmetry with respect to $\mathbf{k_0/2}$.

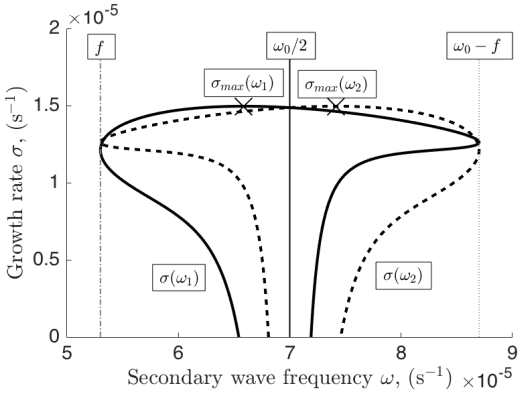

Figure 2.6: Growth rate σ as a function of the frequency of secondary waves associated to the upper unstable branch (plain black line on Figure 2.5) for $f = 0.53 \times 10^{-4}$ s^{-1}. The plain curve represents the growth rate as a function of the frequency of the first secondary wave ω_1, and the dashed curve represents the growth rate as a function of the frequency of the second secondary wave ω_2.

Figure 2.6 shows the growth rate σ associated with the upper unstable branch as a function of the secondary waves frequencies (ω_1 or ω_2), calculated for each point of the upper branch of Figure 2.5 (as mentioned above, because of the symmetry $(\omega_1, \mathbf{k}_1) \longrightarrow (\omega_2, \mathbf{k}_2)$, there is no need to consider the lower branch (+,+) on Figure 2.5). Despite a weak maximum growth rate σ_{max}, we see that the temporal growth rate is roughly constant over a wide range of frequencies (between f and $\omega_0 - f$). In other words, no specific triad is selected. We therefore expect in the simulations that TRIs generate, from the primary internal tide, secondary waves with a wide range of frequencies.

It should be noted that as f is increased toward $\omega_0/2$ the unstable branch gets more and more folded with a cusp moving to infinity when approaching $\omega_0/2$. No

triadic instability is possible after the critical latitude $f = \omega_0/2$. We will come back to internal tide dissipation poleward of the critical latitude in section 2.5.

Hence the theory of TRI, applied with oceanic parameters, predicts the generation, from the primary tide, of secondary waves with a wide range of frequencies. In the next section, this theoretical result is compared to numerical simulations to validate TRI as the principal mechanism in internal tide dissipation equatorward of the critical latitude.

Consistency with the numerical results at early times

The numerical simulation discussed here is at the same latitude as the theoretical case ($f = 0.53 \times 10^{-4}$ s^{-1}). Several snapshots of the wave field (left column) and the wave field without the primary internal tide signal (right column) are shown on Figure 2.7 at 0.5, 1.5, 3 and 5 days. The wave field is obtained by subtracting the zonal mean flow. The primary internal tide has been removed by subtracting two snapshots at t and at $t + T_{tide}$, where T_{tide} is the tide period ($2\pi/\omega_0 \sim$12 hours). Linear characteristics for given frequencies are drawn on the snapshot at 5 days.

The transient phase lasts 3 to 5 days, corresponding to the development and the propagation of the primary tide toward the sponge layer. As early as 1.5 days of simulation, waves with smaller wavelengths appear throughout the water depth, faster than expected from upward propagation from topography (the group velocity of small-scale waves is slower than that of large-scale waves). This suggests that they are not generated at the topography during the transient phase, but instead are generated by nonlinearities at all heights. These figures visually confirm that a wide range of secondary waves are generated at the beginning of the simulation by nonlinearities.

2.4.2 Stage II: accumulation of inertial waves

Figure 2.8 shows the kinetic energy associated with the different frequencies in the simulation over the period 1-15 days and 15-30 days. During the first 15 days, the most energetic waves are associated to frequencies ω_0, the primary internal tide, f, the near-inertial wave and $\omega_0 - f$. There is a signal at $\omega = 0$ s^{-1}, probably linked to a weak mean flow induced by the waves [Grisouard and Bühler 2012]. During the second period, near-inertial waves have more and more energy and become stronger than the primary internal wave. The near-inertial waves are present above topography until 2 500 m, and have significant energy as high as 1 500 m above the bottom.

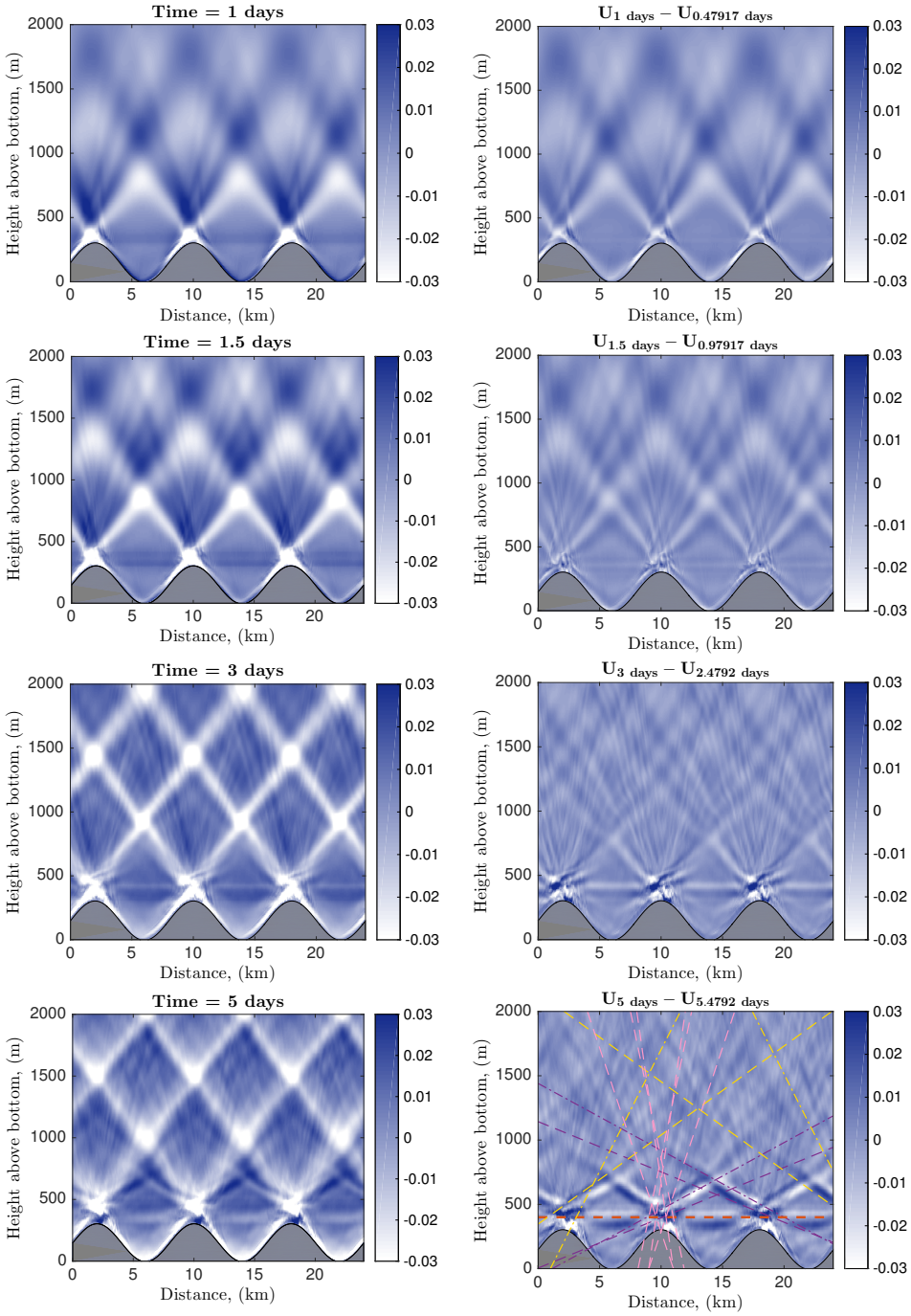

Figure 2.7: Snapshot of (left) the horizontal velocity (u, m s^{-1}) associated with the wave field and (right) the wave field without the primary internal tide signal at 0.5, 1.5, 3 and 5 days (right), for $f = 0.53 \times 10^{-4}$ s^{-1}. The wave field is obtained by subtracting the zonal mean flow. The primary internal tide has been removed by subtracting two snapshots at t and at $t + T_{tide}$, where T_{tide} is the tide period ($2\pi/\omega_0 \sim$12 hours). Dashed lines correspond to linear characteristics for waves at $(\omega_0 - f)$ (yellow dashed), $(\omega_0 + f)$ (yellow pointed dashed), $\omega_{1,\sigma max}$ (purple dashed), $\omega_{2,\sigma max}$ (purple pointed dashed), f (orange dashed) and for harmonics (pink dashed).

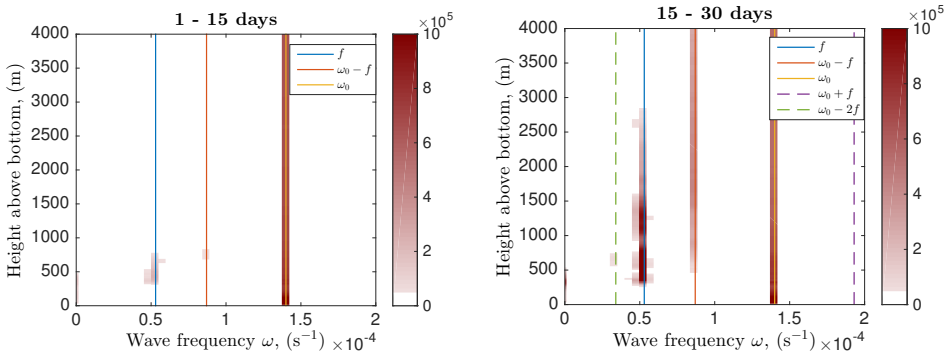

Figure 2.8: Kinetic energy spectrum in time (in m^2s^{-2}) as a function of wave frequency ω and height above topography, and averaged zonally over the time period of (left) 1-15 days and (right) 15-30 days, for $f = 0.53 \times 10^{-4}$ s^{-1}. Vertical lines correspond to the main observed frequencies. The colorbar is saturated to highlight the main secondary frequencies (beyond the primary wave tidal frequency ω_0).

Near-inertial waves (i.e. with frequencies near f) are those with vertical group velocity close to zero (in fact for inertial waves $\omega = f$, $k_{IW} = 0 \Rightarrow c_{g,z} = \partial\omega/\partial m = 0$, consistent with the horizontal characteristic lines seen for instance Figure 2.7). For this reason, they do not propagate upward or downward, and they accumulate near their generation site, growing to order one. Gradually, they accumulate and can not be considered as noise anymore compared to the primary internal wave.

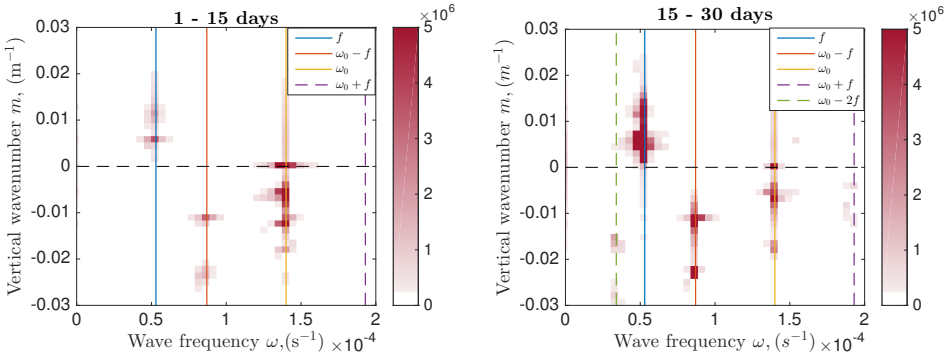

Figure 2.9: Kinetic energy spectrum in time and space (in m^2s^{-2}) as a function of wave frequency ω and vertical wavenumber m, and averaged zonally over the time period of (right) 1-15 days and (left) 15-30 days, for $f = 0.53 \times 10^{-4}$ s^{-1}. Vertical lines corresponds to the main observed frequencies. The colorbar is saturated to highlight the main frequencies.

Moreover, the sign of the vertical group velocity of internal waves,

$$Cg_z = -\frac{mk^2(N^2 - f^2)}{\omega(k^2 + m^2)^2}, \tag{2.9}$$

is minus the sign of the vertical wavenumber m (ω is positive with our convention). Figure 2.9 shows the kinetic energy of the waves as a function of vertical wavenumber

and frequency over 1-15 days and 15-30 days. As seen previously, near-inertial waves have more and more energy. The near-inertial waves are associated with a vertical wavenumber positive which means that the energy goes toward the topography and confirm the accumulation of near-inertial waves at the topography. We note in passing that the primary internal tide at ω_0 has a vertical wavenumber $m < 0$ implying a propagation upward which is coherent with their generation at the topography. After 15 days, near-inertial waves and primary internal tide are of the same order.

2.4.3 Stage III: dominant TRI

Consistent with the aforementioned accumulation of inertial waves, the wave field in the numerical simulation strongly evolves with time and the waves are very different after 19 days compared to earlier times (see Figure 2.10 right panel, where the primary internal tide has been removed). The linear characteristics highlight the waves at frequency $(\omega_0 - f)$ which dominate in the whole domain at the end of the simulation. The triad with waves at f and $\omega_0 - f$ has become order one and clearly dominates the wave field.

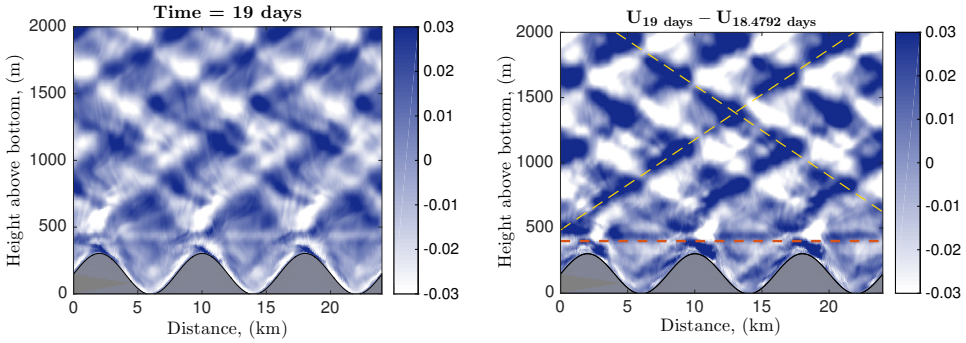

Figure 2.10: Snapshot of (left) the wave field and (right) the wave field without the primary internal tide signal at 19 days, for $f = 0.53 \times 10^{-4}$ s^{-1}. The wave field is obtained by subtracting the zonal mean flow. The primary internal tide has been removed by subtracting two snapshots at t and at $t + T_{tide}$, where T_{tide} is the tide period ($2\pi/\omega_0 \sim$ 12 hours). Dashed lines corresponds to linear characteristics for waves at $\omega_0 - f$ (yellow) and inertial waves f (orange).

In fact, if we come back to Figures 2.8 and 2.9, we can see that waves at $\omega_0 - f$ have more and more energy over time suggesting that their generation is linked to the strengthening of the near-inertial waves. Figure 2.9 also shows that waves at $\omega_0 - f$ have a vertical wavenumber $m < 0$ implying that they propagate upward and their energy is dissipated in the sponge layer. This result is coherent

with Figure 2.8 where $\omega_0 - f$ has homogeneous kinetic energy all over the water column above the maximum of f.

Going back to the TRI theory and triad selection, Figure 2.9 gives one more piece of information which is that the selected triad is the triad $(\omega_1 = \omega_0 - f, m_1 < 0)$ and $(\omega_2 = f, m_2 > 0)$. This triad is located on the right part of the upper unstable branch (see Figure 2.5 as well as Figure 2.11 left panel). Indeed, $m_1 < 0$ (same sign as m_0 on this branch), thus the triad selected corresponds to $\omega_1 = \omega_0 - f$ with $m_1 < 0$, open circles Figure 2.11. Note that in that case $m_2 > 0$ (since $|m_1/m_0| > 1$ see Figure 2.11) and the wave $\omega_2 = f$, $m_2 > 0$ thus propagates downward consistent with Figure 2.9 and the aforementioned accumulation of inertial waves at the topography.

Once near-inertial waves accumulate and become order one compared to the primary internal tide, they can interact with the internal tide, generating a new wave via TRI. The new wave frequency could be, with the combination of ω_0 and f, $(\omega_0 - f)$ or $(\omega_0 + f)$. If we go back to the triadic relation (Eq. 2.7), the only unstable branch corresponds to sign combination $(s_1 = +, s_2 = +)$, yielding $\omega_0 = \omega_1 + \omega_2$, with $\omega_{0,1,2}$ positive. This result implies that the only unstable triad is between frequencies ω_0, f and $\omega_0 - f$. In other words, the dominant TRI generates waves at frequency $(\omega_0 - f)$. This theoretical result is confirmed by the numerical simulation on Figure 2.10.

Thus we conclude that in our simulations, equatorward of the critical latitude, the dissipation of internal tides involves energy transfers to smaller scales (smaller frequencies) via TRI. More precisely, it occurs in three stages: generation of new secondary waves via TRIs over a wide range of frequencies, accumulation of inertial waves which can not propagate vertically, and domination of a TRI between the primary internal tide and inertial waves involving a third wave at $\omega_0 - f$. This theoretical and numerical study of internal tide instability and dissipation confirms the prediction that TRI is the main mechanism for internal tide dissipation in the ocean. We note that in the ocean, assuming that a steady state with the barotropic tidal forcing is reached, stages I and II are not relevant, and it is stage III, i.e. the interaction of internal tides with order one inertial waves, which dominates. We still need to explain how this dissipation mechanism can help explain the strong enhancement of dissipation at the critical latitude $f = \omega_0/2$.

2.4.4 Evolution of dissipation from the equator toward the critical latitude

Internal tide energy dissipation is not constant equatorward of the critical latitude (see Figure 2.2), it increases toward the critical latitude. In this section, we investigate the effect of the latitude on TRI growth rate and secondary waves, in order to investigate the reason behind the increase of dissipation at the critical latitude.

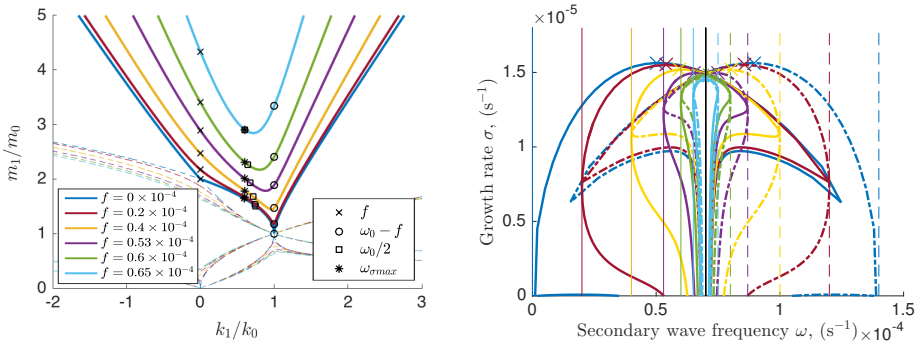

Figure 2.11: Location of (k_1, m_1) satisfying Equation 2.7 for the three possible combinations of signs for different latitudes. Plain curves are unstable branches. The associated growth rate as a function of the secondary wave frequencies are shown right panel. Vertical plain lines correspond to $\omega = f$ and vertical dashed lines to $\omega = \omega_0 - f$. Vertical black plain line indicates the critical latitude. Colored cross marks denotes maximum growth rate at each latitude.

Figure 2.11 shows for different latitudes the loci of TRI and the associated growth rate of the unstable branches as a function of the frequency of secondary waves. From the equator ($f = 0$ s^{-1}) toward the critical latitude, the unstable branch goes to infinite vertical wavenumbers and tightens. For the growth rate, it becomes sharper close to the critical latitude, tending to only generate inertial waves. In fact, at the critical latitude, only one resonant triad exists and both secondary waves have their frequencies equal to $\omega_0/2$. We call this specific TRI, the Parametric Subharmonic Instability (PSI) [Bouruet-Aubertot et al. 1995; Staquet and Sommeria 2002; Bourget et al. 2013]. The sharp increase as f approaches the critical latitude in Figure 2.2 is not explained by a change in the maximum growth rate, which remains roughly constant with f (crosses in the right panel of Figure 2.11). We now investigate whether the growth rate of the other triad involving waves at f and $\omega_0 - f$ can explain this sharp increase and whether changes in scales of the secondary waves may also play a role, as waves with smaller scales are more prone to break and dissipate their energy.

Figure 2.12 represents the latitudinal evolution of growth rate, horizontal wavenumber and vertical wavenumber for the key frequencies. From the equator

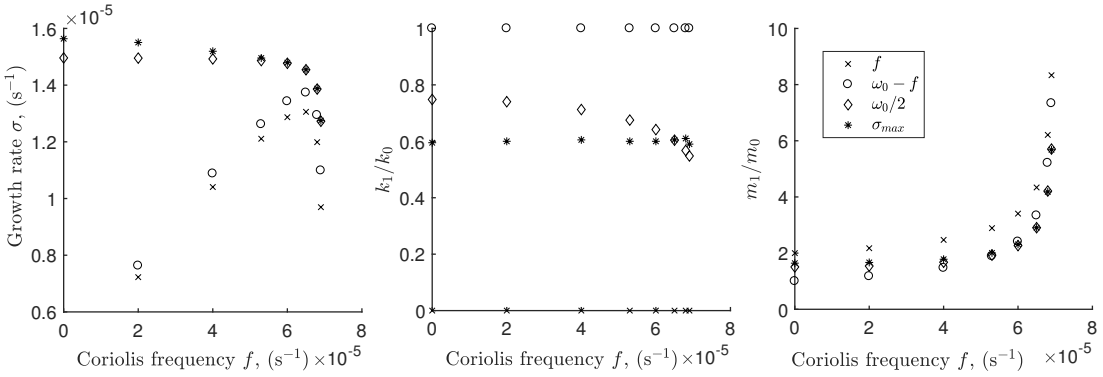

Figure 2.12: Latitudinal evolution of growth rate, horizontal wavenumber k_1, vertical wavenumber m_1 for different frequencies.

toward the critical latitude, we recover the fact that the maximum growth rate is roughly constant, and even decreases. But the growth rate of inertial waves and waves at $(\omega_0 - f)$ increases. The horizontal scales of the waves seem to be almost constant with latitude. On the other hand, the vertical wavenumber (vertical scale) increases (decreases) strongly getting closer to the critical latitude. TRIs promote the generation of inertial waves and waves at $\omega_0 - f$ close to the critical latitude, which have smaller and smaller vertical scales near the critical latitude promoting their dissipation. These theoretical results suggest that the enhanced energy dissipation at the critical latitude is due to faster generation (increased growth rate) of secondary waves with smaller vertical scales which are dissipated quickly after their generation, leading to the strong energy dissipation seen in Figure 2.2.

2.5 Part II - Poleward of the critical latitude: evanescent waves

Poleward of the critical latitude, TRI is not a possible mechanism for internal tide dissipation, since waves at $\omega_0 - f$ are not radiating internal waves anymore. But surprisingly, the dissipation does not decrease sharply. Instead, internal tides continue to dissipate for about 5° of latitude poleward (see Figure 2.2) and thus to participate in diapycnal mixing. The energy dissipation seems to be associated with waves at $\omega_0/2$ (see Figure 2.4) which are not radiating either ($\omega_0/2 < f$), but instead are evanescent in z. Young et al. [2008] propose a mechanism, the "2-f pump", which extends PSI theory poleward of the critical latitude. In Young et al. [2008] theory, the barotropic tide at ω_0 is able to exchange energy with near-inertial waves, leading to its dissipation. Here we compare expectations from this theory to our simulations.

2.5.1 Theory of PSI extension

In Young et al. [2008]'s theory, internal tides can transfer energy to evanescent secondary waves at $\omega_0/2$ via a mechanism called the $2f$-pump. As mentioned earlier, we refer to PSI as the specific TRI where resonant conditions are

$$\mathbf{k_0} = \mathbf{k_1} + \mathbf{k_2}, \tag{2.10}$$

$$\omega_0 = \omega_1 + \omega_2 = \frac{\omega_0}{2} + \frac{\omega_0}{2}. \tag{2.11}$$

Young et al. [2008] studied near-inertial PSI which corresponds to a case where the primary wave has a frequency $\omega_0 \approx 2f$, where f is the local inertial frequency, inducing that secondary waves are near-inertial oscillations. Transfer of energy in this mechanism is particularly efficient because near-inertial oscillations are almost stationary and therefore might dissipate locally.

Young et al. [2008] show that an infinite plane wave at frequency $\omega_0 = 2f+\epsilon$, ($\epsilon \ll f$ and ϵ can be positive or negative), extracts energy from the non-geostrophic part of the background flow then transferring to near-inertial oscillations via near-inertial PSI. If the de-tuning frequency ϵ is negative, which means secondary waves at $\omega_0/2$ fall outside the internal wave frequency band $[f, N]$, Young et al. [2008] point that PSI can extend the internal wave frequency band to slightly subinertial frequencies.

The growth rate of the near-inertial PSI of an infinite-plane internal wave $\omega_0 = 2f + \epsilon$, on the f-plane, is (see appendix B for the full growth rate calculation and e.g. Muller and Bühler [2009] for polarization relations (their Equation 9) used to determine the amplitude of the 2-f pump in our simulations):

$$\sigma = \frac{1}{2}\sqrt{\lambda^2 - \left(\frac{N^2}{2f}\right)^2 \left(\frac{k_1^2}{m_1^2} + \frac{k_2^2}{m_2^2} - 2\frac{\epsilon f}{N^2}\right)^2}, \tag{2.12}$$

where

$$\lambda^2 = \frac{U_0 h_0 k_0^2}{2\omega_0}\sqrt{\frac{(N^2 - \omega_0^2)(\omega_0 + f)}{(\omega_0 - f)}} \tag{2.13}$$

Figure 2.13 represents the growth rate from Equation (2.12) for different latitudes. The growth rate of near-inertial PSI is maximum at the critical latitude ($f = 0.7 \times 10^{-4}$ s^{-1}) and decreases poleward of the critical latitude. A second important point is that the instability is larger at higher vertical wavenumber (small vertical scales). This last result is consistent with the strong dissipation observed near and poleward of the critical latitude (see Figure 2.2), since dissipation is favored by

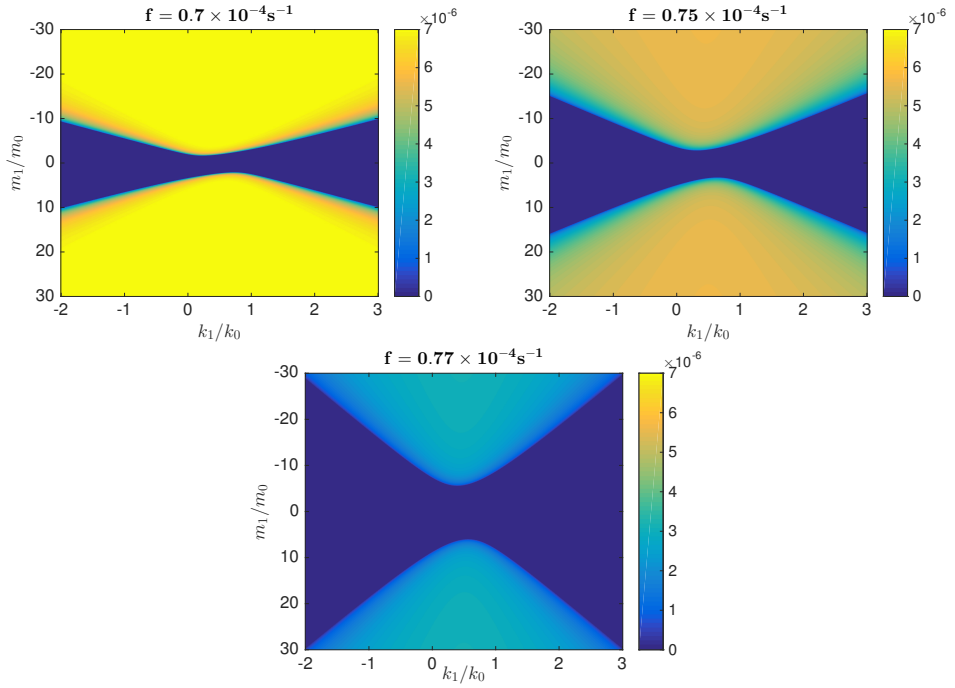

Figure 2.13: Growth rate (in s^{-1}) from (2.12) as a function of m_1/m_0 and k_1/k_0 for different latitudes: $f = 0.7 \times 10^{-4}$ s^{-1}, $f = 0.75 \times 10^{-4}$ s^{-1} and $f = 0.77 \times 10^{-4}$ s^{-1}.

smaller-scale waves. When $m_1/m_0 \to \infty$, the growth rate asymptotes to $\frac{1}{2}\sqrt{\lambda^2 - \epsilon^2}$. From this result, we can evaluate ϵ_c when the growth rate is zero. We obtain $\epsilon_c/f \approx 0.2$ which extends the dissipation poleward of the critical latitude to $f \approx 0.77 \times 10^{-4}$ s^{-1} ($\sim 32°$). This result is in excellent quantitative agreement with the latitudinal extent of enhanced dissipation poleward of the critical latitude found in our simulations Figure 2.2. Further comparison with our numerical results are provided in the next section.

2.5.2 Numerical results

Figure 2.14 is a snapshot of the wave field at 19 days (primary internal tide removed) for a simulation poleward of the critical latitude ($f = 0.75 \times 10^{-4}$ s^{-1}). We draw the characteristics of linear waves at $\omega_0/2$, showing the presence of these near-inertial waves. These near-inertial waves are confined to a few hundred meters from topography, as expected since these are evanescent in the vertical. Consistent with Figure 2.2 and with the theoretical latitude of zero growth rate derived at the end of the previous section, we find that those near-inertial waves at $\omega_0/2$ are present approximately until $f = 0.8 \times 10^{-4}$ s^{-1}. These results suggest that poleward of the critical latitude, the dissipation of internal tides is dominated by this extension of PSI, namely the 2f-pump mechanism. In other words, we find

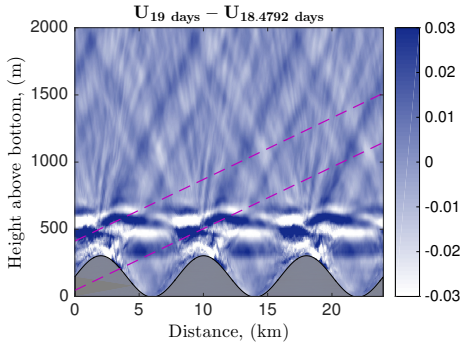

Figure 2.14: Snapshot of the wave field after removing the primary internal tide at 5 days, for $f = 0.75 \times 10^{-4}$ s^{-1}. The wave field is obtained by subtracting the zonal mean flow. Dashed lines corresponds to linear characteristics for waves at $\omega_0/2$ (purple).

that the generation of evanescent waves via nonlinear energy transfers from the primary internal tide, is an efficient process to dissipate tidal energy. Though PSI has been widely studied, the transfer of energy to evanescent waves has not received as much attention, while our work suggests that it could be an equally efficient mechanism to dissipate tidal energy near the critical latitude.

2.6 Discussion and conclusions

In this paper, we investigate the physical processes responsible for the dissipation of internal tides. In particular, we want to determine which physical process, if any, dominates in setting the latitudinal distribution of tidal dissipation and the strong enhancement of energy dissipation at the critical latitude $f \approx 0.7 \times 10^{-4}$ s^{-1} (Figure 2.2). Our results suggest that the physical process behind the dissipation of internal tides is different equatorward and poleward of the critical latitude.

Equatorward of the critical latitude, triadic resonant instabilities are the most efficient mechanism to transfer energy from the primary wave, i.e. the internal tide, to secondary waves. These secondary waves have lower frequencies than the primary wave, hence smaller vertical scales, and are more prone to dissipate. In our simulations, this mechanism involves three stages after the generation of the primary internal tide: generation of secondary waves at various frequencies via TRI, accumulation of near-inertial waves close to the topography (because of their small vertical group velocity) and when inertial waves become of the same order than the primary internal tide, triadic interaction between the primary wave at ω_0 and inertial waves at f leads to the generation of waves at $\omega_0 - f$. In the ocean only the last stage is relevant, if we consider that the ocean has reached a steady state. Internal tides and inertial waves are of the same order, and they interact

nonlinearly to generate waves at $\omega_0 - f$. TRI is found to be a powerful mechanism to extract tidal energy. The increase of energy dissipation from the equator toward the critical latitude is due to increased instability growth rates, as well as to the smaller and smaller vertical scales of the secondary waves (Figure 2.12), hence more likely to break and dissipate their energy.

Poleward of the critical latitude, the "2f-pump" mechanism described in Young et al. [2008] seems to be the leading order mechanism by which internal tides lose energy. In this case, the internal tide transfers energy nonlinearly to evanescent waves at frequencies $\omega_0/2$, which dissipate internal tide energy as efficiently as PSI equatorward of the critical latitude. In fact, the 2f-pump is an extension of PSI poleward of the critical latitude when we consider near-inertial waves $(f + \epsilon)$ for small values of ϵ. The strong dissipation poleward of the critical latitude has implications for the possible consumption of AABW. These results suggest that evanescent waves could play a leading order role in the dissipation of tidal energy in the deep ocean poleward of the critical latitude, and could contribute significantly to the diapycnal mixing relevant to the large-scale ocean circulation and to water masses.

Acknowledgments

We acknowledge CINES/GENCI, France, for providing access and support to their computing platform OCCIGEN, as well as the PRACE Research Infrastructure computing resource Curie based in France at TGCC. CJM gratefully acknowledges funding from the ANR LEFE program and the ENS Actions Incitatives program.

3

Impact of a Mean Current on the Internal Tide Energy Dissipation at the Critical Latitude

This project describes the effect of a mean current on the local dissipation of semi-diurnal tide (M2). Without a mean current, the dependence of internal tide energy dissipation on latitude is strong and strongly enhanced at the critical latitude in the numerical studies. This enhancement is not as strong in oceanic measurements. Here we explore the possible explanation for this discrepancy between simulations and observations. One possibility is the presence of mean currents, such as large-scale oceanic currents or mesoscale eddies, which can perturb the propagation and the dissipation of the waves.

Bill Watterson, 18 June 1993

JUNE 2017 RICHET ET AL. 1457

Impact of a Mean Current on the Internal Tide Energy Dissipation at the Critical Latitude

O. RICHET, C. MULLER,[a] AND J.-M. CHOMAZ

LadHyX, Ecole Polytechnique, Palaiseau, France

(Manuscript received 24 August 2016, in final form 12 January 2017)

ABSTRACT

Previous numerical studies of the dissipation of internal tides in idealized settings suggest the existence of a critical latitude (~29°) where dissipation is enhanced. But observations only indicate a modest enhancement at this latitude. To resolve this difference between observational and numerical results, the authors study the latitudinal dependence of internal tides' dissipation in more realistic conditions. In particular, the ocean is not a quiescent medium; the presence of large-scale currents or mesoscale eddies can impact the propagation and dissipation of internal tides. This paper investigates the impact of a weak background mean current in numerical simulations. The authors focus on the local dissipation of high spatial mode internal waves near their generation site. The vertical profile of dissipation and its variation with latitude without the mean current are consistent with earlier studies. But adding a weak mean current has a major impact on the latitudinal distribution of dissipation. The peak at the critical latitude disappears, and the dissipation is closer to a constant, albeit with two weak peaks at ~25° and ~35° latitude. This disappearance results from the Doppler shift of the internal tides' frequency, which hinders the nonlinear transfer of energy to small-scale secondary waves via the parametric subharmonic instability (PSI). The new two weak peaks correspond to the Doppler-shifted critical latitudes of the left- and right-propagating waves. The results are confirmed in simulations with simple sinusoidal topography. Thus, although nonlinear transfers via PSI are efficient at dissipating internal tides, the exact location of the dissipation is sensitive to large-scale oceanic conditions.

3.1 Introduction

In the abyssal ocean, away from boundaries where exchanges with the atmosphere or land can occur, the largest buoyancy forcing happens via mixing. In the ocean interior, observations indicate that diapycnal mixing (mixing across isopycnals) is largely dominated by the breaking of internal waves [Polzin et al. 1997; Ledwell et al. 2000; Waterhouse et al. 2014]. Internal waves are ubiquitous in the ocean [Garrett and Munk 1979]. They transport energy, and when they become unstable and break, they dissipate this energy, thereby contributing to mixing oceanic water masses. This mixing is strongly inhomogeneous in space and time, but its distribution remains poorly understood. Uncertainties in the spatial distribution of wave-energy dissipation and concomitant diapycnal mixing, limit our ability to understand the ocean global circulation and water mass formation, especially deep waters whose isopycnals do not outcrop at high latitudes [Talley 2013; Ferrari 2014].

Numerous studies show the impact of inhomogeneous mixing on the abyssal circulation, from idealized models [Samelson 1998; Nikurashin et al. 2012; Mashayek

et al. 2015] to more realistic global ocean models [Jayne 2009; Munday et al. 2011; Melet et al. 2016]. Global climate models do not resolve processes associated with internal waves, which are therefore parameterized. The consumption of Antarctic Bottom Water (AABW, dense cold bottom water mass formed in Antarctica) in the ocean interior is strongly influenced by wave-induced diapycnal mixing [Talley 2013; Melet et al. 2016]. It is primarily influenced by internal tides [Nikurashin and Ferrari 2013; De Lavergne et al. 2016b;a], which are internal waves generated by barotropic tidal currents flowing above topography (see Garrett and Kunze [2007] for a review). Depending on the spatial distribution of internal tides dissipation and the induced mixing, estimates of AABW upwelling differ by a factor 2 or more [De Lavergne et al. 2016b].

One major uncertainty is the vertical profile of the internal tides dissipation. To leading order, its maximum height, which determines the depth of the AABW return flow to the Southern Ocean along isopycnals [Ferrari 2014], is dictated by the topographic height [Nikurashin and Ferrari 2013], since dissipation is strongly localized near topography. Nevertheless, vertical profiles with enhanced dissipation up to 500 m or 1 km above topography have been found in numerical studies [Nikurashin and Legg 2011]. Along with the Antarctic latitudinal extent of ice cover, the height of dissipation dictates exchanges with the atmosphere (carbon dioxide, oxygen, etc) in the Southern Ocean, and hence largely determines the carbon storage in the deep ocean [Ferrari et al. 2014]. Another major uncertainty is the fraction of internal tide energy which dissipates locally near the seafloor upon generation, and the remaining fraction of internal tides which escape and are hence available to dissipate remotely. The latter could contribute as low as 1 Sv and as high as 28 Sv of AABW upwelling depending on their energy and vertical dissipation profile [De Lavergne et al. 2016b]. Understanding internal tides sources, mechanisms of energy transfers and the resulting mixing, are therefore crucial steps to understand the global distribution of temperature, salinity and biogeochemical tracers in the abyssal ocean, and to improve the representation of wave-induced mixing in climate models.

Mechanisms of internal tides breaking are not well understood, and several mechanisms have been proposed. These include breaking through convective or shear instability [Muller and Bühler 2009], scattering by the bottom [Müller and Xu 1992] and the thermocline [Gerkema 2001], critical reflection [Gemmrich and Klymak 2015], scattering by mesoscale features [Rainville and Pinkel 2006], or energy transfer to smaller scales via nonlinear wave-wave interactions [Polzin 2009; MacKinnon and Winters 2005]. It is believed that internal tides with small scales (high spatial modes,

generated by topography with horizontal scales below 10 km or so) are dissipated near their generation site [St. Laurent and Garrett 2002; Muller and Bühler 2009; Lefauve et al. 2015], while waves with larger scales (low spatial modes) generated at large topographic features (e.g. the Hawaiian ridge) can propagate thousands of kilometers across oceanic basins [Hazewinkel and Winters 2011]. We focus on the local dissipation of internal tides near their generation site. Of particular interest is the latitudinal distribution of the local dissipation (high-mode internal tides).

Recent idealized simulations show that the latitudinal distribution of tidal mixing may be largely determined by an instability known as the Parametric Subharmonic Instability (PSI). PSI is the class of resonant wave-wave nonlinear interactions wherein energy is transferred from large scales to smaller scales, and where the frequencies of the secondary waves are near half the primary frequency [Bouruet-Aubertot et al. 1995; Staquet and Sommeria 2002; Bourget et al. 2013]. When the primary waves are internal tides generated at the tidal frequency ω_0 (about twice a day for the largest semi-diurnal lunar tide), PSI yields two secondary waves through nonlinear interactions with frequency $\omega_0/2$. Both idealized numerical studies of low [MacKinnon and Winters 2005] and high [Nikurashin and Legg 2011] modes find a large enhancement of the dissipation of internal tides at a critical latitude of $\sim 29^\circ$ ($f = 0.7 \times 10^{-4}$ s^{-1}). This corresponds to the latitude where the frequency of the secondary waves $\omega_0/2$ matches the Coriolis frequency $f = 2\Omega \sin\phi$, where Ω denotes the Earth rotation rate and ϕ latitude. In other words, the secondary waves at the critical latitude are near-inertial waves. The secondary waves have frequencies lower than the primary waves, hence smaller scales.

On the other hand, observations only indicate a modest enhancement of dissipation at the critical latitude [Alford et al. 2007; MacKinnon et al. 2013], at least for low mode internal tides. Indeed these observations were not deep enough to capture the high modes discussed in Nikurashin and Legg [2011]. In other words, observations of low modes do not confirm the “catastrophic" dissipation that numerical studies of low modes [MacKinnon and Winters 2005] and high modes [Nikurashin and Legg 2011] suggest. For the low mode internal tides propagating away from their generation site, it was suggested that the time scale of PSI may be too slow to significantly impact the propagating low-mode wave packet as it crosses the critical latitude [Hazewinkel and Winters 2011]. But for the high-mode internal tides whose group velocities are smaller and who are continuously generated near the seafloor, PSI could significantly impact their local dissipation. This is the question addressed here, namely what role does PSI play in the local dissipation of internal tides near their generation site? In particular, do we expect the enhanced

dissipation at the critical latitude observed in the idealized simulations of Nikurashin and Legg [2011] under more realistic oceanic conditions?

In order to address these questions, we investigate whether the presence of a background mean current can impact the enhanced local dissipation at the critical latitude. Indeed, internal tides do not propagate through a quiescent ocean. Large-scale currents or mesoscale eddies are ubiquitous in the ocean and can yield currents with amplitudes comparable to or larger than the barotropic tide [Nikurashin and Ferrari 2011]. This mean current can interact with internal tides and modify their propagation and dissipation. In this paper we investigate the impact of a weak mean current, with an amplitude on the order of the barotropic tide, on the high-mode internal tides dissipation.

Section 2 describes the numerical model used and the setting. Section 3 presents results first without a mean current, reproducing the main results of [Nikurashin and Legg 2011], and second with a mean current whose impact is discussed. In section 4, we validate the hypothesis of a Doppler effect with idealized simulations of internal tides generated by simple monochromatic sinusoidal topography. Conclusions and implications for the large-scale circulation are discussed in section 5.

3.2 Methods

3.2.1 Numerical model

Our goal is to investigate the impact of a mean current on the resonant dissipation found at the critical latitude in the simulations of Nikurashin and Legg [2011]. We therefore follow their methodology and use the same numerical model in similar settings. Namely, we use the Massachussetts Institute of Technology general circulation model (MITgcm; Marshall et al. [1997]) a high-resolution numerical model in nonhydrostatic configuration. The nonhydrostatic configuration allows the explicit representation of processes such as hydraulic jumps or Kelvin-Helmholtz instabilities. The MITgcm solves the equations of an incompressible fluid under the Boussinesq approximation. The model is developed with the finite volume techniques to provide the treatment of irregular geometries like the topography using the MITgcm partial cells architecture. The bottom boundary is treated with a no-slip condition.

The main characteristics of the domain are synthesized on Fig. 3.1. The domain is two-dimensional with horizontal periodicity in the x direction. The horizontal size of the domain is 60 km with a uniform resolution of $\Delta x = 30$ m and the total vertical extent is 7.5 km. The 4.5 km bottom layer has a uniform resolution of

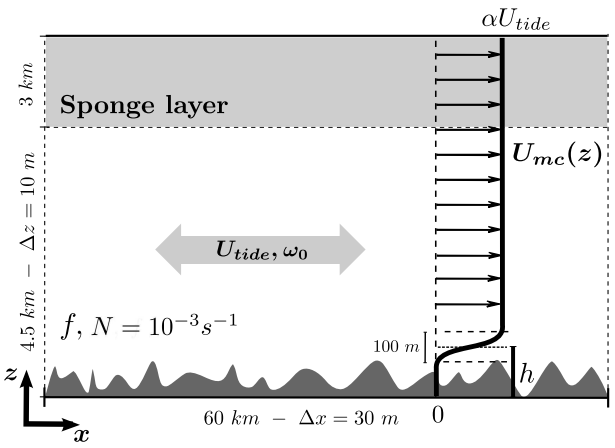

Figure 3.1: Schematic of the numerical setup. The barotropic tidal current, with amplitude U_{tide} and frequency ω_0, interacts with a one-dimensional realistic topography in a stratified (N constant) and rotating (f varying with latitude) fluid. The mean flow U_{mc} has an amplitude equal to zero below the maximum of topography and reaches an amplitude αU_{tide} 100 m above the maximum of topography. The parameter α governing the relative strength of the mean current varies between 0 and 1 in the various simulations. The gray shaded layer at the top of the domain corresponds to the sponge layer.

$\Delta z = 10$ m. The last upper 3 km form the sponge layer where the resolution is progressively stretched from $\Delta z = 10$ m to $\Delta z = 70$ m. The model time step is 30 seconds. Although two-dimensional ($\partial/\partial y \equiv 0$), we allow for a velocity v constant in the y direction. As in Nikurashin and Legg [2011], these high-resolution idealised simulations are designed to allow the resolution of a wide range of spatial and temporal scales of the turbulence.

We are interested in the local dissipation of internal tides near their generation site, so we neglect reflection at the ocean surface and assume a semi-infinite ocean. We therefore add the sponge layer at the top of the domain to absorb the upward propagating waves which do not dissipate locally, and whose remote dissipation would require further investigation beyond the scope of this study. In the sponge layer, buoyancy and momentum are damped with a linear drag with a time scale of 1 hour.

3.2.2 Settings

In the simulations, the fluid is linearly stratified in the vertical with constant buoyancy frequency $N = 10^{-3}$ s^{-1} representative of the deep ocean stratification. The Coriolis frequency is varied with varying latitude, to investigate the latitudinal variation of internal tides dissipation. At the critical latitude 28.8°, $f = 0.7 \times 10^{-4}$ s^{-1}. The horizontal and vertical viscosities and diffusivities are set to $\nu_h = \nu_v =$

2×10^{-3} m^2 s^{-1} and $\kappa_h = \kappa_v = 10^{-4}$ m^2 s^{-1} (values close to the ones used in Nikurashin and Legg [2011], who found that the energy dissipation profiles are robust to reasonable changes of these values). All simulations are initiated from a state at rest and run for 30 days (a statistically steady state is reached in 5 to 10 days depending on the simulation).

3.2.3 Topography

Following Nikurashin and Legg [2011], we focus on tidal generation in the Brazil Basin where high levels of mixing have been observed [Polzin et al. 1997; Waterhouse et al. 2014] and are attributed to internal tides breaking. In the Brazil Basin, the Mid-Atlantic Ridge (MAR) is almost oriented East-West. Abyssal ridges are anisotropic and elongated perpendicular to the direction of spreading. For this reason and in the case of the MAR, the roughest topography is oriented almost South-North and a 2D numerical model in this direction is a good first approximation for wave generation. Topographic variability associated with abyssal hills is described by a one-dimensional topography spectrum obtained by integrating the two-dimensional spectrum of Goff and Jordan [1989] (see also Goff and Arbic [2010])

$$H(k,l) = \frac{4\pi\nu h^2}{k_0 l_0}\left(\frac{k^2}{k_0^2} + \frac{l^2}{l_0^2} + 1\right)^{-(\nu+1)} \tag{3.1}$$

along the smooth direction (see Muller and Bühler [2009]; Nikurashin and Legg [2011] for more details about the one-dimensional topography computation). The topography used in § 3.3 is designed to have this observed spectrum with parameters from the Brazil basin: root mean square (rms) height $h = 110$ m, high wavenumber slope $\nu = 0.90$, and roll-off wavenumber $k_0 = 1.0 \times 10^{-3}$ m^{-1}.

In § 3.4, additional simulations with idealized sinusoidal topography will be performed. The sinusoidal topography is designed to have similar vertical and horizontal Froude numbers as the realistic topography, $Fr_v = U_{tide}/Nh \approx 10^{-1}$ and $Fr_h = U_{tide}/(N2\pi/k_0) \approx 4 \times 10^{-3}$ respectively, where U_{tide} denotes the amplitude of the barotropic tide (see next section for more details). This ensures that we keep the same flow regimes. We note in passing that holding Fr_h and Fr_v constant implies that both the ratio of the wave slope to topography slope $\approx \frac{\omega/N}{h/(2\pi/k)}$, and the tidal excursion $\frac{U/\omega}{2\pi/k}$ are kept constant, since ω and N are the same in all simulations. Hence, the rms height of the sinusoidal topography is set to $h = 110$ m , and the horizontal wavenumber is equal to $k_0 \approx 0.8 \times 10^{-3}$ m^{-1}.

3.2.4 Tidal and mean currents imposed

The tidal barotropic flow is forced by adding a body force to the momentum equations, yielding a barotropic semi-diurnal lunar M_2 tide $U(t) = U_{tide}\sin(\omega_0 t)$ with amplitude $U_{tide} = 2.5$ cm s^{-1} and frequency $\omega_0 = 1.4 \times 10^{-4}$ s^{-1}. In some of the simulations, a mean current U_{mc} is also imposed. To allow waves to feedback on the mean current, we do not use relaxation towards an imposed profile, but instead we impose a geostrophic current by adding a meridional pressure gradient. Our goal is to investigate the impact of this mean current on the propagation of waves, not on their generation. We therefore only add the mean current above topography, and increase the amplitude of U_{mc} from 0 at the maximum height of topography to αU_{tide} a hundred meters above that height using a smooth arctan profile (see Appendix C for more details about the few lee waves generated by the mean current intersecting the highest topographic features and the negligible energy dissipation associated with those). The parameter α is varied between 0 and 1 in the different simulations, to assess the impact of the relative amplitude of the mean current on the internal tides. The vertical profile of the mean current U_{mc} is shown in Fig. 3.1.

As noted above, our goal is to investigate the impact of the mean current on the internal tides and their energy dissipation to secondary waves via PSI. We therefore need to make sure that the 100 m vertical shear layer does not impact significantly the upward-propagating internal tides before they reach the mean current region. Two possible undesirable effects of the shear layer can destabilize the primary waves and prevent their upward-propagation: shear instability and/or a critical layer. Empirically, we will see that the energy dissipation is not enhanced in the shear layer, implying that the waves can propagate through and past the shear layer.

This is expected theoretically since shear instability is determined by the non-dimensional Richardson number $Ri = N^2/(\partial u/\partial z)^2 \geq 4$ for a 100 m thick shear layer and $0 \leq \alpha \leq 1$ (strength of the mean current). Hence $Ri > 1/4$ ensuring stability in the shear layer. The second possible source of dissipation are critical levels, where the mean current matches the horizontal phase speed $c = \omega_0/k$ of the internal tides [Booker and Bretherton 1967; Maslowe 1986]. At critical levels, the momentum of the waves is transferred to the mean flow and the waves are attenuated. The non-dimensional parameter relevant in that case is $U/c = Uk/\omega_0$, which is the so-called tidal excursion [Garrett and Kunze 2007], typically below unity in the ocean. In our simulations $U/c = \mathcal{O}(10^{-1})$ ensuring stability through the shear layer. We therefore expect the internal tides generated at the topography to propagate upward past the shear layer into the mean-current region $U \equiv U_{mc}$ of interest.

3.3 Results: realistic topography

In this section, we investigate the dissipation of internal tides generated by realistic topography, without and with mean current. We start by reproducing the peak of tidal dissipation at the critical latitude found by Nikurashin and Legg [2011] (our control simulations). In these control simulations, the only forcing is the barotropic tide. We then add a mean current and investigate whether the enhanced dissipation at the critical latitude is robust or altered.

3.3.1 Control case: tidal energy transfer without mean current

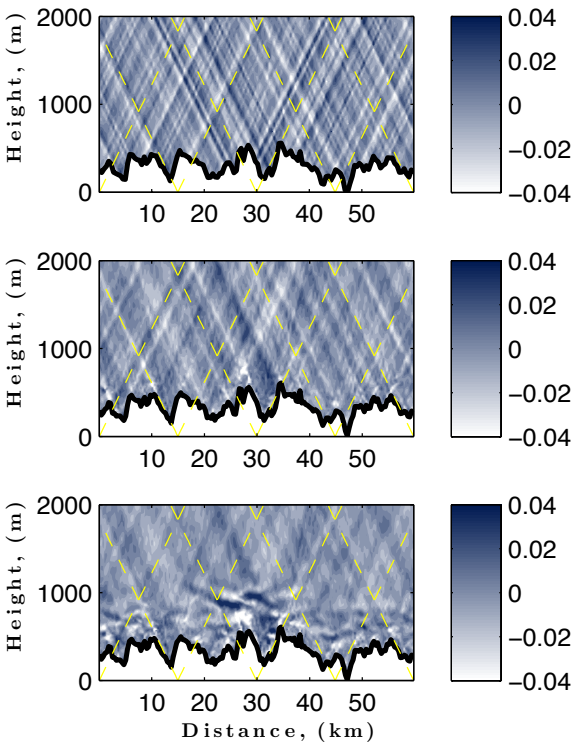

Figure 3.2: Snapshots of the wave zonal velocity (m s^{-1}) from the control simulation without mean current at the critical latitude ($f = 0.7 \times 10^{-4}$ s^{-1}, $\alpha = 0$) after 5 days (middle) and 19 days (bottom) of simulation. The linear solution is also shown for comparison (top), as well as wave characteristics from the linear theory dispersion relation (dashed yellow lines).

Fig. 3.2 shows snapshots of the zonal velocity anomaly (deviation from the zonally averaged flow) at 5 and 19 days in the control simulation at the critical latitude ($f = 0.7 \times 10^{-4}$ $s^{-1}, \alpha = 0$). In the simulations, internal tides are generated

at the topography as the barotropic tide oscillates back and forth. As these waves propagate into the ocean interior, they either break and dissipate, or propagate all the way to 4.5 km above which they are absorbed in the sponge layer. Internal tides typically take 5-10 days to reach the sponge layer (depending on their scales, larger scales propagating faster). This time corresponds to the establishment of a stationary wave field in the ocean interior, where the energy input from the barotropic tide is equilibrated by the energy output into wave dissipation in the ocean interior or wave damping in the sponge layer.

At day 5, the generation of internal tides is in good agreement with linear theory, shown in the top panel [Bell 1975; Muller and Bühler 2009]. The dashed yellow lines repeated in all the panels indicate the linear wave slopes $k/m = \pm\sqrt{(\omega_0^2 - f^2)/(N^2 - \omega_0^2)}$. The observed wave field is the multichromatic superposition of plane waves generated at the various wavelengths of the topography spectrum. Note that from their dispersion relationship, internal waves propagate with a slope determined solely by their temporal frequency, ω_0 for waves generated at the fundamental tidal frequency, which clearly dominate the wave field here (we can also observe some higher harmonics with frequency $2\omega_0$ and accordingly steeper slopes).

After 19 days, the wave field has largely diverged from linear theory, and horizontal waves appear. This is consistent with the results of Nikurashin and Legg [2011] who show that nonlinear interactions spontaneously generate secondary waves at $\omega_0/2$, which is equal to f at the critical latitude. The horizontal waves observed towards the end of the simulation on Fig. 3.2 are those secondary near-inertial waves. They largely dominate the wavefield at day 19, consistent with earlier results in the literature that the transfer of energy from the primary wave at ω_0 to secondary waves at $\omega_0/2$ is maximum when there is resonance with $f = \omega_0/2$, i.e. at the critical latitude.

The energy dissipation rate diagnosed from the control simulation is shown in Fig. 3.3 (blue plain curve) and compared to dissipation rate at other latitudes (blue dashed and dotted curves). The dissipation rate is computed as

$$\epsilon = \nu_i \left\langle \left(\frac{\partial u_j}{\partial x_i}\right)\left(\frac{\partial u_j}{\partial x_i}\right)\right\rangle, \tag{3.2}$$

where ν is viscosity, u is velocity, $\langle . \rangle$ denotes zonal and temporal mean and repeated indices are understood as sums. The dissipation rate is averaged over the last 10 days of simulation. The vertical dissipation profiles obtained at different latitudes (plain line $f = 0.7 \times 10^{-4}$ s^{-1}, dotted line $f = 0.53 \times 10^{-4}$ s^{-1} and dashed line

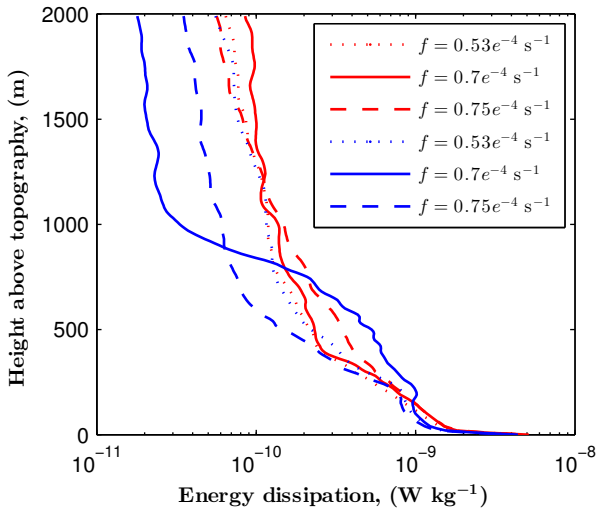

Figure 3.3: Profiles of energy dissipation rates averaged zonally and over the last 10 days of the simulations. Blue profiles correspond to simulations with $\alpha = 0$ (no mean current) and red profiles to simulations with $\alpha = 1$ (mean current).

$f = 0.75 \times 10^{-4}$ s^{-1}) exhibit 3 distinct regions. The first one extends a few tens of meters above topography, where, for all latitudes, the energy dissipation is enhanced up to $O(10^{-8})$ W.kg^{-1}. This region corresponds to the bottom boundary layer where energy dissipation is sustained by nonlinear effects such as flow separation from topography, hydraulic jumps, and direct breaking of the smallest-scale internal tide $O(50)$ m or less (not shown). The second one is the region above the bottom boundary layer until the first kilometer above topography. In this region, the energy dissipation profile at the critical latitude ($f = 0.7 \times 10^{-4}$ s^{-1}) is different from those obtained at the other latitudes ($f = 0.53 \times 10^{-4}$ s^{-1} and $f = 0.75 \times 10^{-4}$ s^{-1}), with a one kilometer thick "pocket" of enhanced dissipation. Dissipation is enhanced up to $O(10^{-9})$ W.kg^{-1} at a height of 500 m above topography. This is consistent with Fig. 3.2: at the critical latitude tidal energy is transferred efficiently to near-inertial frequencies via PSI, while at the other latitudes the instability is not as efficient at transferring energy to near-inertial waves. The third and last region is higher than 1 km above topography. The energy dissipation is close to the background value of $O(10^{-10})$ W.kg^{-1}, except at the critical latitude where the energy dissipation falls to $O(10^{-11})$ W.kg^{-1} as in Nikurashin and Legg [2011].

The vertically-integrated energy dissipation over the bottom 50 m, and from 50m to 2 km above topography, are shown for several latitudes in Fig. 3.4 (blue curves). Consistent with the above results and earlier studies, the bottom energy dissipation (50 m from topography) is largely insensitive to f, while the energy

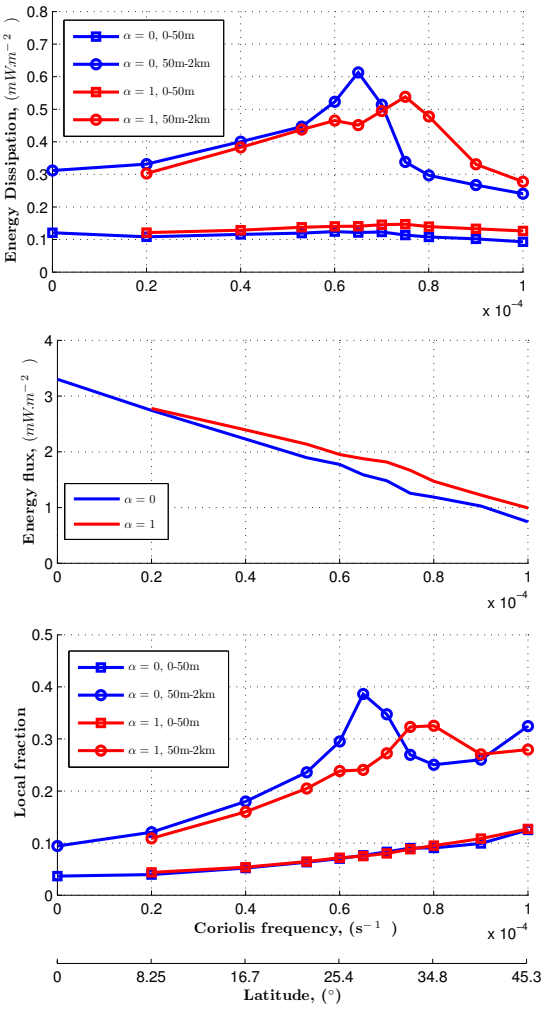

Figure 3.4: (Top) Energy dissipation rate integrated in the bottom 50 m (squares) and between 50 and 2 km (circles). (Middle) Energy flux at the topography. (Bottom) Energy dissipation expressed as a fraction of the energy flux at the topography. Blue curves correspond to simulations without mean current ($\alpha = 0$) and red curves to simulations with mean current ($\alpha = 1$, note that in that case $f = 0$ is not shown since a mean current can not be imposed via geostrophy with $f = 0$, see Methods for details).

dissipation above the bottom boundary layer is strongly dependent on the Coriolis frequency. It increases from near the equator ($f = 0.2 \times 10^{-4}$ s^{-1} $\implies$ $\epsilon \approx 0.3$ mW.m^{-2}) to the critical latitude ($f = 0.7 \times 10^{-4}$ s^{-1} $\implies$ $\epsilon \approx 0.6$ mW.m^{-2}) and decreases rapidly poleward ($f = 1 \times 10^{-4}$ s^{-1} $\implies$ $\epsilon \approx 0.2$ mW.m^{-2}). The energy flux at the topography, defined as the vertical wave energy flux $p'w'$ averaged over the surface bounding the topography

$$EF = \left\langle \frac{\int p'w' \mathrm{d}x \ \mathrm{d}y}{\int \mathrm{d}x \ \mathrm{d}y} \right\rangle_T \tag{3.3}$$

where p' and w' are pressure and vertical velocity zonal anomalies and $\langle . \rangle_T$ denotes

the time average between 5th and 15th tidal periods, is shown in the middle panel in Fig. 3.4. It decreases with latitude (consistent with the linear theory which predicts $EF \propto \sqrt{\omega_0^2 - f^2}$ decaying with f [Muller and Bühler 2009]). The local dissipation fraction, shown in the bottom panel in Fig. 3.4 and defined as the energy dissipation vertically integrated normalized by the energy flux at the topography, increases from 10% at the equator (latitude 0) to 40% at the critical latitude (28.8°) and decreases to 25-30% at higher latitudes. In other words, our simulations so far confirm the results from earlier studies that the critical latitude may serve as a "hotspot" for tidal dissipation.

3.3.2 Impact of a mean current on energy dissipation

We now investigate the impact of a mean current on the radiation and breaking of internal tides. As noted in the Methods, the mean current increases progressively above the topography to reach an amplitude of αU_{tide} a hundred meters above the topography, so that the generation of internal tides is unchanged (see Fig. 3.1 and Appendix for details).

The zonal wave field (deviation from the zonally averaged flow) at the critical latitude is shown in Fig. 3.5 after 5 (middle) and 19 (bottom) days of simulation. Comparing Fig. 3.2 and Fig. 3.5, a striking feature is the absence of the near-inertial horizontal waves that developed at day 19 near the seafloor in Fig. 3.2. Without a mean current, the linear wave field was largely distorted by nonlinearities, yielding strong near-inertial waves at day 19. This is not the case in Fig. 3.5 once a mean current is added, here instead the middle and bottom panels of Fig. 3.5 are similar. As before, we added the linear wave slopes, note however that the Doppler shift $\omega_0 - U_{mc}k$, and hence the wave slope, is scale dependent. For illustration purposes we picked $k = k_0$, roll-off wavenumber in the spectrum, for the yellow lines, showing reasonable but not perfect (as expected) agreement with the linear theory (top panel). Overall, the wave field remains fairly close to the linear wave field (top panel) even after 19 days. So the mean current seems to impact the nonlinear transfer of energy to secondary near-inertial waves.

We further quantify this observed reduction of nonlinear secondary wave generation by looking at energy dissipation profiles in Fig. 3.6. Each profile corresponds to a simulation where α is fixed. In the boundary layer (tens of meters from topography), the energy dissipation is not affected by the mean current (this is unsurprising since the mean current starts above topography). Above the bottom boundary layer, when α is increased, the enhanced energy dissipation associated

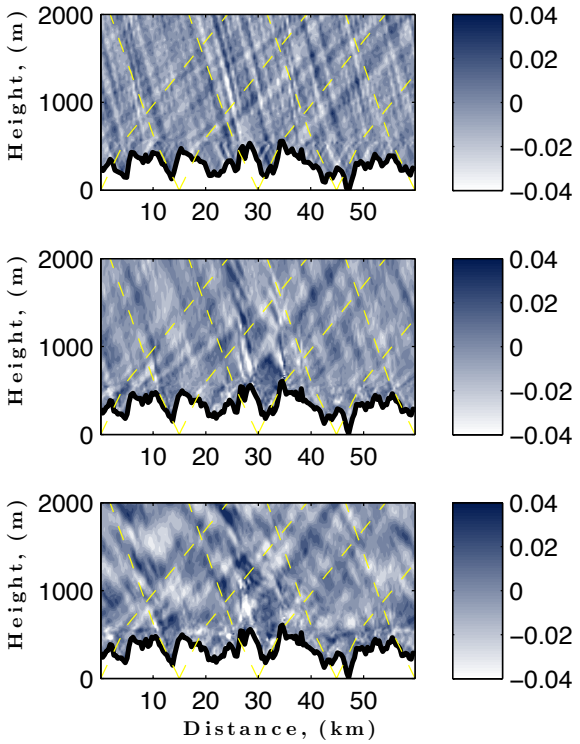

Figure 3.5: Snapshots of the wave zonal velocity (m s^{-1}) from the simulation with a mean current ($f = 0.7 \times 10^{-4}$ s^{-1}, $\alpha = 1$) after (middle) 5 days and (bottom) 19 days of simulation. The linear solution is also shown (top) for comparison, with the slopes (yellow dashed lines) from linear theory with Doppler shift (computed using a typical topographic wavenumber close to the topography spectrum wavenumber rolloff k_0).

with PSI at the critical latitude progressively disappears. Going back to the vertical profiles of dissipation Fig. 3.3, we superimpose the new profiles obtained with a mean current ($\alpha = 1$, red curves) to the previous profiles (blue curves). The new profiles at all latitudes almost perfectly match earlier profiles at non-resonant latitudes. Thus the latitude dependence of energy dissipation seems to disappear when a mean current is added.

This result is also visible on vertically-integrated energy dissipation rates (Fig. 3.4 - red curve). The energy dissipation in the boundary layer is unchanged when the mean current is added. But in the ocean interior, the enhancement of dissipation is weaker and more spread-out, for values of f between 0.6×10^{-4} s^{-1} and 0.85×10^{-4} s^{-1} (latitudes between 20° and 35°). The energy flux at the topography is shown in the middle panel in Fig. 3.4 and is quite similar to simulations without a mean current showing that the mean current does not affect the generation of waves. The local dissipation fraction (bottom panel Fig. 3.4) increases slowly from 10% at the

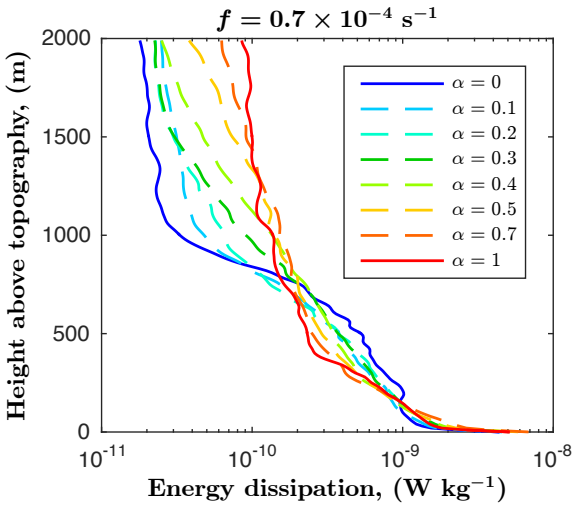

Figure 3.6: Profiles of energy dissipation rates averaged zonally and over the last 10 days of the simulations. Each profile corresponds to a simulation with a given α (which dictates the strength of the mean current) at $f = 0.7 \times 10^{-4}$ s^{-1}.

equator to ∼33% at 35° latitude and decreases at higher latitudes. Overall, with a mean current, the energy dissipation fraction is less peaked and closer to a constant northward of 25° latitude. Closer inspection of the local fraction shows that there are still two weak “resonant" latitudes shifted to ∼25° and ∼35° latitudes. In order to understand this behavior and the physical processes responsible for the new latitudinal dependence of dissipation, we analyze the kinetic energy spectrum.

3.3.3 Kinetic energy spectrum and Doppler effects

Given that the mean current is above the topography and thus does not impact the generation of waves, the picture that emerges is that the mean current impacts the propagation of the waves, and more precisely the generation of secondary waves via PSI. One possible explanation is that the growth rate of this instability for a wave packet is sensitive to the presence of a background mean velocity [Bourget et al. 2014]. Indeed, if the time scale of advection of the wave packet is faster than the growth rate of PSI, the instability may not have time to significantly distort the wave. Though this may play a role in our simulations, we believe that it is small. The waves are not spatially localized in the simulations, instead they fill the whole domain, partly due to the x-periodicity. We note however that in the ocean where localized topographic features can generate localized wave packets, this effect could play a role, in particular for the longer low-mode internal tides.

Instead here, we believe that the main reason for the behavior observed is the Doppler effect on the secondary waves.

Fig. 3.5 clearly shows the distortion of the radiating waves by the mean current. The slope of internal tides changes: upstream waves have steeper slopes and downstream waves have gentle slopes. The angle of the slant of the wave rays is changed due to Doppler effects. For a wave $\propto e^{i(kx-\omega_0 t)}$, the frequency in the frame moving with the fluid becomes $\omega_f = \omega_0 - U_{mc}k$. For internal tides, the left-propagating waves have $k < 0$ since their horizontal group velocity is negative, and the right-propagating waves have $k > 0$ (positive horizontal group velocity). This implies that the left propagating waves have a higher frequency $\omega_f = \omega_0 + U_{mc}|k|$ hence steeper slopes, while the right propagating waves have lower frequencies $\omega_f = \omega_0 - U_{mc}|k|$ hence gentler slopes. The slopes shown in Fig. 3.5 change consistently with this theoretical prediction.

This can also be seen on the kinetic energy spectrum as a function of horizontal and vertical wavenumber (Fig. 3.7). The curves from linear theory accounting for Doppler shift are shown (note that the frequency of Doppler shifted waves depends of the magnitude of the mean current but also on the horizontal wavenumber. Also note that their vertical wavenumber changes accordingly to satisfy the dispersion relation in the frame of the fluid). The agreement with the numerical simulations suggests that the Doppler effect on the primary internal tides may be important.

These changes in the primary waves imply that the secondary waves generated in the moving frame via PSI have frequencies $(\omega_0 \pm U_{mc}|k|)/2$. So the "critical latitude" at which these frequencies match the Coriolis frequency f, will now be a function of the wavenumber. This may explain the widening of the latitude window for which tidal dissipation is enhanced in Fig. 3.4 with a mean current. We note also the generation of secondary waves at f and $\omega_f - f = \omega_0 + U_{mc}|k| - f$ from the left propagating wave ($k < 0$) on Fig. 3.7. For the right propagating wave, those secondary waves are not generated since the frequency $\omega_f - f = \omega_0 - U_{mc}|k| - f$ is below f.

Fig. 3.8 illustrates schematically the Doppler effects on primary and secondary waves. Without mean current the primary wave at frequency ω_0 yields two secondary waves at frequency $\omega_0/2 = f$ at the critical latitude. With a mean current, in the frame of the fluid, the left propagating wave can generate a secondary wave via PSI at frequency $(\omega_0 + U_{mc}|k|)/2$, but the right propagating wave can not excite secondary waves at the critical latitude since the corresponding frequency $(\omega_0 - U_{mc}|k|)/2$ is below f. So Doppler effects limit transfers from the primary wave and hence reduce the energy loss via PSI at the critical latitude.

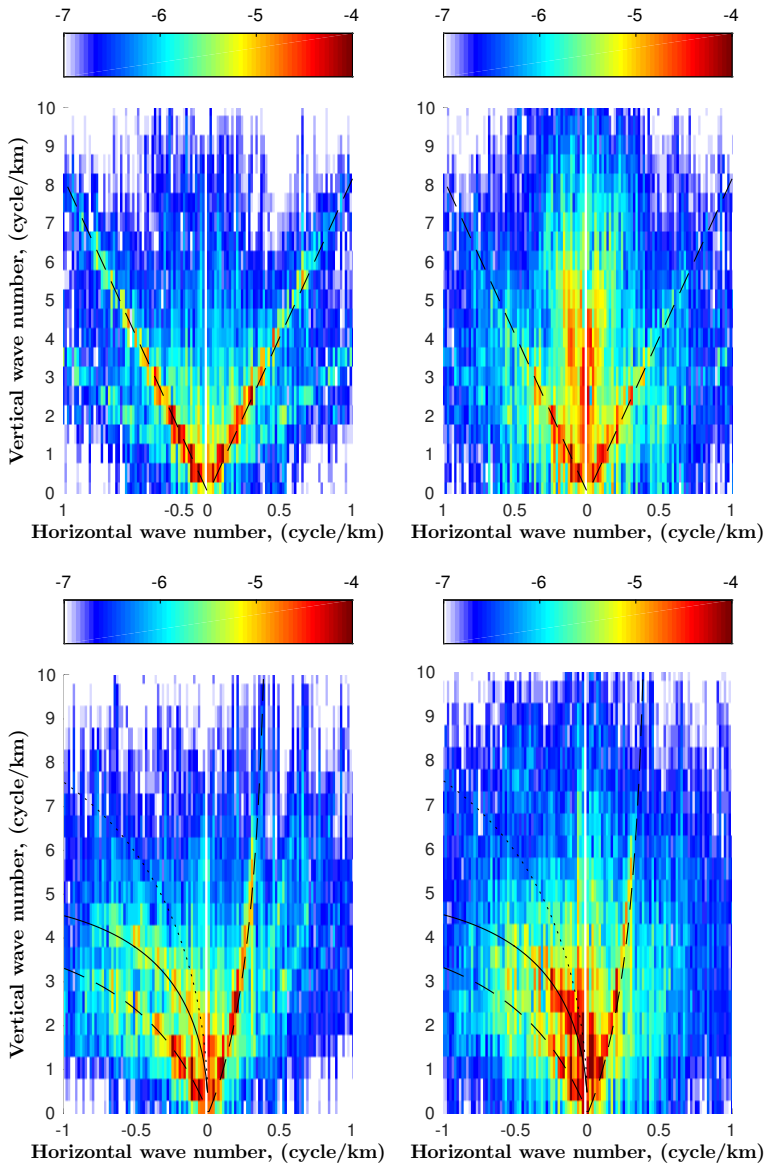

Figure 3.7: Snapshots of the horizontal and vertical wavenumber kinetic energy spectrum from (top) simulation ($f = 0.7\times10^{-4}$ s^{-1}, $\alpha = 0$) and (bottom) simulation ($f = 0.7\times10^{-4}$ s^{-1}, $\alpha = 1$) after (left) 5 days and (right) 19 days of simulation. The linear solution for the internal tide at fundamental frequency ω_0 is shown as black dashed lines (including Doppler effects with mean current bottom panels). In the bottom panels, the plain lines represent the Doppler shifted wave at $\omega_f - f$ and the dotted line the Doppler shifted wave at $\omega_f/2$.

This is also shown on Fig. 3.9 which schematically highlights the wavenumbers for which PSI can not excite secondary waves (blue regions $\Leftrightarrow (\omega_0 - U_{mc}k)/2 < f$). The top panel shows the wave frequency in the frame of the fluid as a function of horizontal wavenumber with a mean current (oblique line $\omega_f = \omega_0 - U_{mc}k$).

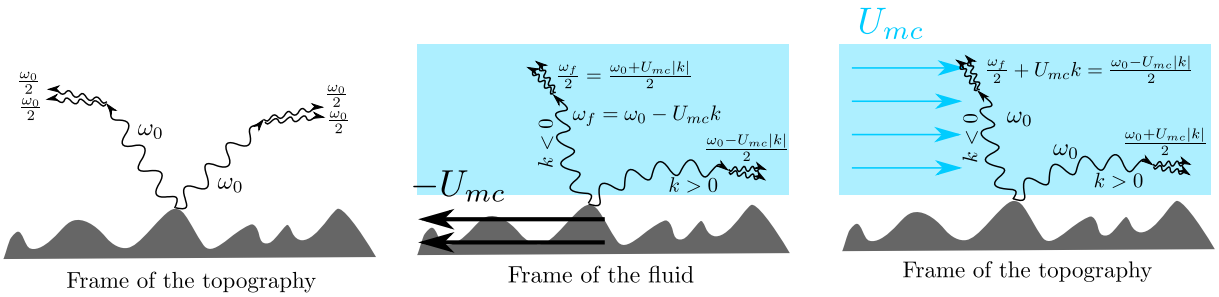

Figure 3.8: Diagrams of the Doppler effect. The left diagram represents PSI without mean current in the frame of the topography. The middle diagram represents PSI with Doppler effect in the frame of the mean current U_{mc}. The right diagram represents the frequency of the waves in the frame of topography.

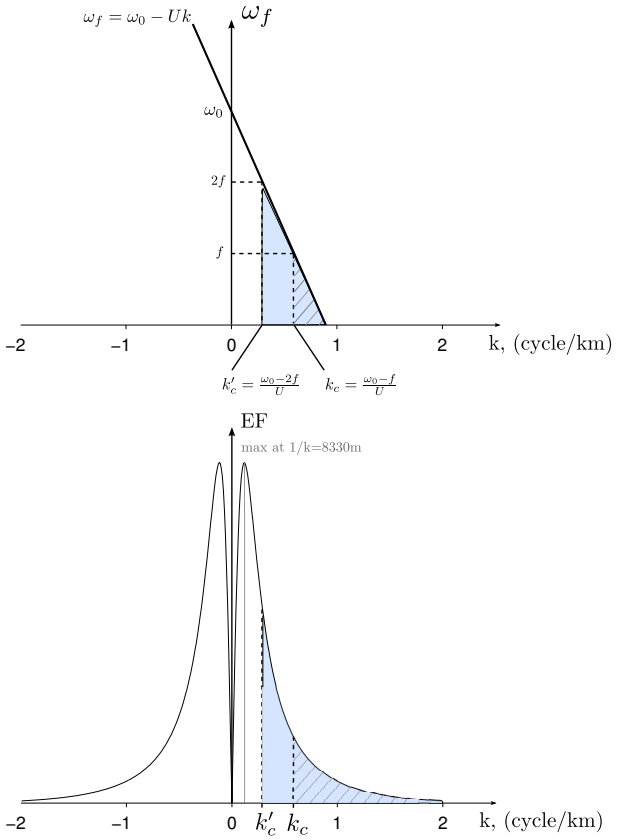

Figure 3.9: Diagram of (top) frequency of the fluid ω_f as a function of the horizontal wavenumber k in case without mean current (horizontal line $\omega_f = \omega_0$) and with mean current ($\omega_f = \omega_0 - U_{mc}k$). Diagram of (bottom) wave energy from linear theory as a function of the horizontal wavenumber k for the simulation with $f = 0.53 \times 10^{-4}$ and $\alpha = 0$. In the case of a mean current, the crosshatching section represents the domain where primary internal wave can not exist ($\omega_0 - U_{mc}k < f \Leftrightarrow k > k_c$). The blue area corresponds to the domain where PSI can not exist and where waves propagate without dissipation ($(\omega_0 - Uk)/2 < f \Leftrightarrow k > k'_c$).

The bottom diagram on Fig. 3.9 represents the energy of the waves from linear theory, for $f = 0.53 \times 10^{-4}$ s^{-1}. In the presence of a mean current, primary waves with $k > k_c$ can not exist since their frequency is below f (crosshatching area) and the energy at those horizontal wavenumbers is lost through dissipation, but these represent a small amount of wave energy. The important point is that waves with $k > k_c'$ (blue area) can not generate secondary waves via PSI and hence propagate without losing energy.

In order to illustrate this effect more clearly, we turn to a simpler monochromatic topography. Indeed, the realistic topography used here has a wide range of horizontal wavenumbers, which makes it difficult to highlight the Doppler effect. We perform new simulations with a sinusoidal topography, thus containing only one horizontal wavenumber.

3.4 Results: sinusoidal topography

The internal tides generated by sinusoidal topography $h(x) = h_0 \sin(k_t x)$ at the critical latitude are shown in Fig. 3.10 without mean current and Fig. 3.11 with mean current. The topographic height h_0 and wavenumber k_t are chosen to match the horizontal and vertical Froude numbers of the realistic topography of the previous section, so that we remain in the same flow regimes and can expect similar behavior (see Methods for detail). Two snapshots of the wave zonal velocity at 5 (middle) and 19 (right) days are shown in Figs. 3.10 and 3.11.

Without mean current, PSI yields strong inertial waves which are fully developed at day 19 (horizontal waves similar to the ones that were observed in Fig 3.2). With mean current, the strong horizontal inertial waves are absent even at day 19. The transfer of energy to smaller scales via PSI is largely suppressed, consistent with the results from the previous section. We note though that the left-propagating waves still undergo some nonlinear transfer (as in the previous section Fig. 3.7) to lower frequency waves at f and $\omega_f - f$, yielding some waves with lower frequency (smaller slopes) at day 19. But the right propagating wave is preserved even after 19 days, consistent with the theoretical prediction that Doppler effects prevent the generation of secondary waves via PSI for the right propagating wave. Indeed its frequency in the frame of the fluid is $\omega_f = \omega_0 - U_{mc} k_t$, hence $\omega_f/2$ is below f at the critical latitude.

The vertical energy dissipation profiles at different latitudes are shown in Fig. 3.12. As before, blue curves correspond to simulations without a mean current ($\alpha = 0$) and red curves correspond to simulations with a mean current ($\alpha = 1$). Without a mean current, we recover the critical latitude at $f = 0.7 \times 10^{-4}$ s^{-1}

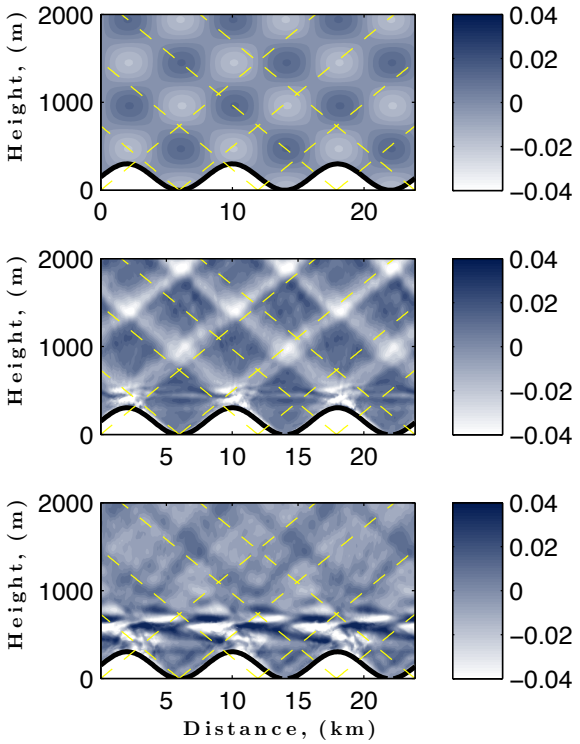

Figure 3.10: Snapshots of the wave zonal velocity (m s^{-1}) from the simulation at the critical latitude with sinusoidal topography ($f = 0.7 \times 10^{-4}$ s^{-1}, $\alpha = 0$), after (middle) 5 days and (bottom) 19 days of simulation. The linear solution is also shown (top) for comparison, as well as wave characteristics from the linear theory dispersion relation (dashed yellow lines).

where the energy dissipation is enhanced in the first kilometer above topography. When a mean current is added, consistent with our earlier results, the profiles look similar regardless of the latitude.

The vertically-integrated energy dissipation also confirms our earlier results (Fig. 3.13). As before, the energy dissipation in the bottom boundary layer does not depend on latitude, and without a mean current the dissipation in the ocean interior peaks at the critical latitude $f \approx 0.7 \times 10^{-4}$ s^{-1}. When a mean current is added, the maximum dissipation is weaker and more spread-out with latitudes. In fact, we see two new "critical" latitudes emerging, where the energy dissipation is maximum ($f = 0.55 \times 10^{-4}$ s^{-1} and $f = 0.75 \times 10^{-4}$ s^{-1}). In this simple case of monochromatic topography the interpretation of the results is clearer. Without mean current, the transfer of energy from the primary wave at ω_0 to secondary waves with frequency $\omega_0/2$ is maximum when $f = \omega_0/2$, i.e. when the frequency of the secondary waves resonates with the Coriolis frequency. With mean current, the resonance occurs at

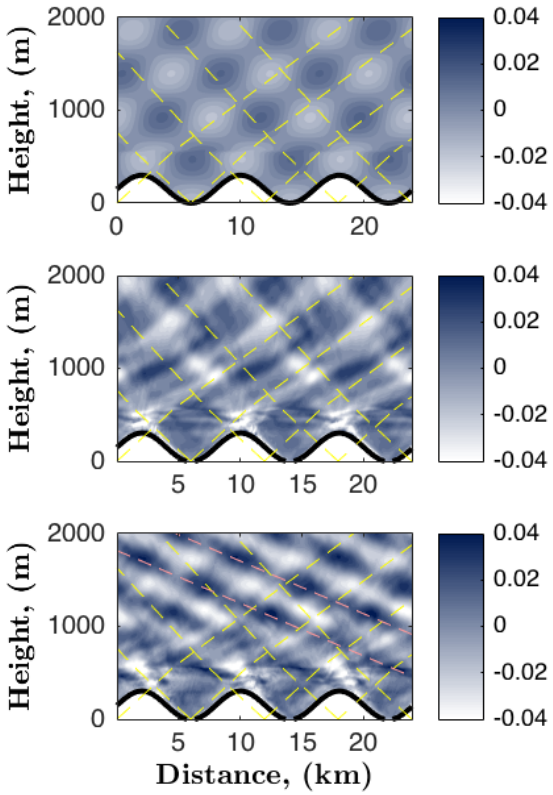

Figure 3.11: Snapshots of the wave zonal velocity (m s^{-1}) from the simulation at the critical latitude with sinusoidal topography with mean current ($f = 0.7 \times 10^{-4}$ s^{-1}, $\alpha = 1$), after (middle) 5 days and (bottom) 19 days of simulation. The Doppler-shifted linear solution is also shown (top) for comparison, with the slopes (yellow dashed lines) from linear theory with Doppler shift. The coral dashed lines show the left-propagating secondary waves at $\omega_f - f$.

two latitudes: $f = (\omega_0 - U_{mc}k_t)/2$, and $f = (\omega_0 + U_{mc}k_t)/2$. Those two "critical" latitudes hence correspond to frequencies of secondary waves with a Doppler shift.

Closer inspection shows that those two maxima are slightly asymmetric, with somewhat stronger dissipation at the higher latitude. Fig. 3.14 shows wavenumber spectra of the kinetic energy for $f = 0.53 \times 10^{-4}$ s^{-1} and $f = 0.75 \times 10^{-4}$ s^{-1}, at 5 (left) and 19 (right) days of simulation. At the beginning of the simulation, for both latitudes, spectra have energy localized at the unique topographic horizontal wavenumber k_t and its harmonics. After 19 days, there are new horizontal wavenumbers generated via non-linearities. We can see again that there is a slight asymmetry between the two resonant latitudes. There is more energy at these new horizontal wavenumbers at $f = 0.75 \times 10^{-4}$ s^{-1} suggesting that the nonlinear transfer seems to be more vigorous at this latitude (consistent with the dissipation

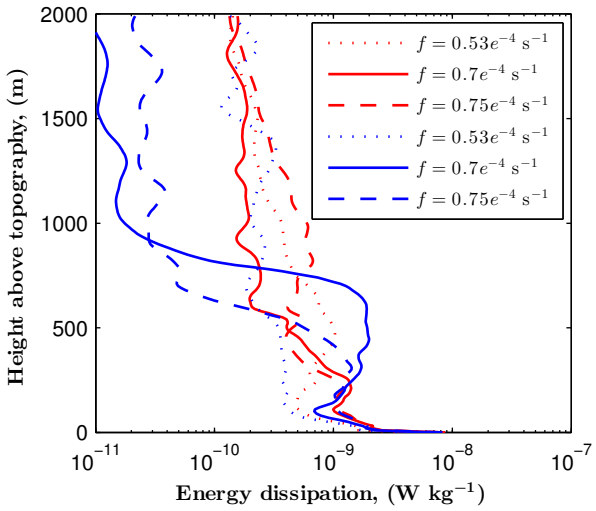

Figure 3.12: Profiles of energy dissipation rates averaged zonally and over the last 10 days from simulations with sinusoidal topography. Blue profiles correspond to simulations with $\alpha = 0$ and red profiles to simulations with $\alpha = 1$. The enhanced dissipation at the critical latitude without mean current disappears when a current is added, consistent with the earlier results for realistic topography.

in Fig. 3.13). We interpret this asymmetry as resulting from the slower group velocities of the waves at $f = 0.75 \times 10^{-4}$ s^{-1}, allowing non linearities to develop and to transfer a larger amount of energy to smaller scales.

3.5 Conclusions and discussion

In this paper, we investigate the latitudinal dependence of the local dissipation of internal tides, near their generation site at the seafloor. We recover earlier results that were obtained in the idealized case of internal tides propagating in a quiescent ocean. In that case, without a mean current, the local dissipation of internal tides generated at rough topography is strongly enhanced at a critical latitude. The latter is the latitude where inertial waves at f resonate with the secondary waves generated by PSI at $\omega_0/2$. When a mean current is added, though weak (same order as the barotropic tide: a few cm s^{-1}), this behavior drastically changes. The dissipation peak at the critical latitude disappears and the local dissipation fraction of internal tides is closer to a constant, with two weak peaks at about 25° and 35° latitude.

Despite its simplicity, the idealized case of sinusoidal topography reproduces the main features of the internal tides generated by realistic multichromatic topography. This helps shed some light into the processes determining the latitudinal distribution

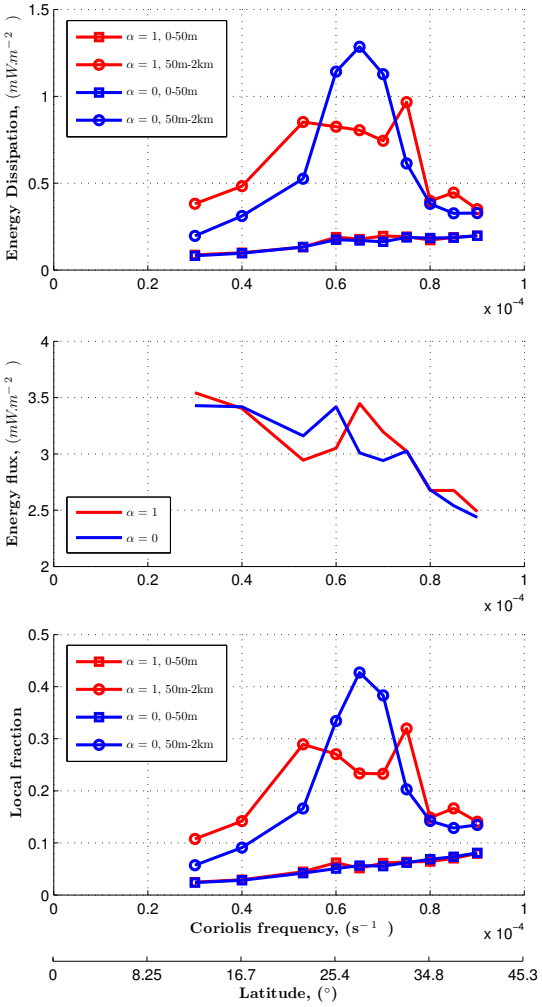

Figure 3.13: Energy dissipation rate integrated in the bottom 50 m (square) and between 50 and 2 km (circle) with sinusoidal topography. Blue curves correspond to simulations with no U_{mc} and red curves to simulations with U_{mc} and $\alpha = 1$. We recover the results of the previous section with realistic topography, namely the dissipation enhancement at the critical latitude disappears when a mean current is added, and the dissipation is closer to a constant, with two new weaker peaks at Doppler shifted latitudes.

of wave instability and dissipation. This sensitivity to a mean current can be understood by accounting for the Doppler shift of the primary internal tides as they propagate through the mean current. Different scales of the waves are shifted with different magnitudes, yielding a wide range of critical latitudes for the shifted primary frequency. In other words, the peak of dissipation at the critical latitude is not robust to the presence of a mean current.

This suggests that under realistic conditions, where waves are unlikely to propagate through a quiescent ocean, the local dissipation of the internal tide is not a strong function of latitude. The reduced dissipation fraction near the critical

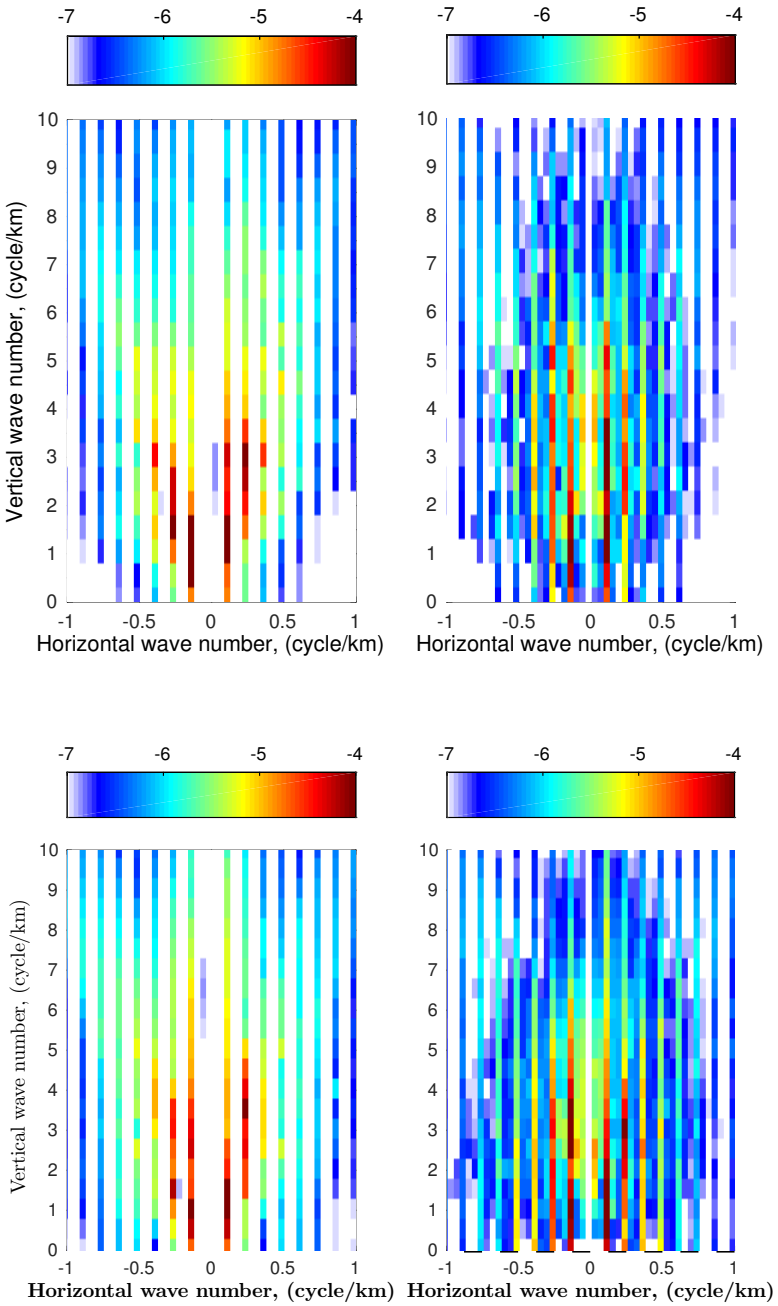

Figure 3.14: Snapshots of the horizontal and vertical wavenumber spectrum from (top) simulation ($f = 0.53 \times 10^{-4}$ s^{-1}, $\alpha = 1$) and (bottom) simulation ($f = 0.75 \times 10^{-4}$ s^{-1}, $\alpha = 1$) after (left) 5 days and (right) 19 days of simulation with sinusoidal topography.

latitude implies that more wave energy than previously thought may propagate away from topography, and hence may be available to dissipate in remote locations. A recent observational study also highlights the impact of Doppler effects on the propagation of near-inertial waves, which can propagate poleward beyond their critical latitude [Xie et al. 2016].

This has implications for the transformation of deep water masses and the abyssal circulation. Recent estimates of internal waves' impact on the overturning circulation point out the large uncertainty associated with remote dissipation of tides which do not dissipate locally near their generation site. Depending on where this dissipation and the concomitant mixing occur, in particular its vertical structure, such mixing could drive 1 to 28 Sv of AABW upwelling. More work is desirable to help better constrain estimates of remote internal tide energy propagation and dissipation.

Acknowledgments

The authors would like to thank Maxim Nikurashin for providing further details about the setting of the MITgcm simulations of Nikurashin and Legg [2011]. C.M. gratefully acknowledges financial support from the Chair for sustainable development at Ecole Polytechnique. We acknowledge CINES/GENCI, France, for providing access and support to their computing platform JADE, as well as the PRACE Research Infrastructure computing resource Curie based in France at TGCC. The authors would like to thank the Direction Générale de l'Armement (DGA) for the financial support of Océane Richet's PhD research.

4

Influence of upstream perturbations on upstream circulation of a hydraulically controlled sill

Long waves, with larger scales than waves studied in the two previous chapters, can also modify currents. In this last study, we investigate the effect of a hydraulically controlled sill on the upstream circulation submitted to an inflow perturbation in the upstream basin. In this configuration, the sill is the only location for the upstream and downstream basin to communicate and to exchange water.

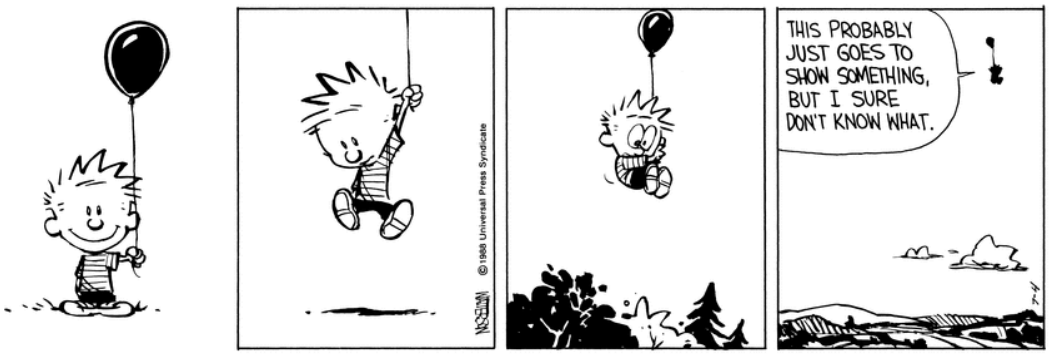

Bill Watterson, 4 July 1988

4.1 Introduction

The Atlantic Ocean is separated from the Nordic and Arctic Seas by the Greenland-Iceland-Scotland Ridge (GISR, Fig. 4.1). The surface waters from the Atlantic flow into the Nordic Seas where they lose buoyancy and form a dense water mass through deep convection and other processes [Hattermann et al. 2016]. The dense water spills over the shallow sills in the various channels that cut through the GISR, and mix with lighter water masses downstream to form North Atlantic Deep Water (NADW), which feeds the lower limb of the Atlantic Meridional Overturning Circulation (AMOC) [Dickson and Brown 1994][Hansen and Østerhus 2007]. The overflow volume of dense water, Denmark Strait Overflow Water (DSOW, potential density σ_θ larger than 27.8 kg.m^{-3} [Dickson and Brown 1994]) over the GISR is equal to 6 Sv (1 Sv = 10^6 m^3.s^{-1}) and distributed between the Denmark Strait (sill depth 620 m, 3 Sv), the Faroe Bank Channel (sill depth 840 m, 2 Sv) and the Iceland Faroe Ridge (sill depth 420 m,1 Sv) [Hansen et al. 2008].

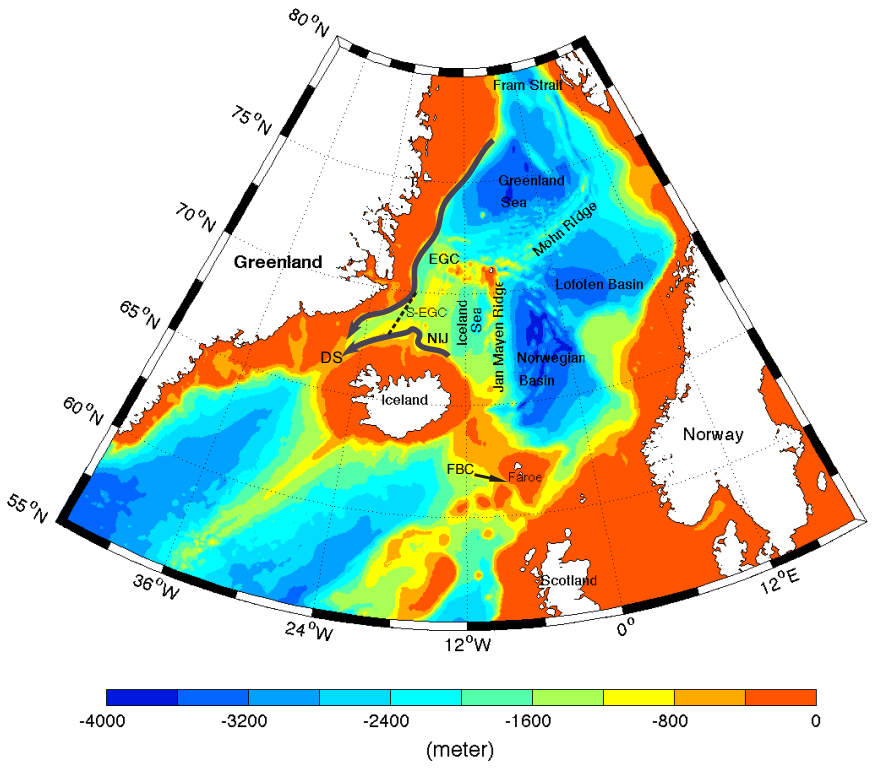

Figure 4.1: Bathymetry of the Nordic Seas from [Yang and Pratt 2014]. Abbreviations correspond to, **DS**: Denmark Strait, **EGC**: East Greenland Current, **NIJ**: North Icelandic Jet, **s-EGC**: separated EGC and **FBC**: Faroe Bank Channel.

From the Nordic Seas side of the ridge, three currents approach the Denmark Strait: the East Greenland Current (EGC), which follows the East Greenland coastline and is the main conduit for Arctic-origin fresh water flowing into the subpolar gyre on the East side of Greenland [Mauritzen 1996]; the North Icelandic Jet (NIJ), which approaches Denmark Strait along the Iceland shelf break [Våge et al. 2013] [Harden et al. 2016]; and the separated-EGC (sEGC), which branches off the EGC upstream of Denmark Strait and joins the NIJ close to the Denmark Strait [Våge et al. 2013] [Harden et al. 2016]. The Denmark Strait Overflow Water (DSOW) is composed by these three currents. Its volume transport varies on short timescales of a few days [Mastropole et al. 2016] [Von Appen et al. 2016] but does not display seasonal variability or a long-term trend [Dickson and Brown 1994] [Jónsson 1999] [Jochumsen et al. 2012].

The overflow in the Denmark Strait is hydraulically controlled [Whitehead et al. 1974] [Nikolopoulos et al. 2003] [Girton et al. 2006], which means that the flow upstream of the sill is dominated by its kinetic energy (river regime) and downstream of the sill by its potential energy (torrential regime). The DSOW can be seen as a marine waterfall. The particularity of a hydraulically controlled sill is that a perturbation in the supply of dense water in the upstream (for example Nordic Seas) basin will communicate via a long ocean waves reflected at the sill and modify the transport of the overflow water (here DSOW) [Pratt and Whitehead 2008].

We propose to study the effect of long waves (Kelvin and topographic Rossby waves) on a hydraulically controlled overflow in a 1.5-layer reduced gravity model. The purpose of this study is to understand the upstream influence of a hydraulically controlling sill in a case where a peninsula or an island geometry complicates the path taken by an upstream disturbance. The model set up is described in section 2, followed by the description of a simulation with a dam break. In section 3, we present simulation results from a case with a dam break and an inflow/outflow as initial conditions and the impact of a perturbation in the inflow and its response.

4.2 Methods

The numerical model is a 1.5 layer reduced gravity model. It is assumed that the overlying fluid layer is very thick compared to the bottom layer and motionless. The horizontal velocity (u, v) and the layer thickness H of the thin, dynamically

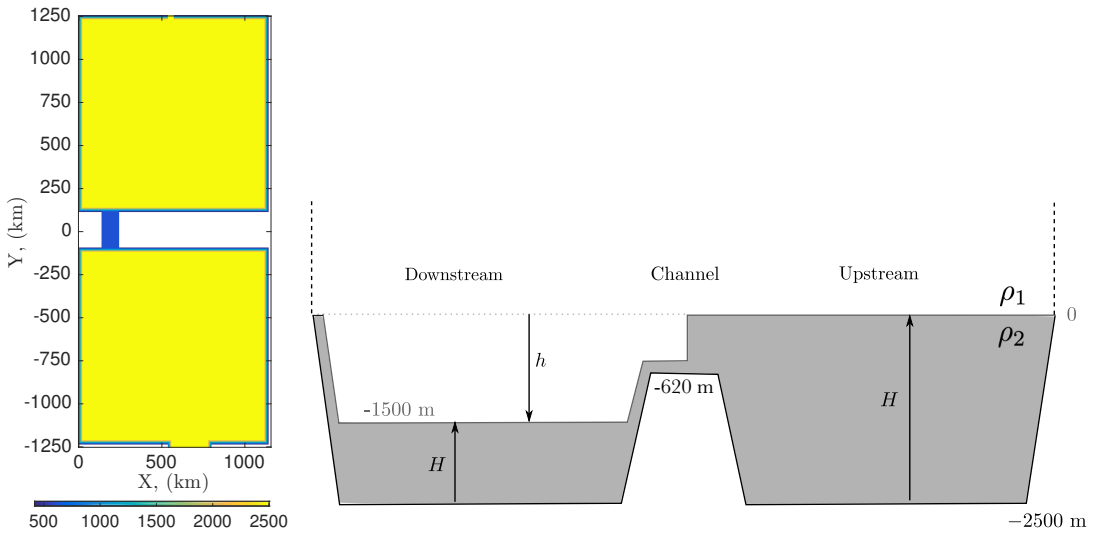

Figure 4.2: (a) Bathymetry of the domain and (b) sketch of the lateral view of the domain at the initial state.

active bottom layer are governed by the shallow water equations:

$$\partial_t u + \mathbf{u} \cdot \nabla u - fv = -g' \partial_x H + \nu \nabla^2 u, \tag{4.1}$$

$$\partial_t v + \mathbf{u} \cdot \nabla v + fu = -g' \partial_y H + \nu \nabla^2 v, \tag{4.2}$$

$$\partial_t H + \nabla(\mathbf{u} H) = 0, \tag{4.3}$$

where f is the Coriolis frequency, $g' = g\Delta\rho/\rho_0$ is the reduced gravity, $\nu = 5 \times 10^{-4}$ $\mathrm{m^2 s^{-1}}$ is the horizontal viscosity and ∇^2 the horizontal Laplacian. The control simulation latitude is 66°N. At the initial state, the fluid in the bottom layer is at rest and the interface is flat. In the initial layer thickness is equal to $H_0(x, y)$, which is larger in the upstream basin and varies according to the bathymetry. In view of the presence of $\nabla^2 \mathbf{u}$, we need to specify a lateral boundary condition (no stress, free slip and no-normal flow). In the absence of sources and sinks, a steady state is reached, and a perturbation corresponding to an inflow/outflow through a lateral opening boundary is added. The horizontal resolution is the same in the $x-$ (zonal) and $y-$ (meridional) directions and equals to 5 km. The discretization of the model is based on the Arakawa C-grid and the model domain spans 1155 km zonally and 2505 km meridionally.

Figure 4.2 shows the bathymetry and the initial state of the model. The upstream and downstream basins have a flat bottom, except along the boundaries where there

is a slope. The depth of the Denmark Strait is equal to 620 m and the depth of the Iceland-Scotland Ridge is a bit shallower with a depth of 520 m. The initial state corresponds to a situation where the lower layer depth is more than twice large as in the upstream basin, and separated from the downstream basin by virtual dams in the middle of the Denmark Strait and the Iceland-Scotland Ridge. The maximum thickness in the upstream basin is equal to 2500 m and 1000 m in the downstream basin. The interface is set to zero in the upstream basin. The model allows grounding but still maintains a thin (20 cm) sheet of lower-layer fluid throughout.

4.3 Preliminary numerical results: dam break

We first consider the case of simulations with only a dam break in a channel. What we call a "dam break" is an initialization with a step in the interface depth between the upstream and the downstream basin, in the middle of the channel. The upstream basin has a maximum lower layer thickness of 2500 meters and the downstream basin of 1000 meters. The reference simulation has a latitude of 66°, a $\Delta\rho = \rho_2 - \rho_1 = 0.3$ kg m^{-3}, a sill depth equal to 1880 m and a slope of 0.0833.

4.3.1 Circulation in the basins

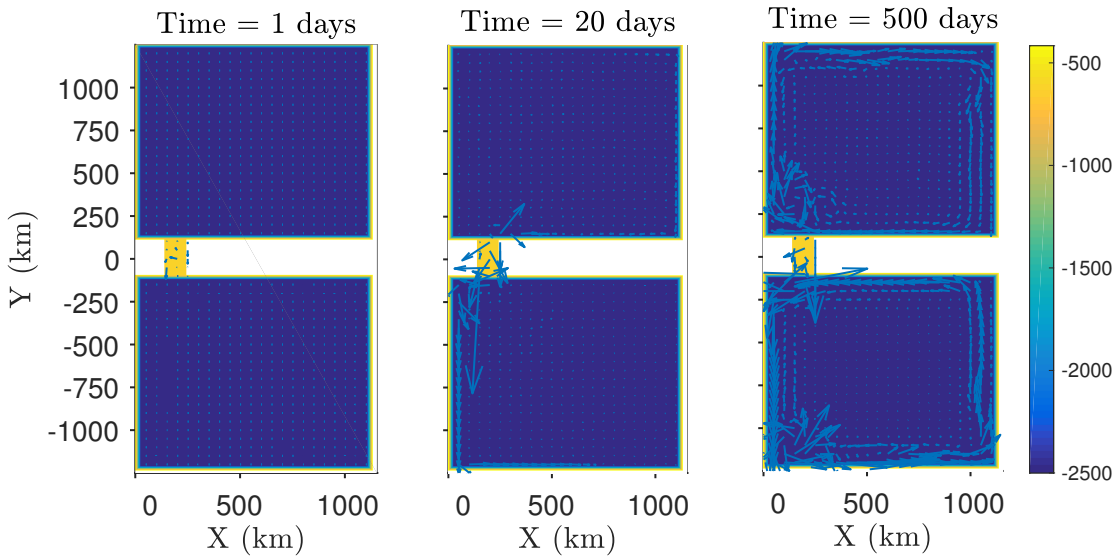

Figure 4.3: Snapshot of velocity field (arrows) at different times after the dam breaks. Colors represent the bathymetry.

A snapshot of the circulation induced by the dam break is shown in Fig. 4.3 (blue arrows) at 1 day, 20 days and 500 days. The dam break generates a current

from the channel which propagates along the eastern boundary in the upstream basin and the western boundary in the downstream basin. The generated circulation in the upstream basin is thus anti-cyclonic, while in the downstream basin the circulation is cyclonic. The flow in both basins is maximum over the slope.

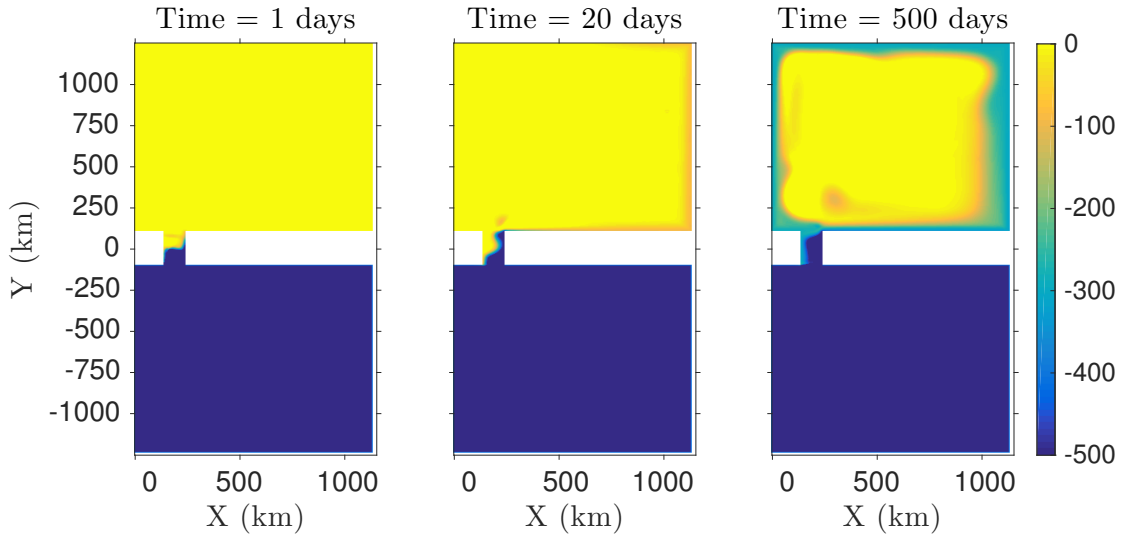

Figure 4.4: Snapshot of the layer thickness anomaly (variations around the zero line on figure 4.2b, in meters) at different times after the dam breaks. The color-scale has been saturated to highlight the propagation of the wave in the upstream basin.

Fig. 4.4 shows the layer thickness anomaly (variations around the zero line on figure 4.2b) for 3 snapshots in the simulation. The dam break generates a wave in the channel which propagates in the cyclonic direction in both basins. The wave shows up as a decrease in the layer thickness along the upstream boundary and an increase along the downstream boundary (not shown on the figure due to the saturated colorbar used to highlight the decreased layer thickness). 500 days after the dam break, the surplus of dense water in the channel has flown into the downstream basin and the effect of the rotation constrains the lower-layer flow to the western flank of the channel (Fig. 4.4c).

4.3.2 Hydraulic control in the channel and transport

One way to know if the flow in a channel is hydraulically controlled is to calculate the generalized Froude number (Stern's criterion [Stern 1974])

$$Fr = \frac{\int_{w/2}^{-w/2} \frac{1}{g'H^2} dx}{\int_{w/2}^{-w/2} \frac{1}{Hv^2} dx}, \tag{4.4}$$

where w is the width where the flow is unidirectional, g' the reduced gravity, H the layer thickness and v the velocity in the channel. If $Fr < 1$ the flow is subcritical upstream of the sill and the kinetic energy is smaller, and if $Fr > 1$, the flow is supercritical downstream of the sill and the kinetic is larger.

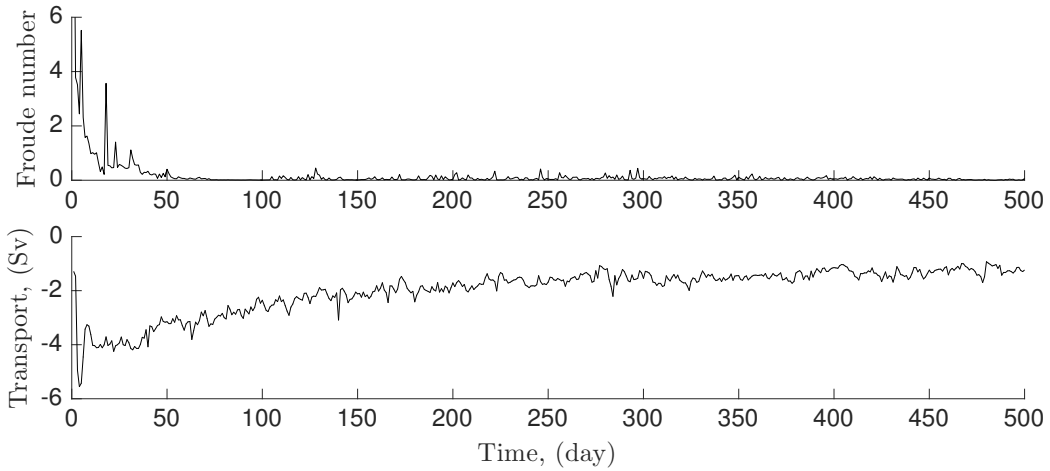

Figure 4.5: Time series of (a) the maximum generalized Froude number in the channel and (b) transport. The generalized Froude number achieves 12 at the begin.

Figure 4.5a shows the time series of the generalized Froude number. We can notice that the maximum Froude number in steady state is less than 1 meaning that the flow in the channel is subcritical. The generalized Froude number may not be applicable here, because in our simulations, once the flow achieves a steady state, it is separated (grounded interface - see figure 4.4) and it is unsure that the Stern's criterion is still valid. Nevertheless, the maximum local Froude number is greater than 1 (not shown) in the channel, a necessary condition for supercritical channel flow. Moreover, with the configuration of the simulations with a layer depth lower than the sill in the downstream basin, we can thus conclude with some confidence that the flow in the channel is hydraulically controlled, though further investigation is desired to determine this with certainty. The associated transport is shown on figure 4.5b. During the first days, the transport from the upstream channel toward the downstream channel is very strong but quickly decreases, and then increases slowly. After 300 days, the transport reaches a constant value around 2 Sv meaning that the simulation achieves its steady state.

4.3.3 Waves induced by the dam break

We saw previously in figure 4.4 that the dam break generates a cyclonic wave propagating on the slope and associated with a decrease in the layer thickness.

Figure 4.6 shows the phase speed of the observed wave for different simulations with a given latitude and $\Delta\rho$. We add the theoretical phase speed of the topographic Rossby wave ($c = R_{bc}^2 \times \beta_{topog}$, where $R_{bc} = g'H/f^2$ is the baroclinic Rossby radius of deformation and β_{topog} is the topographic beta) and the Kelvin waves ($c = \sqrt{g'H}$ - $H = 833$ m is the layer thickness for which the phase speed has been calculated in the simulation) for comparison. Though there is some uncertainty in figure 4.6, the phase speed of the waves in the simulations are consistent with that of Kelvin waves.

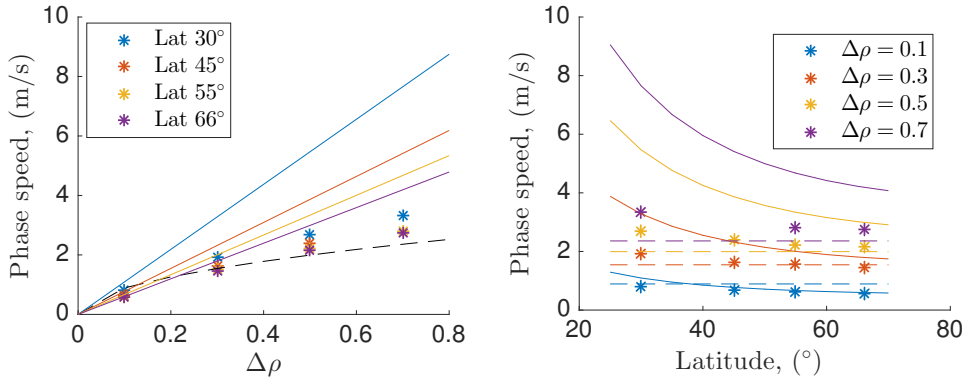

Figure 4.6: Wave phase speed for different simulation ($*$) as a function of (a) $\Delta\rho$ and (b) latitude. Solid lines correspond to the theoretical phase speed of the topographic Rossby wave and dashed lines to the theoretical phase speed of the Kelvin wave in the layer thickness equal to 833 m. Colors are given in the legend.

4.3.4 Influence of parameters ($\Delta\rho$, latitude, sill depth and slope) on Froude number and transport

We evaluate the generalized Froude number for different simulations varying the latitude, $\Delta\rho$, sill depth and the slope in the basins (Fig. 4.7). The Froude number number generally decreases with latitude, and increases with $\Delta\rho$ and with sill depth (Fig. 4.7 left and middle). The evolution of the Froude number with sill depth (low sill depth equals to high layer thickness) is easily understandable ($Fr \sim v^2/(g'H)$). For the evolution with $\Delta\rho$ and the latitude, we link the increase of the Froude number with the geostrophic velocity $v = g'\partial_x H/f$. In fact, when f increases, v decreases and thus the Froude number decreases. The same applies for $\Delta\rho$ which appears in g', v increases with $\Delta\rho$ and so the Froude number increases. The last parameter is the slope of the basins and in this case, the Froude number seems to increase with the slope which is in good agreement with the geostrophic flow.

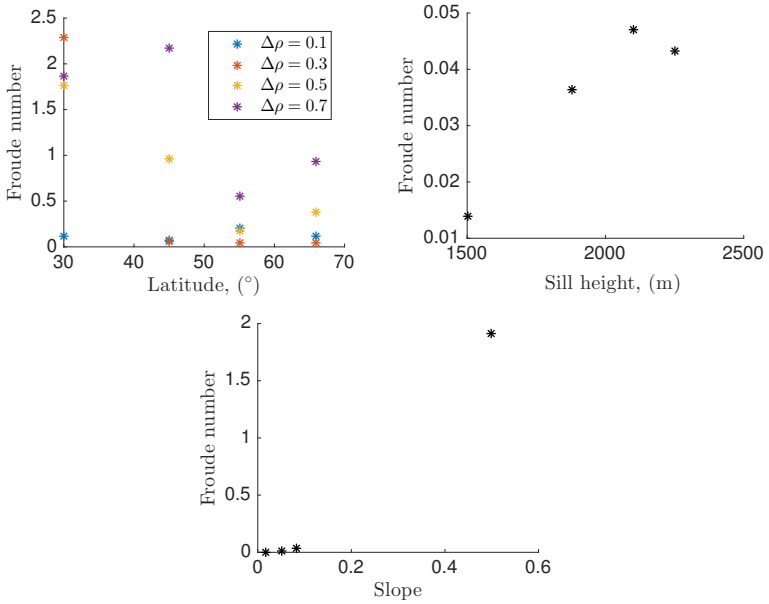

Figure 4.7: Maximum generalized Froude number (Stern's criterion) in the channel, averaged over the last 100 days of simulation as a function of (a) latitude and $\Delta\rho$, (b) sill depth and (c) slope of the basins.

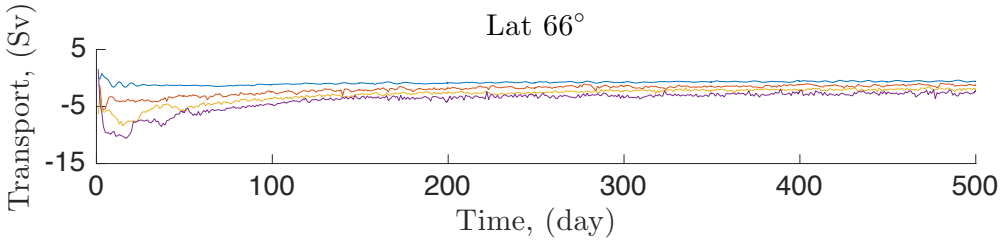

Figure 4.8: Time series of transport at the entrance of the channel averaged over the last 100 days at 66°N. Colors correspond to various values of $\Delta\rho$: blue - $\Delta\rho = 0.1$, orange - $\Delta\rho = 0.3$, yellow - $\Delta\rho = 0.5$ and purple - $\Delta\rho = 0.7$.

Figure 4.8 shows time series of the transport through the channel at 66°N for different $\Delta\rho$. All the simulations reach a steady state after around 200 days. The transport increases with $\Delta\rho$ and with the slope and decreases with latitude (Fig. 4.9a and c) which is again in good agreement with the geostrophic velocity. The transport decreases with sill depth (Fig. 4.9b) which implies a thinner layer thickness and so a weaker transport.

4.4 Dam break simulation with a northern inflow

In this section, we look at the flow dynamics in simulations initialized with a dam break in the middle of the channel and a constant inflow of 1.5 Sv through a channel in the northern boundary of the upstream basin. We run simulations during 500 days.

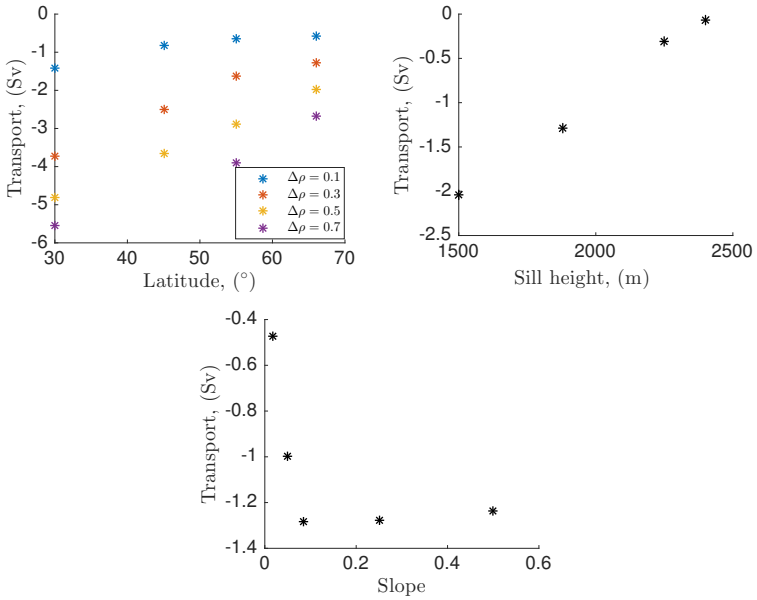

Figure 4.9: Transport in the channel averaged over the last 100 days of simulation as a function of (a) latitude and $\Delta\rho$, (b) sill depth and (c) slope of the basins.

4.4.1 Circulation in the upstream basin

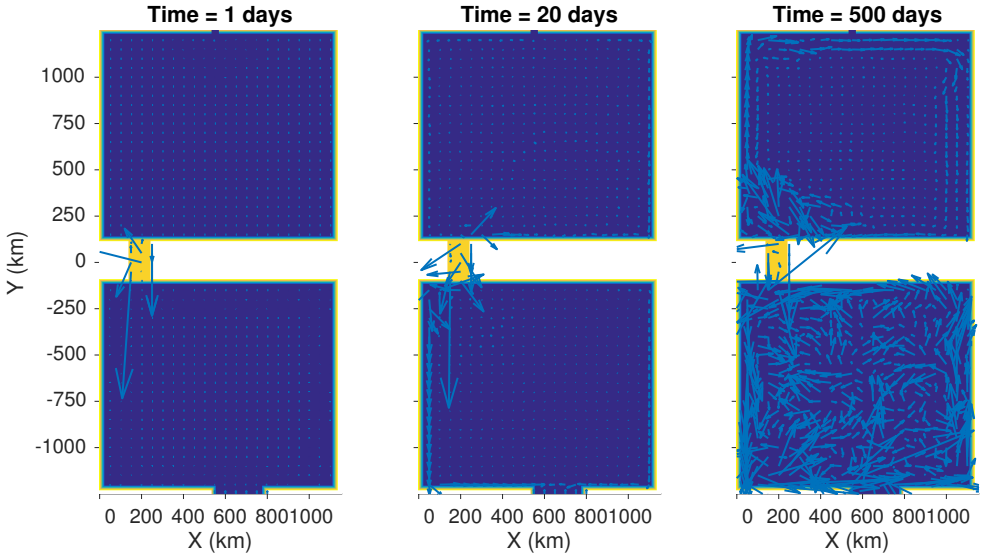

Figure 4.10: Snapshots of velocity field (arrows) at different times after the dam breaks. Colors represent the bathymetry. The latitude is 66°, $\Delta\rho = 0.3$ kg m^{-3}, the sill depth is 1880 m and the slope is 0.0833.

Figure 4.10 shows snapshots of the velocity field at day 1, 20 and 500. The circulation in the upstream basin is anti-cyclonic and cyclonic in the downstream basin. The dam break generates waves that propagate with the coast on their

right-hand side in both basins. The inflow is directed southward through the channel. The outflow channel prevents propagation of the signal from the channel around the downstream basin and back into the upstream basin.

The anti-cyclonic circulation in the upstream basin follows from the potential vorticity budget. Following [Pratt and Llewellyn Smith 1997], [Yang and Price 2000] and [Yang and Price 2007], and considering $w = w(z)$, $f = f_0 + \beta y$ and after derivation of the model equations ($\zeta = \partial_x(4.2) - \partial_y(4.1)$)

$$\mathrm{d}_t(\zeta) + (\zeta + f)\nabla.\underline{u} + \beta v = \nabla \times (\nu \nabla^4 \underline{u}), \tag{4.5}$$

where ζ is the relative vorticity and d is the Lagrangian derivative. Considering $\mathrm{d}_t = \beta v$

$$\mathrm{d}_t(\zeta + f) + (\zeta + f)\nabla.\underline{u} = \nabla \times (\nu \nabla^4 \underline{u}). \tag{4.6}$$

Using the continuity equation and multiplying by $1/H$

$$\mathrm{d}_t \left(\frac{\zeta + f}{H} \right) + \frac{(\zeta + f)}{H} \partial_z w = \frac{1}{H} \nabla \times (\nu \nabla^4 \underline{u}). \tag{4.7}$$

Now in steady state and considering only the vertical component

$$\underline{u}.\nabla \left(\frac{\zeta + f}{H} \right) - \left(\frac{\zeta + f}{H} \right) \partial_z w = \frac{1}{H} \nabla \times (\nu \nabla^4 \underline{u}), \tag{4.8}$$

where the first term is the vorticity advection, the second term is vortex stretching and last term is the friction. $q = \frac{\zeta + f}{H}$ is the potential vorticity. In that case, the vertical component in the potential vorticity budget is small compare to the relative vorticity ζ

$$\nabla. \left(U_h \left(\frac{\zeta + f}{H} \right) \right) = \nabla \times (\nu \nabla^4 \underline{u}). \tag{4.9}$$

After integration over the whole domain and using the Stokes theorem

$$\oint_C (\underline{U}_h.\widehat{n}) \left(\frac{\zeta + f}{H} \right) \mathrm{d}S = \int \int_A D_p \mathrm{d}x\mathrm{d}y, \tag{4.10}$$

where $\underline{U}_h = H(u, v)$ and D_p is the curl of the friction. The left hand side in the equation corresponds to the lateral potential vorticity advection and the right hand side to the frictional torque. Considering that the relative vorticity ζ is smaller than the planetary vorticity f, the deviation of the layer thickness from the initial value is small, and the friction is approximated as a Rayleigh friction

$$\sum_{i=1}^{N} \frac{Q_i f_i}{H_{0i}} \approx -\lambda \oint_C (\underline{u}.\underline{l}) dS, \tag{4.11}$$

where u is the tangential velocity along the boundary, Q_i is the volume transport out of the basin across the sill, λ the Rayleigh friction coefficient and l the unit tangential vector.

In our simulations, the inflow channel in the upstream basin is deeper than the channel between the two basins, which induces a positive potential vorticity anomaly and thus an anti-cyclonic circulation.

4.4.2 Froude number: hydraulically controlled?

The maximum Froude number based on Stern's criterion (Eq. 4.4) and averaged over the last 100 days of simulation varies around a value of 1 in the simulations (Fig. 4.11). We can not conclude based on this criterion alone whether the channel flow is hydraulically controlled or not, as the applicability of this criterion in our case is unclear as mentioned earlier. This is due to the presence of a separated flow but in view of the domain configuration and the value of the maximum local Froude number, we are hydraulically controlled. Maximum generalized Froude number increases with $\Delta\rho$ and decreases with latitude (Fig. 4.11a). It increases with sill depth and with slope. An increase of the Froude number with sill depth (low sill depth equals to high layer thickness) is coherent ($Fr \sim v^2/(g'H)$, where v is the meridional velocity, g' the gravity reduced and H the layer thickness). Now if the geostrophic velocity v decreases with latitude, so does the Froude number. The same reasoning applies to $\Delta\rho$ and the slope, but in that case v increases with larger density difference or with the slope.

4.4.3 Transport through the channel

The transport in the channel is calculated at the entrance. We can see on figure 4.12 that the steady state in the simulations is achieved in 200 days and the transport is greater than without the inflow case (dashed curve). The transport is directed from the upstream basin toward the downstream basin (negative transport associated with negative meridional velocity - by convention, meridional velocity is positive northward) and it increases with $\Delta\rho$. In fact, the geostrophic velocity, $v \sim g'/f\partial_x H$ increases with $\Delta\rho$.

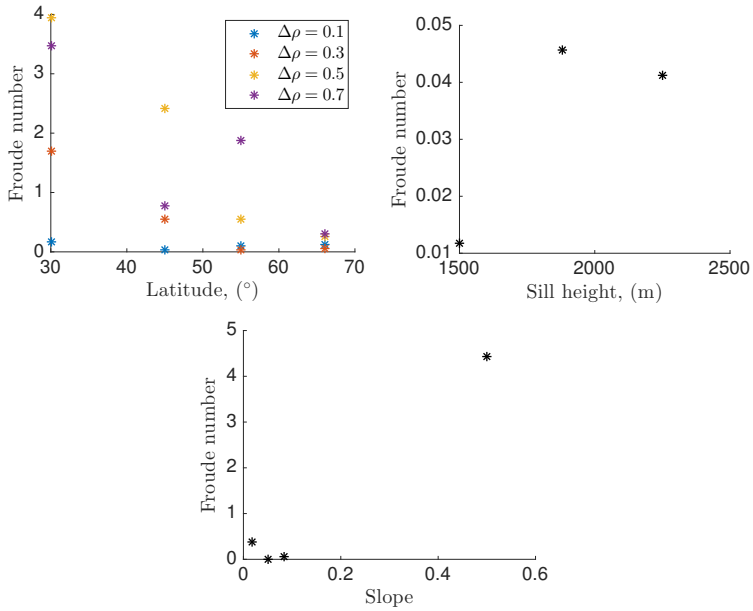

Figure 4.11: Maximum generalized Froude number (Stern's criterion) in the channel, averaged over the last 100 days of simulation as a function of (a) latitude and $\Delta\rho$, (b) sill depth and (c) slope of the basins.

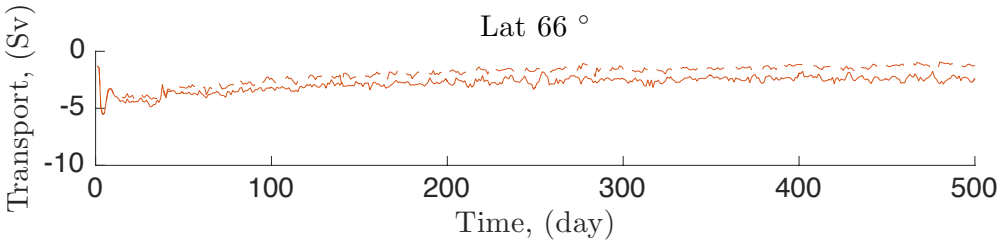

Figure 4.12: Time series of transport at the entrance of the channel averaged over the last 100 days at 66°N with $\Delta\rho = 0.3$. Dashed curve corresponds to the case without an inflow and plain curve to the case with an inflow.

As seen previously, the transport increases with $\Delta\rho$ (Fig. 4.13a). It also decreases with latitude due to a decrease in the velocity v (geostrophic flow). The transport increases with sill depth or more exactly decreases with layer thickness (Fig. 4.13b). Furthermore, the transport decreases with the slope (Fig. 4.13c).

After almost 200 days, the transport seems to be constant but the magnitude can be greater than the inflow transport showing that the flow has not reached an equilibrium.

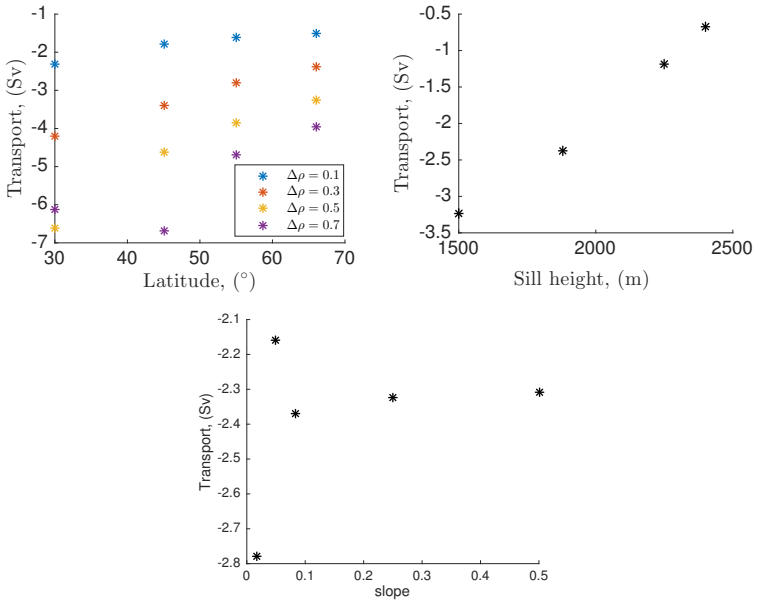

Figure 4.13: Transport in the channel averaged over the last 100 days of simulation as a function of (a) latitude and $\Delta\rho$, (b) sill depth and (c) slope of the basins.

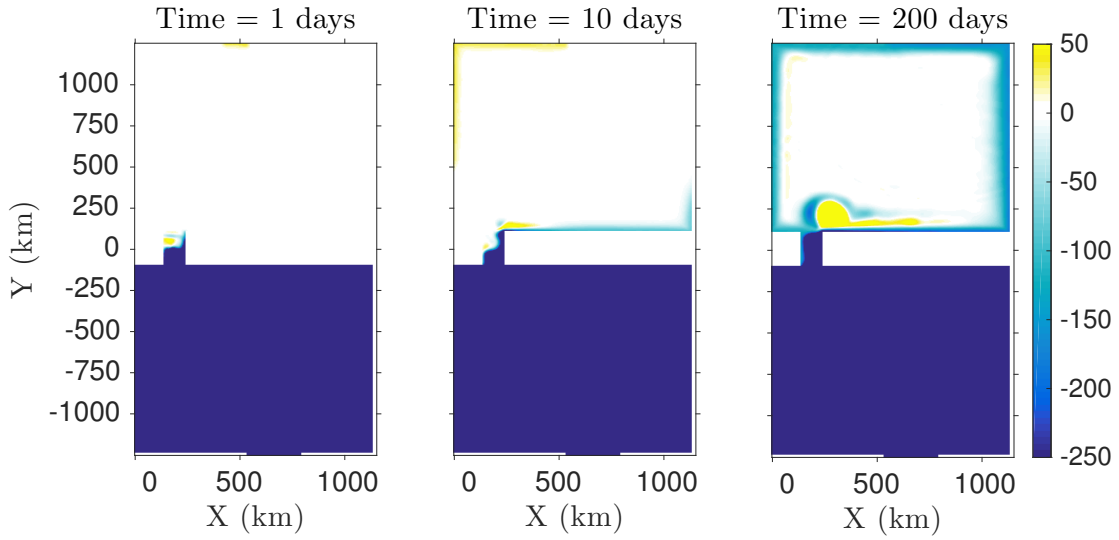

Figure 4.14: Snapshots of the layer thickness anomaly (variations around the zero line on figure 4.2b, in meters) at different times after the dam breaks. The latitude is 66°, $\Delta\rho = 0.3$ kg m^{-3}, the sill depth is 1880 m and the slope is 0.0833. The color-scale has been saturated to highlight the propagation of the wave in the upstream basin.

4.4.4 Waves induced by the inflow and the dam break

Snapshots of the layer thickness anomaly (Fig. 4.14) show two propagative waves in the upstream basin: one induced by the inflow and characterized by a positive anomaly (yellow) and a second one induced by the dam break and characterized

by a negative anomaly (cyan). Both are cyclonic waves and propagate along the boundaries.

We track these waves to obtain their phase velocity and thus to identify them. The figure 4.15 shows the phase speed of the dam break and the inflow waves in different simulation (∗) and also the theoretical phase speed of the topographic Rossby wave (solid lines) for diverse latitudes (colors) and of the Kelvin wave (black dashed lines) for a layer thickness equals to 833 m.

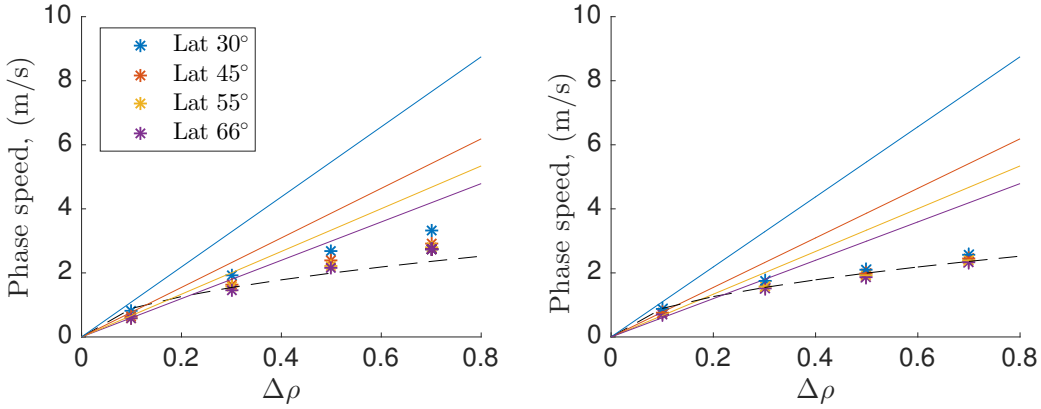

Figure 4.15: Wave phase speed for different simulation (∗) as a function of $\Delta\rho$ for (a) the dam break wave and (b) the inflow wave. Solid lines correspond to the theoretical phase speed of the topographic Rossby wave and dashed lines to the theoretical phase speed of the Kelvin wave for a layer thickness equals to 833 m. Colors are given in the legend.

The phase speed of the dam break wave (Fig. 4.15a) is closer to the Kelvin wave phase speed for the same parameters than in the simulations ($\Delta\rho$ and initial layer thickness). The layer thickness of 833 m corresponds to the initial layer thickness where we track the velocity of the wave. The phase speed of the inflow wave (Fig. 4.15b) is in good agreement with the theoretical phase speed of the Kelvin wave. We can conclude that the dam break and the inflow both generate a cyclonic Kelvin wave.

4.5 Perturbation of the northern inflow

After reaching the steady state, we increase or decrease the inflow transport (initially equals to 1.5 Sv) during a period of 5 days and after that we come back to the initial transport. This perturbation in the inflow transport generates a wave which propagates along the boundary toward the channel.

It is possible to track the propagation of the wave around the upstream basin looking at the layer thickness variations (Fig. 4.16). The wave is cyclonic, reaches

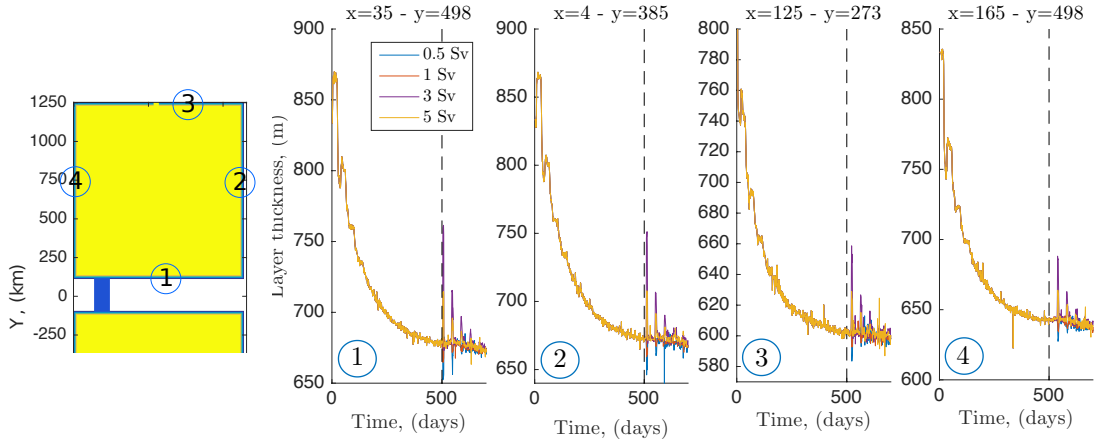

Figure 4.16: Time series of the layer thickness at different locations of the upstream basin. The localization of the time series is summarized on the left figure on the basins bathymetry. After reaching the steady state at 500 days, we decrease the inflow transport to 0.5 Sv (blue) or 1 Sv (orange), or we increase the inflow transport to 3 Sv (yellow) or 5 Sv (violet).

the channel in 29 days and takes 41 days to travel around the upstream basin. A decrease in the inflow transport generates a wave with a negative layer thickness anomaly and an increase a positive layer thickness anomaly. We can also notice the decrease of magnitude of the layer thickness displacement after each passage.

If we look at the time evolution of the layer thickness in the channel (Fig. 4.17), we can see that the wave have an effect in the channel. In fact, a part of the wave is reflected and another part is refracted on the channel. We can notice that the wave has only a effect on the western wall of the channel because the effect of the rotation constrains the lower layer flow to the western flank of the channel (see Fig. 4.14).

As the wave modifies the layer thickness, it also changes the transport through the channel (Fig. 4.18), increasing or decreasing the transport, according to the perturbation, at each passage from the upstream basin toward the downstream basin.

4.6 Discussion and conclusion

The numerical simulations without and with an inflow/outflow have a anti-cyclonic circulation in the thin bottom layer due to the potential vorticity balance in the basins. Unfortunately, Stern's criterion does not allow to conclude on the fact that the flow in the channel is hydraulically controlled, due to the presence of separated flows in our simulations. Based on the local Froude number and on the configuration

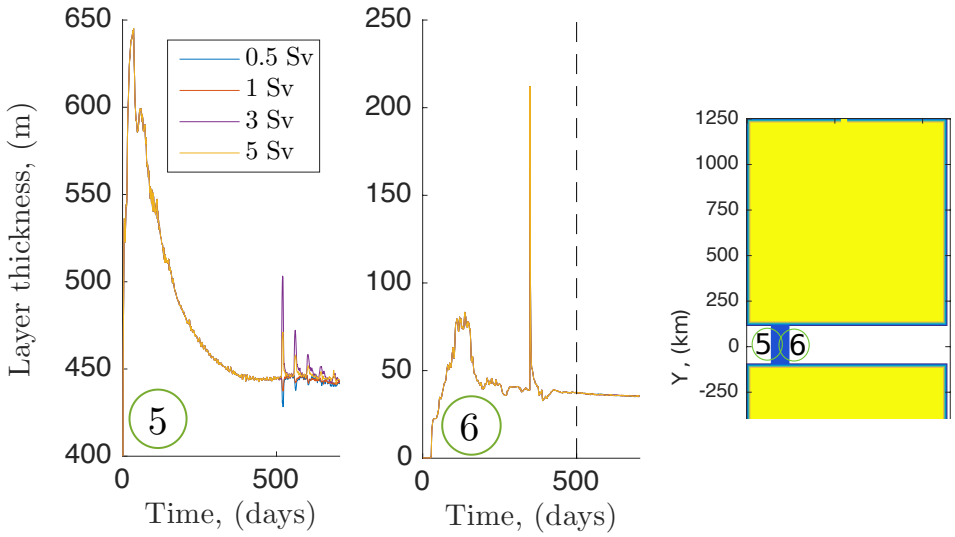

Figure 4.17: Time series of the layer thickness on each wall of the channel. The localization of the time series is summarized on the right figure on the basins bathymetry. After reaching the steady state at 500 days, we decrease the inflow transport to 0.5 Sv (blue) or 1 Sv (orange), or we increase the inflow transport to 3 Sv (yellow) or 5 Sv (violet).

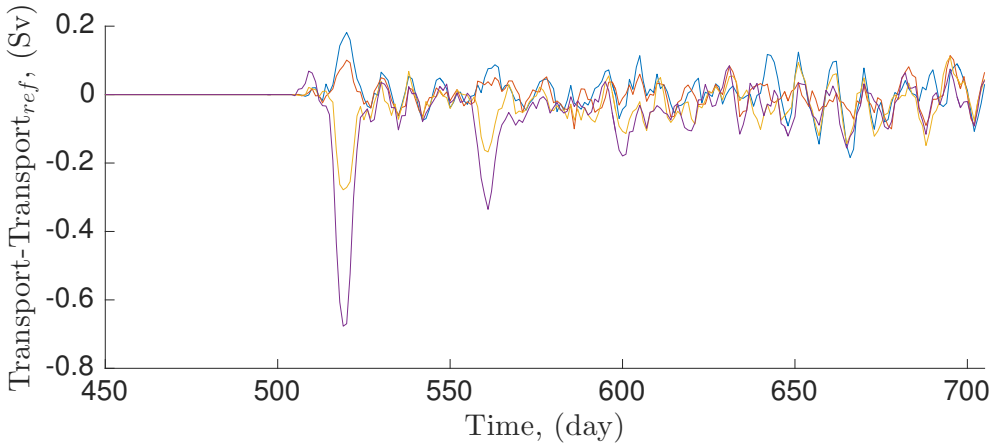

Figure 4.18: Time series of the difference between the perturb transport and the transport with a constant inflow at 1.5 Sv through the channel. After reaching the steady state at 500 days, we decrease the inflow transport to 0.5 Sv (blue) or 1 Sv (orange), or we increase the inflow transport to 3 Sv (yellow) or 5 Sv (violet).

of the domain, we can conclude with some confidence though that the flow is hydraulically controlled but more investigation is necessary to find a robust criterion.

The dam break in the channel and the initialization of the inflow generate two cyclonic waves which propagate in the upstream basin with the coast on their right. After comparison with the theoretical formula of topographic Rossby and Kelvin

waves, the simulated waves are found to be close to Kelvin waves. These waves turn around cyclonically in the upstream basin until dissipation. A perturbation in the inflow, generates a new Kelvin wave which propagates all around the upstream basin. Nevertheless, a part of the Kelvin wave is refracted in the channel and propagates downstream. This interaction with the sill modifies the transport periodically, with a period equal to the time needed for the Kelvin wave to go around the upstream basin. In fact, the Kelvin wave goes around the upstream basin and at each passage it interacts with the sill and a part of the Kelvin wave is transmitted to the downstream basin modifying less and less the transport through the channel.

These results suggest that the interaction between a wave and a hydraulically controlled sill modulates the transport of water from a basin to another. The presence of long-waves in the Nordic Seas could explain the variability of the transport of Denmark Strait Overflow Water observed at the Denmark Strait.

5

Main results of the thesis and perspectives

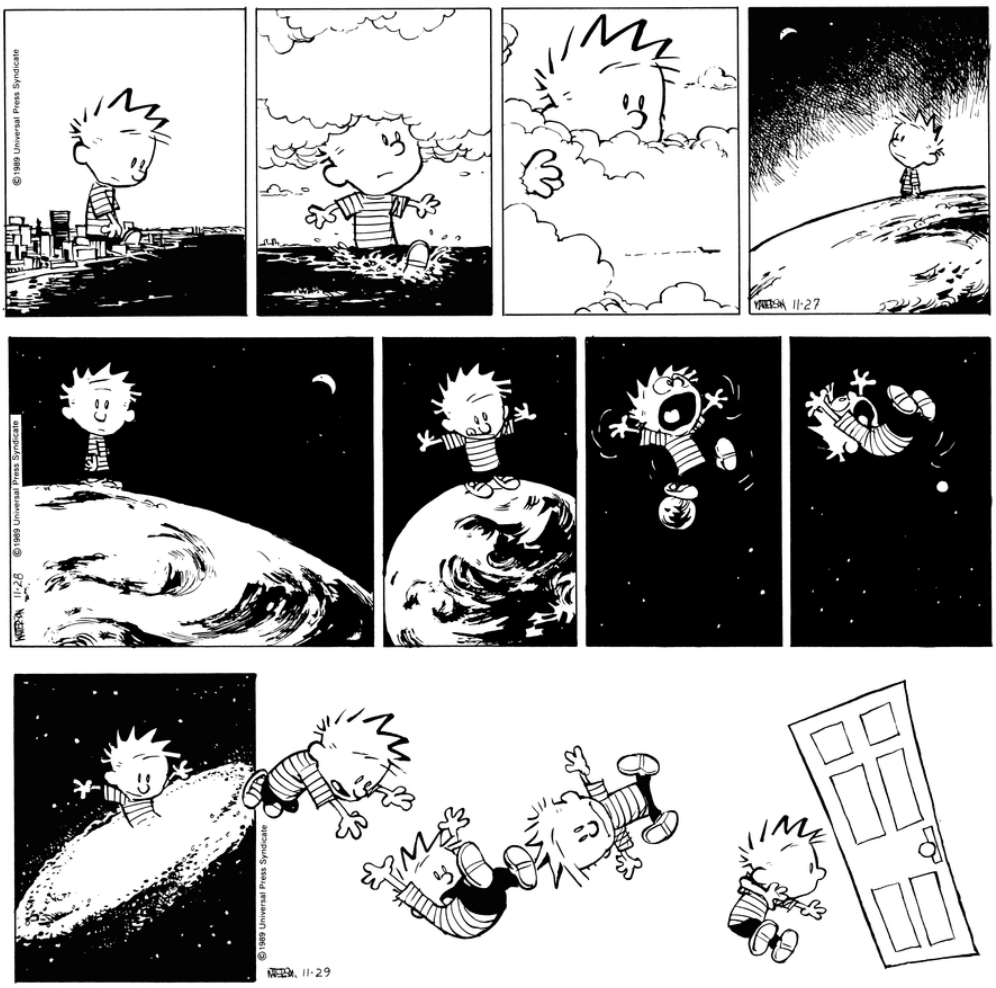

Bill Watterson, 27-28-29 November 1989

5.1 Conclusions on the projects

The oceanic circulation involves various time and spatial scales making its modeling challenging. In fact, high resolution in time and space is necessary for small and fast phenomena like internal waves which need small scales in the topography. On the other hand, the ocean is so vast that for global modeling, large domains are necessary, thus the spatial and temporal resolutions need to be degraded due to the high computational cost. It is for this reason that large ocean modeling studies are completed by high resolution modeling to understand the small-scales phenomena and hence parametrize them in the large-scale models.

With this goal in mind, we studied the spatial distribution of tidal dissipation, and the physical processes responsible for the internal tide instability and dissipation. The mixing induced by tidal dissipation is known to be key in large-scale models. More precisely, we demonstrated that the latitudinal dependence of the tidal energy dissipation is sensitivity to the presence of a mean current. This sensitivity is induced by a change in the frequency of the waves by Doppler effect. Different scales of the waves are shifted with different magnitude due to the multichromatic topography, yielding a wide range of critical latitudes and hence a smoother latitudinal dependence. This result implies that near the critical latitude, the local energy dissipation is lower than expected from idealized studies neglecting background mean flows. Therefore, more waves escape and propagate away from the topography. Those waves carry energy away from the topography and can dissipate their energy in remote locations, participating in the non-local consumption of bottom water.

In this thesis, we also clarified the physical process responsible for the instability and dissipation of internal tide near topography, and its sensitivity to latitude in the absence of mean flow. We highlighted the key role of triad resonant instabilities involving near-inertial waves and waves at $\omega_0 - f$. The latter triad extracts energy from the internal tide equatorward of the critical latitude. The strong increase in energy dissipation toward the critical latitude is due to smaller and smaller vertical scales of the secondary waves which easily locally dissipate. Poleward of the critical latitude, significant dissipation persists for a few degrees of latitude latitude, though the waves at $\omega_0 - f$ fall outside of the internal wave frequency range. This dissipation is therefore not from triad interactions, but instead is induced by energy transfers to evanescent waves which seems to be as efficient as the triadic resonant

instability.

At larger scales, long waves also play a role in the oceanic circulation. Their generation is associated with a disturbance in the system, such as the inflow transport which is the case studied here. In the configuration of a hydraulically controlled sill, we find that the upstream flow is controlled by the sill. This implies that a long wave generated by a disturbance interacts with the sill modifying the volume of water exported in the downstream basin. In our idealized model, the inflow perturbation generates Kelvin and topographic waves which propagate around the upstream basin. At each turn, they interact with the sill modifying temporarily the transport through the channel. This change in the upstream outflow is associated with the partial refraction of the wave at the sill, the remaining fraction of the wave being reflected and continuing to propagate in the upstream basin. More investigation is needed to find the valid Froude number for this basin configuration, to validate the hydraulic control of the sill. Additionally, to be closer to the Nordic seas configuration, we will investigate the propagation of the waves around an island and how it will modify the upstream circulation.

5.2 Future work

Following the idea of energy dissipation by internal waves, we are currently working on a new project on the dissipation of mesoscale eddy energy by interaction with rough topography. As in internal tides dissipation, the interaction of the eddy with the topography generates internal waves and more precisely lee waves. The generation of lee waves seems to be an efficient way to dissipate the energy of the eddy with 80 % of the total volume-integrated energy dissipated below 1 km depth in high-resolution simulations of the Southern Ocean [Nikurashin et al. 2012]. To explain the eddy energy dissipation and energy transfer to waves, we will run high-resolution 3D numerical simulations.

The planned configuration of the simulations, presented in figure 5.1, is one barotropic eddy sitting on rough topography or on a flat bottom for comparison. The eddy will be in equilibrium with the temperature field. The diameter of the eddy will be on the order of 30 km. The generation of lee waves by an eddy speed of ~ 5 cm s^{-1} imposes horizontal topography scales of the order of 300 m to 1500 m ($f < Uk < N$, where f is the Coriolis frequency, U the eddy speed, k the horizontal wavenumber of the topography and N the stratification). A configuration with a horizontal resolution of 200 m and a vertical resolution of 20 m can be reached.

The slope of the waves imposes a vertical depth of 3 km so that the wave can cross the eddy. In order to prevent the interaction between the eddy and the waves radiating outside the domain, lateral sponge layers will be added. All these constraints lead to a domain of 100 km in both horizontal directions and 3 km in the vertical. The purpose of this study is to understand the energy transfer near the topography, so we consider a constant stratification representative of the deep ocean, with a constant stratification with $N = 10^{-3}$ s^{-1}.

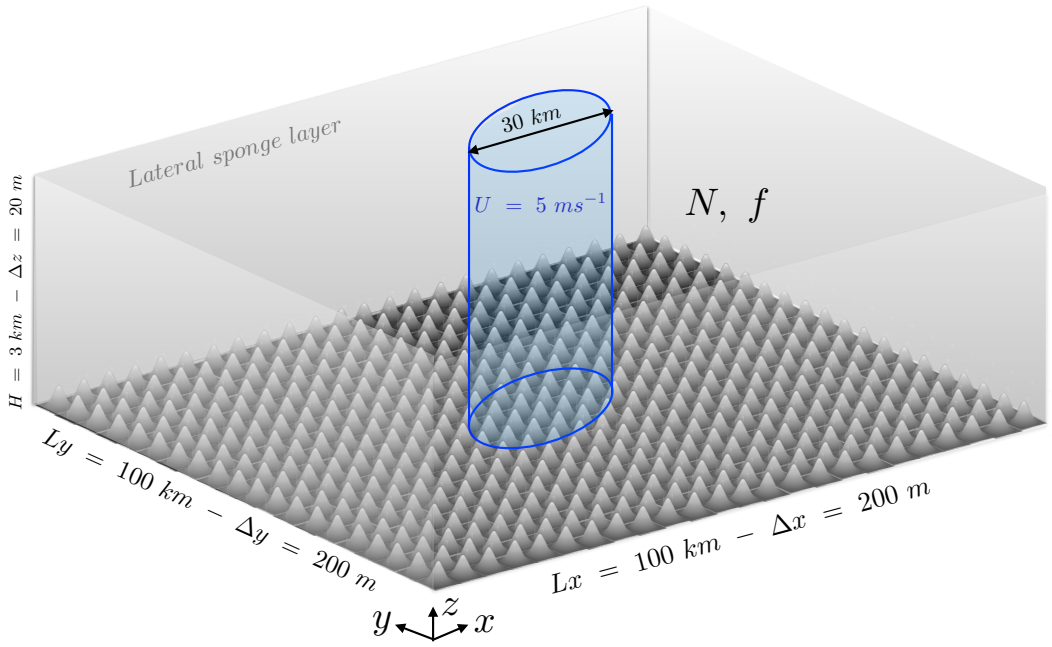

Figure 5.1: Sketch of the numerical setup. The eddy current interacts with a Gaussian topography in a linearly stratified (N constant) and rotating (f constant) fluid. The light gray areas represent the lateral sponge layers.

Mesoscale eddies are ubiquitous in the oceans, and play a crucial role in our climate. They modulate the interaction and exchanges between the atmosphere and the ocean at the ocean surface, and impact the transport of nutrients and thus ecosystems. They also play a key role in the carbon cycle.

The role of internal waves in dissipating mesoscale eddy energy and setting their large-scale properties is still unknown, and is thus of leading order importance in our current climate and in a warming climate.

Bill Watterson, 30 December 1990

Appendices

A

Growth rate calculations

In this section, we develop the full growth rate calculation for a triadic resonant instability in a rotating frame, following Bourget et al. [2013] and Maurer et al. [2016].

Using Equations (2.1), (2.2) and (2.3), and introducing the streamfunction ψ with $\mathbf{u} = (\partial_z \psi, v, -\partial_x \psi)$ (recall that the velocity v is constant in our setting), we obtain a new set of equations

$$\frac{\partial \nabla^2 \psi}{\partial t} + J(\nabla^2 \psi, \psi) - f\frac{\partial v}{\partial z} = -\frac{\partial b}{\partial x} + \nu \Delta^2 \psi, \tag{A.1}$$

$$\frac{\partial v}{\partial t} + J(v, \psi) + f\frac{\partial \psi}{\partial z} = \nu \Delta v, \tag{A.2}$$

$$\frac{\partial b}{\partial t} + J(b, \psi) = N^2 \frac{\partial \psi}{\partial x}, \tag{A.3}$$

where J is the Jacobian operator such as $J(A, B) = \partial_x A \partial_z B - \partial_z A \partial_x B$. We are interested in triadic interactions, so we are looking for solutions of the form

$$\psi = \sum_{j=0}^{2} \Psi_j(t) e^{i(\mathbf{k_j}\cdot\mathbf{r} - \omega_j t)} + c.c., \tag{A.4}$$

$$v = \sum_{j=0}^{2} V_j(t) e^{i(\mathbf{k_j}\cdot\mathbf{r} - \omega_j t)} + c.c., \tag{A.5}$$

$$b = \sum_{j=0}^{2} R_j(t) e^{i(\mathbf{k_j}\cdot\mathbf{r} - \omega_j t)} + c.c., \tag{A.6}$$

where $\mathbf{k_j} = (k, 0, m)$ is the wavevector. Using these solutions in Equations (A.1), (A.2) and (A.3), we obtain

$$\sum_{j=0}^{2}[-\kappa_j^2(\dot{\Psi}_j - i\omega_j\Psi_j) + ik_jR_j - \nu\kappa_j^4\Psi_j - ifm_jV_j]e^{i(\mathbf{k_j}\cdot\mathbf{r}-\omega_j t)} + c.c. = -J(\Delta\psi,\psi) \quad \text{(A.7)}$$

$$\sum_{j=0}^{2}[\dot{V}_j - i\omega_jV_j + \nu\kappa_j^2V_j + ifm_j\Psi_j]e^{i(\mathbf{k_j}\cdot\mathbf{r}-\omega_j t)} + c.c. = -J(v,\psi) \quad \text{(A.8)}$$

$$\sum_{j=0}^{2}[\dot{R}_j - i\omega_jR_j - iN^2k_j\Psi_j]e^{i(\mathbf{k_j}\cdot\mathbf{r}-\omega_j t)} + c.c. = -J(b,\psi) \quad \text{(A.9)}$$

where $\kappa_j = \sqrt{k_j^2 + m_j^2}$. The Jacobian terms on the right handside can be rearranged. The usual inviscid linear dynamics of (A.8) and (A.9) provides the polarization relation

$$R_j = -\frac{N^2k_j}{\omega_j}\Psi_j, \quad \text{(A.10)}$$

$$V_j = \frac{fm_j}{\omega_j}\Psi_j. \quad \text{(A.11)}$$

After some calculations on Equations (A.7), (A.8) and (A.9), they become

$$\begin{aligned} J(\Delta\psi,\psi) = &\sum_{p=0}^{2}\sum_{q\neq p}[(k_pm_q - m_pk_q)\kappa_p^2\Psi_p\Psi_q]e^{i[(\mathbf{k_p}+\mathbf{k_q})\cdot\mathbf{r}-(\omega_p+\omega_q)t]} \\ &-[(k_pm_q - m_pk_q)\kappa_p^2\Psi_p\Psi_q^\star e^{i[(\mathbf{k_p}-\mathbf{k_q})\cdot\mathbf{r}-(\omega_p-\omega_q)t]}] + c.c. \end{aligned} \quad \text{(A.12)}$$

$$\begin{aligned} J(v,\psi) = &\sum_{p=0}^{2}\sum_{q\neq p}[(-k_pm_q + m_pk_q)V_p\Psi_q]e^{i[(\mathbf{k_p}+\mathbf{k_q})\cdot\mathbf{r}-(\omega_p+\omega_q)t]} \\ &-[(-k_pm_q + m_pk_q)V_p\Psi_q^\star e^{i[(\mathbf{k_p}-\mathbf{k_q})\cdot\mathbf{r}-(\omega_p-\omega_q)t]}] + c.c. \end{aligned} \quad \text{(A.13)}$$

$$\begin{aligned} J(b,\psi) = &\sum_{p=0}^{2}\sum_{q\neq p}[(k_pm_q - m_pk_q)R_p\Psi_q]e^{i[(\mathbf{k_p}+\mathbf{k_q})\cdot\mathbf{r}-(\omega_p+\omega_q)t]} \\ &-[(-k_pm_q + m_pk_q)R_p\Psi_q^\star e^{i[(\mathbf{k_p}-\mathbf{k_q})\cdot\mathbf{r}-(\omega_p-\omega_q)t]}] + c.c. \end{aligned} \quad \text{(A.14)}$$

We now get the evolution of a particular wavenumber component $(\mathbf{k_r}, \omega_r)$ associated with the streamfunction ψ, in which r = 0,1 or 2, by averaging both the left and the right hand side over the period of that wave. The resonant terms on the right hand side that balance the left hand side correspond to the wave fulfilling the resonant conditions 2.5 and 2.6.

Highlighting only the resonant terms and using the polarization relations (A.10) and (A.11), the Jacobian terms can be rewritten as

$$
\begin{aligned}
J(\nabla^2\psi,\psi) &= (k_1m_2 - m_1k_2)(\kappa_1^2 - \kappa_2^2)\Psi_1\Psi_2 e^{i(\mathbf{k_0}\cdot\mathbf{r}-\omega_0 t)} \\
&-(k_0m_2 - m_0k_2)(\kappa_0^2 - \kappa_2^2)\Psi_0\Psi_2^\star e^{i(\mathbf{k_1}\cdot\mathbf{r}-\omega_1 t)} \\
&-(k_0m_1 - m_0k_1)(\kappa_0^2 - \kappa_1^2)\Psi_0\Psi_1^\star e^{i(\mathbf{k_2}\cdot\mathbf{r}-\omega_2 t)} + NRT,
\end{aligned} \tag{A.15}
$$

$$
\begin{aligned}
J(v,\psi) &= -(k_1m_2 - m_1k_2)f\left(\frac{m_1}{\omega_1} - \frac{m_2}{\omega_2}\right)\Psi_1\Psi_2 e^{i(\mathbf{k_0}\cdot\mathbf{r}-\omega_0 t)} \\
&+(k_0m_2 - m_0k_2)f\left(\frac{m_0}{\omega_0} - \frac{m_2}{\omega_2}\right)\Psi_0\Psi_2^\star e^{i(\mathbf{k_1}\cdot\mathbf{r}-\omega_1 t)} \\
&+(k_0m_1 - m_0k_1)f\left(\frac{m_0}{\omega_0} - \frac{m_1}{\omega_1}\right)\Psi_0\Psi_1^\star e^{i(\mathbf{k_2}\cdot\mathbf{r}-\omega_2 t)} + NRT,
\end{aligned} \tag{A.16}
$$

$$
\begin{aligned}
J(b,\psi) &= (k_1m_2 - m_1k_2)N^2\left(\frac{k_1}{\omega_1} - \frac{k_2}{\omega_2}\right)\Psi_1\Psi_2 e^{i(\mathbf{k_0}\cdot\mathbf{r}-\omega_0 t)} \\
&-(k_0m_2 - m_0k_2)N^2\left(\frac{k_0}{\omega_0} - \frac{k_2}{\omega_2}\right)\Psi_0\Psi_2^\star e^{i(\mathbf{k_1}\cdot\mathbf{r}-\omega_1 t)} \\
&-(k_0m_1 - m_0k_1)N^2\left(\frac{k_0}{\omega_0} - \frac{k_1}{\omega_1}\right)\Psi_0\Psi_1^\star e^{i(\mathbf{k_2}\cdot\mathbf{r}-\omega_2 t)} + NRT,
\end{aligned} \tag{A.17}
$$

where NRT is the acronym for non-resonant terms and they are not relevant for this problem.

At the first order, we make the further assumption that the amplitude Ψ_j varies slowly with respect to the period of the wave. It is therefore appropriate to consider that $\dot{\Psi}_j \ll \omega_j\Psi_j$. Use of this assumption in the derivative of (A.10) and (A.11) yields

$$
\dot{V}_j = \frac{fm_j}{\omega_j}\dot{\Psi}_j, \tag{A.18}
$$

$$
\dot{R}_j = -\frac{N^2k_j}{\omega_j}\dot{\Psi}_j. \tag{A.19}
$$

Using (A.18) in resonant terms of Equation (A.8), we obtain

$$
V_0 = \frac{-\gamma_0\beta_0\Psi_1\Psi_2 + ifm_0\Psi_0 + f\frac{m_0}{\omega_0}\partial_t\Psi_0}{i\omega_0 - \nu\kappa_0^2}, \tag{A.20}
$$

$$
V_1 = \frac{-\gamma_1\beta_1\Psi_0\Psi_2^\star + ifm_1\Psi_1 + f\frac{m_1}{\omega_1}\partial_t\Psi_1}{i\omega_1 - \nu\kappa_1^2}, \tag{A.21}
$$

$$
V_2 = \frac{-\gamma_2\beta_2\Psi_0\Psi_1^\star + ifm_2\Psi_2 + f\frac{m_2}{\omega_2}\partial_t\Psi_2}{i\omega_2 - \nu\kappa_2^2}, \tag{A.22}
$$

where $\gamma_0 = 1$, $\gamma_{1,2} = -1$ and

$$\beta_r = (k_p m_q - m_p k_q)\left(\frac{m_p}{\omega_p} - \frac{m_q}{\omega_q}\right), \tag{A.23}$$

with $(p,q,r) = (0,1,2)$ or any circular permutation. Now, using (A.19) in resonant terms of Equation (A.7)

$$R_0 = -\frac{i}{k_0}\left[\kappa_0^2(\dot{\Psi}_0 - i\omega_0\Psi_0) + \nu\kappa_0^4\Psi_0 - \gamma_0\alpha_0\Psi_1\Psi_2 + if m_0 V_0\right], \tag{A.24}$$

$$R_1 = -\frac{i}{k_1}\left[\kappa_1^2(\dot{\Psi}_1 - i\omega_1\Psi_1) + \nu\kappa_1^4\Psi_1 - \gamma_1\alpha_1\Psi_0\Psi_2^\star + if m_1 V_1\right], \tag{A.25}$$

$$R_2 = -\frac{i}{k_2}\left[\kappa_2^2(\dot{\Psi}_2 - i\omega_2\Psi_2) + \nu\kappa_2^4\Psi_2 - \gamma_2\alpha_2\Psi_0\Psi_1^\star + if m_2 V_2\right], \tag{A.26}$$

where

$$\alpha_r = (k_p m_q - m_p k_q)(\kappa_p^2 - \kappa_q^2), \tag{A.27}$$

with $(p,q,r) = (0,1,2)$ or any circular permutation. Therefore, using all the previous results in Equation (A.9) leads to

$$\frac{N^2 k_0}{\omega_0}\dot{\Psi}_0 + i\omega_0 R_0 + iN^2 k_0\Psi_0 = \gamma_0\delta_0 N^2\Psi_1\Psi_2, \tag{A.28}$$

where

$$\delta_r = (k_p m_q - m_p k_q)\left(\frac{k_p}{\omega_p} - \frac{k_q}{\omega_q}\right), \tag{A.29}$$

with $(p,q,r) = (0,1,2)$ or any circular permutation. Replacing R_0 and V_0 by their expression

$$\begin{aligned}\frac{N^2 k_0^2}{\omega_0^2}\dot{\Psi}_0 + \kappa_0^2(\dot{\Psi}_0 - i\omega_0\Psi_0) + \nu\kappa_0^4\Psi_0 - \gamma_0\alpha_0\Psi_1\Psi_2 \\ + if m_0\left(\frac{-\gamma_0 f\beta_0\Psi_1\Psi_2 + if m_0\Psi_0 + f\frac{m_0}{\omega_0}\dot{\Psi}_0}{i\omega_0 - \nu\kappa_0^2}\right) + i\frac{N^2 k_0}{\omega_0}\Psi_0 = \gamma_0\frac{k_0}{\omega_0}\delta_0 N^2\Psi_1\Psi_2,\end{aligned} \tag{A.30}$$

relating the time derivative of the wave amplitude, Ψ_0, to the other wave amplitudes.

$$\dot{\Psi}_0 = \frac{\gamma_0}{2\kappa_0^2}\left(\alpha_0 + \frac{\delta_0 N^2 k_0}{\omega_0} + \frac{f^2 m_0\beta_0}{\omega_0}\right)\Psi_1\Psi_2 - \frac{1}{2}\nu\left(\kappa_0^2 + \frac{f^2 m_0^2}{\omega_0^2}\right)\Psi_0. \tag{A.31}$$

$$\dot{\Psi}_0 = I_0\Psi_1\Psi_2 - \frac{1}{2}\nu\kappa_0^2\left(1+\frac{f^2m_0^2}{\kappa_0^2\omega_0^2}\right)\Psi_0, \tag{A.32}$$

$$\dot{\Psi}_1 = I_1\Psi_0\Psi_2^\star - \frac{1}{2}\nu\kappa_1^2\left(1+\frac{f^2m_1^2}{\kappa_1^2\omega_1^2}\right)\Psi_1, \tag{A.33}$$

$$\dot{\Psi}_2 = I_2\Psi_0\Psi_1^\star - \frac{1}{2}\nu\kappa_2^2\left(1+\frac{f^2m_2^2}{\kappa_2^2\omega_2^2}\right)\Psi_2, \tag{A.34}$$

where I_r is

$$\begin{aligned} I_r &= \frac{\gamma_r}{2\kappa_r^2}\left(\alpha_r + \frac{\delta_r N^2 k_r}{\omega_r} + \frac{f^2 m_r \beta_r}{\omega_r}\right) \\ &= \gamma_r \frac{k_p m_q - m_p k_q}{2\omega_r\kappa_r^2}\left[\omega_r(\kappa_p^2-\kappa_q^2) + k_r N^2\left(\frac{k_p}{\omega_p}-\frac{k_q}{\omega_q}\right) + m_r f^2\left(\frac{m_p}{\omega_p}-\frac{m_q}{\omega_q}\right)\right]. \end{aligned} \tag{A.35}$$

We consider Ψ_0 as the primary wave and it is constant in early times since amplitudes of the secondary waves, Ψ_1 and Ψ_2 are negligible compare to the amplitude of Ψ_0. Combining Equations (A.34) and (A.34), we get

$$\ddot{\Psi}_1 = I_1 I_2 \Psi_0^2\Psi_1 - \frac{1}{4}\nu^2\kappa_1^2\kappa_2^2\left(1+\frac{f^2m_1^2}{\kappa_1^2\omega_1^2}\right)\left(1+\frac{f^2m_2^2}{\kappa_2^2\omega_2^2}\right)\Psi_1 - \frac{1}{2}\nu\left(\kappa_1^2+\kappa_2^2+\frac{f^2m_1^2}{\omega_1^2}+\frac{f^2m_2^2}{\omega_2^2}\right)\dot{\Psi}_1. \tag{A.36}$$

The solution of Equation (A.36) is of the form $\Psi_{1,2} = A_{1,2}e^{\sigma_+ T} + B_{1,2}e^{\sigma_- T}$, where σ is the growth rate defined as (2.8).

B

PSI extension calculations

In this part, we give a brief description of the 2f-pump mechanism described in detail in Young et al. [2008]. Of particular interest is the derivation of the growth rate (Equation 2.12). We consider the interaction of a background flow (U, V, W) with a pure inertial oscillation. W is a function of time t and depth z and is given by the incompressibility condition $U_x + V_y + W_z = 0$. For us, a pure inertial oscillation is a disturbance with infinite horizontal spatial scales which implicates that the velocity is $(u(z,t), v(z,t), 0)$. A pure inertial oscillation has no pressure or buoyancy signal so that its dynamic is entirely governed by the horizontal momentum equations, after removing second order terms,

$$u_t + Wu_z + uU_x + vU_y - fv = 0, \tag{B.1}$$

$$v_t + Wv_z + uV_x + vV_y + fu = 0. \tag{B.2}$$

Rewriting Equations (B.1) and (B.2) in term of the 'back-rotated' velocity $\Omega \equiv (u + iv)e^{ift}$, we obtain

$$\Omega_t + W\Omega_z + \frac{1}{2}\left[(U_x + V_y) + i(V_x - U_y)\right]\Omega + \frac{1}{2}\left[(U_x - V_y) + i\left(V_x + U_y\right)\right]e^{2ift}\Omega^\star = 0. \tag{B.3}$$

We consider that the background flow and the near-inertial oscillation interact weakly so that the envelope of $\Omega(z,t)$ is evolving slowly relative to the inertial time scale. The secular evolution of $\Omega(z,t)$ (evolution on really long time period) is then obtained by time-averaging (denoted by an overbar) Equation (B.3) over an interval which is long relative to f^{-1}

$$\overline{\Omega}_t + \frac{1}{2}i\zeta\overline{\Omega} + \frac{1}{2}\Upsilon\overline{\Omega}^\star = 0, \tag{B.4}$$

where

$$\zeta \equiv \overline{V}_x - \overline{U}_y, \tag{B.5}$$

is the vertical velocity of the low-frequency part of the background flow, assuming that the low-frequency part of the background flow is geostrophycally balanced so that $\overline{W} = \overline{U}_x + \overline{V}_y = 0$. The term involving $\frac{1}{2}i\zeta$ in Equation (B.4) corresponds to Kunze [1985]'s result that the effective inertial frequency is shifted away from the local inertial frequency by half the relative vorticity of the low-frequency geostrophic background flow. The second coefficient Υ in Equation (B.4) is the amplitude of the $2f$-pump

$$\Upsilon \equiv \overline{\left[(U_x - V_y) + i\,(V_x + U_y)\right] e^{2ift}}, \tag{B.6}$$

which is non-zero if the background flow strain rates have spectral content at $2f$.

Now we consider the propagation of near-inertial oscillations through a geostrophic flow which changes slowly relative to the inertial period. The background flow has two components: a geostrophic component (denoted by subscript g) and a $2f$-pump flow (denoted by subscript p). There is no transfer of energy between the geostrophic part of the background flow and the near-inertial waves [Young and Jelloul 1997]. Thus, the $2f-$pump part of the background flow plays the essential role of energizing the near-inertial oscillations. The dynamics of the near-inertial field (u, v, w, b, p) is given by the linearized Boussinesq equations around the background flow (U, V, W, B, P)

$$u_t + Uu_x + Vu_y + Wu_z + uU_x + vU_y + wU_z - fv + p_x = 0, \tag{B.7}$$

$$v_t + Uv_x + Vv_y + Wv_z + uV_x + vV_y + wV_z + fu + p_y = 0, \tag{B.8}$$

$$-b + p_z = 0, \tag{B.9}$$

$$u_x + v_y + w_z = 0, \tag{B.10}$$

$$b_t + Ub_x + Vb_y + Wb_z + uB_x + vB_y + wB_z + wN^2 = 0. \tag{B.11}$$

We emphasize that PSI is driven solely and essentially by the pump component of the background flow. Young et al. [2008]'s calculations lead to the evolution equation of near-inertial fields ($f-$plane, uniform N, $\partial_y \equiv 0$ and magnitude of ϖ is too small to affect the solution [Young et al. 2008])

$$A_{zzt} + \frac{1}{2}\frac{N^2}{f} i A_{xx} + \frac{1}{2}\Upsilon A^{\star}_{zz} = 0, \tag{B.12}$$

Considering now the instability of an infinite-plane internal gravity wave with a uniform stratification on an f-plane. Its pressure is given by

$$P_p = a\cos\phi, \tag{B.13}$$

where $\phi = kx + mz - \omega_0 t$ and $a = \frac{U_0 h_0 m(\omega_0^2 - f^2)}{k\omega_0}$ is the amplitude of the pump.

The frequency and the wavenumber are related by the non-hydrostatic dispersion relation (2.4). Since, we consider ω_0 close to $2f$, we write

$$\omega_0 = 2f + \epsilon, \tag{B.14}$$

with $\epsilon \ll f$, where the de-tunning frequency ϵ, might be either positive or negative; in our case, we consider a negative de-tuning.

Substituting the pressure into the linearized Boussinesq equations, we obtain the other pump fields

$$U_p = \frac{ak\omega_0}{(\omega_0^2 - f^2)}\cos\phi, \tag{B.15}$$

$$V_p = \frac{afk}{(\omega_0^2 - f^2)}\sin\phi, \tag{B.16}$$

$$W_p = -\frac{ak^2\omega_0}{m(\omega_0^2 - f^2)}\cos\phi, \tag{B.17}$$

$$B_p = -\frac{ak^2N^2}{m(\omega_0^2 - f^2)}\sin\phi. \tag{B.18}$$

From there, we want to calculate the amplitude of the $2f$-pump from Equation (B.6), considering $\partial_y \equiv 0$. Thus

$$U_{px} + iV_{px} = \partial_x Re(\widetilde{U}_p e^{i\phi}) + i\partial_x Re(\widetilde{V}_p e^{i\phi}) = \frac{iak^2e^{i\phi}}{2(\omega_0 - f)} - \frac{iak^2e^{-i\phi}}{2(\omega_0 + f)} \tag{B.19}$$

and therefore

$$\Upsilon = \overline{(U_{px} + iV_{px})e^{2ift}} = i\lambda e^{i(kx+mz-\epsilon t)}, \tag{B.20}$$

where

$$\lambda^2 = \frac{U_0 h_0 k_0^2}{2\omega_0}\sqrt{\frac{(N^2 - \omega_0^2)(\omega_0 + f)}{(\omega_0 - f)}}. \tag{B.21}$$

Replacing Υ by its expression in Equation (B.12), we obtain

$$A_{zzt} + \frac{1}{2}\frac{N^2}{f}iA_{xx} + \frac{1}{2}i\lambda e^{i(kx+mz-\epsilon t)}A^{\star}_{zz} = 0. \tag{B.22}$$

The solution of this equation is of the form

$$A = e^{-i\epsilon t/2}\left[A_1(t)e^{i(k_1x+m_1z)} + A_2^{\star}(t)e^{i(k_2x+m_2z)}\right]. \tag{B.23}$$

Now, we use the spatial resonant condition (2.5) in Equation (B.23) leading to

$$A_{1t} + i\left(\frac{N^2k_1^2}{2fm_1^2} - \frac{\epsilon}{2}\right)A_1 + \frac{i\lambda m_2^2}{2m_1^2}A_2 = 0, \tag{B.24}$$

$$A_{2t} - i\left(\frac{N^2k_2^2}{2fm_2^2} - \frac{\epsilon}{2}\right)A_2 - \frac{i\lambda m_1^2}{2m_2^2}A_1 = 0. \tag{B.25}$$

Combining the two previous equations, we obtain a single equation for $A_1(t)$

$$A_{1tt} + i\left(\frac{N^2k_1^2}{2fm_1^2} - \frac{N^2k_2^2}{2fm_2^2}\right)A_{1t} + \left(\frac{N^2k_1^2}{2fm_1^2}\frac{N^2k_2^2}{2fm_2^2} - \frac{\lambda^2}{4}\right)A_1 = 0. \tag{B.26}$$

If $A_1 = \widehat{A}_1 e^{st}$ then

$$s = \frac{1}{2}\left(\frac{N^2k_1^2}{2fm_1^2} - \frac{N^2k_2^2}{2fm_2^2}\right)i \pm \frac{1}{2}\sqrt{\lambda^2 - \left(\frac{N^2k_1^2}{2fm_1^2} + \frac{N^2k_2^2}{2fm_2^2}\right)^2}. \tag{B.27}$$

Finally, the growth rate is $\sigma = \mathrm{Re}(s)$, such as

$$\sigma = \frac{1}{2}\sqrt{\lambda^2 - \left(\frac{N^2}{2f}\right)^2\left(\frac{k_1^2}{m_1^2} + \frac{k_2^2}{m_2^2} - 2\frac{\epsilon f}{N^2}\right)^2}. \tag{B.28}$$

C

Mean current

In this Appendix, we show that adding a mean current to the simulations of internal tides does not impact significantly the generation of internal tides at the topography. Indeed, we want to investigate the impact of a mean current on the propagation and dissipation of waves, not on their generation.

In order to ensure minimal interaction of the mean current with topography, we start increasing the strength of the mean current near the highest topography peak. The amplitude of U_{mc} increases from 0 near the maximum height of topography to αU_{tide} a hunder meters above that height.

In the simulations discussed in the paper, the shear layer starts at $z = 500$ m and ends at 600 m above which the mean current is constant (Fig. 3.1). Here we show that even if the shear layer is lowered between $z = 400$ m and 500 m to accentuate the generation of lee waves by the mean current, the generation and the energy dissipation of those lee waves are negligible compared to the internal tides discussed in the paper. The mean current used in the paper (starting higher at 500 m) yields even weaker lee waves and dissipation.

Fig. C.1 (top and middle panels) shows snapshots of a simulation with mean current only (no barotropic tide). Some lee waves are generated at the highest topographic peaks, but the signal is very weak compared to the internal tides shown Fig. 3.2 or 3.5. The energy dissipation associated to those lee waves is small compared to the energy dissipation associated to internal tides (Fig. C.1 bottom panel). We are therefore confident that the presence of lee waves does not impact the results presented here.

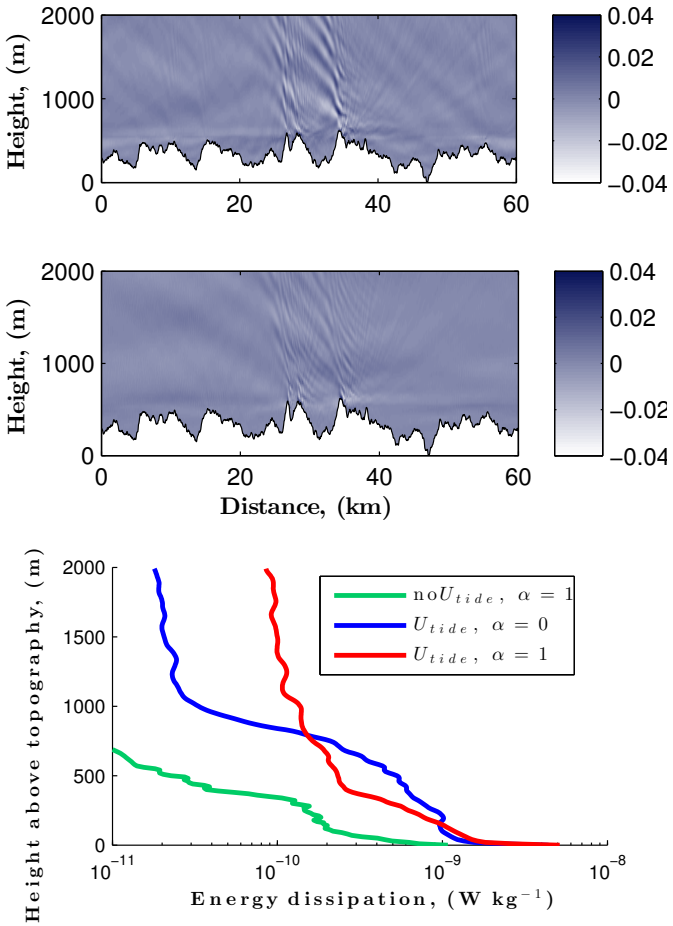

Figure C.1: Snapshots of the wave zonal velocity (m s^{-1}) from the simulation without a tidal flow ($f = 0.7 \times 10^{-4}$ s^{-1}, $\alpha = 1$ and $U_{tide} = 0$ m.s^{-1}) after 5 days (top) and 19 days (middle) of simulation. The bottom panel shows the vertical profile of energy dissipation averaged over the last 10 days of the simulation. For comparison, the vertical profiles with tidal forcing are repeated from Fig. 3.6.

Bibliography

Aagaard, K. (1970). Wind-driven transports in the greenland and norwegian seas. *Deep Sea Research and Oceanographic Abstracts*, 17(2):281–291.

Alford, M., MacKinnon, J., Zhao, Z., Pinkel, R., Klymak, J., and Peacock, T. (2007). Internal waves across the pacific. *Geophys. Res. Lett.*, 34(24).

Bell, T. H. (1975). Lee waves in stratified flows with simple harmonic time dependence. *J. Fluid Mech.*, 67:705–722.

Booker, J. R. and Bretherton, F. P. (1967). The critical layer for internal gravity waves in a shear flow. *J. Fluid Mech.*, 27:513–539.

Bourget, B., Dauxois, T., Joubaud, S., and Odier, P. (2013). Experimental study of parametric subharmonic instability for internal plane waves. *J. Fluid Mech.*, 723:1–20.

Bourget, B., Scolan, H., Dauxois, T., Le Bars, M., Odier, P., and Joubaud, S. (2014). Finite-size effects in parametric subharmonic instability. *J. Fluid Mech.*, 759:739–750.

Bouruet-Aubertot, P., Sommeria, J., and Staquet, C. (1995). Breaking of standing internal gravity waves through two-dimensional instabilities. *J. Fluid Mech.*, 285:265–301.

Broecker, W. S. (1987). Unpleasant surprises in the greenhouse? *Nature*, 328(6126):123–126.

Curry, R. and Mauritzen, C. (2005). Dilution of the northern north atlantic ocean in recent decades. *Science*, 308(5729):1772–1774.

De Lavergne, C., Madec, G., Le Sommer, J., and Nurser, A. J. G.and Naveira Garabato, A. C. (2016a). The impact of a variable mixing efficiency on the abyssal overturning. *J. Phys. Oceanogr.*, 46(2):663–681.

De Lavergne, C., Madec, G., Le Sommer, J., Nurser, A. J. G., and Naveira Garabato, A. C. (2016b). On the consumption of antarctic bottom water in the abyssal ocean. *J. Phys. Oceanogr.*, 46(2):635–661.

Dickson, R. R. and Brown, J. (1994). The production of north atlantic deep water: sources, rates, and pathways. *Journal of Geophysical Research: Oceans*, 99(C6):12319–12341.

Dushaw, B. D., Howe, B. M., Cornuelle, B. D., Worcester, P. F., and Luther, D. S. (1995). Barotropic and baroclinic tides in the central North Pacific Ocean determined from long-range reciprocal acoustic transmissions. *J. Phys. Oceanogr.*, 25(4):631–647.

Egbert, G. and Ray, R. (2000). Significant dissipation of tidal energy in the deep ocean inferred from satellite altimeter data. *Nature*, 405(6788):775.

Emery, W. J. and Meincke, J. (1986). Global water masses: summary and review. *Oceanol. Acta*, 9:383–391.

Ferrari, R. (2014). What goes down must come up. *Nature*, 513(7517):179–180.

Ferrari, R., Jansen, M. F., Adkins, J. F., Burke, A., Stewart, A. L., and Thompson, A. F. (2014). Antarctic sea ice control on ocean circulation in present and glacial climates. *Proc. Natl. Acad. Sci. (USA)*, 111(24):8753–8758.

Ferrari, R., Mashayek, A., McDougall, T. J., Nikurashin, M., and Campin, J.-M. (2016). Turning ocean mixing upside down. *J. Phys. Oceanogr.*, 46(7):2239–2261.

Ganachaud, A. and Wunsch, C. (2000). Improved estimates of global ocean circulation, heat transport and mixing from hydrographic data. *Nature*, 408(6811):453.

Garrett, C. and Kunze, E. (2007). Internal tide generation in the deep ocean. *Annu. Rev. Fluid Mech.*, 39:57–87.

Garrett, C. and Munk, W. (1979). Internal waves in the ocean. *Annu. Rev. Fluid Mech.*, 11(1):339–369.

Gemmrich, J. and Klymak, J. M. (2015). Dissipation of internal wave energy generated on a critical slope. *J. Phys. Oceanogr.*, 45(9):2221–2238.

Gerkema, T. (2001). Internal and interfacial tides: beam scattering and local generation of solitary waves. *J. Mar. Res.*, 59(2):227–255.

Girton, J. B., Pratt, L. J., Sutherland, D. A., and Price, J. F. (2006). Is the faroe bank channel overflow hydraulically controlled? *Journal of physical oceanography*, 36(12):2340–2349.

Goff, J. A. and Arbic, B. K. (2010). Global prediction of abyssal hill roughness statistics for use in ocean models from digital maps of paleo-spreading rate, paleo-ridge orientation, and sediment thickness. *Ocean Modelling*, 32(1):36–43.

Goff, J. A. and Jordan, T. H. (1989). Stochastic modeling of seafloor morphology: a parameterized gaussian model. *Geophys. Res. Lett.*, 16(1):45–48.

Gordon, A. L. (2002). Bottom water formation. *Encyclopedia of ocean sciences*, pages 334–340.

Grisouard, N. and Bühler, O. (2012). Forcing of oceanic mean flows by dissipating internal tides. *J. Fluid Mech.*, 708:250–278.

Hansen, B. and Østerhus, S. (2000). North atlantic–nordic seas exchanges. *Progress in Oceanography*, 45(2):109–208.

Hansen, B. and Østerhus, S. (2007). Faroe bank channel overflow 1995–2005. *Progress in Oceanography*, 75(4):817–856.

Hansen, B., Østerhus, S., Turrell, W. R., Jónsson, S., Valdimarsson, H., Hátún, H., and Olsen, S. M. (2008). The inflow of atlantic water, heat, and salt to the nordic seas across the greenland–scotland ridge. In *Arctic–Subarctic Ocean Fluxes*, pages 15–43.

Harden, B. E., Pickart, R. S., Valdimarsson, H., Våge, K., de Steur, L., Richards, C., Bahr, F., Torres, D., Børve, E., Jónsson, S., et al. (2016). Upstream sources of the denmark strait overflow: Observations from a high-resolution mooring array. *Deep Sea Research Part I: Oceanographic Research Papers*, 112:94–112.

Hattermann, T., Isachsen, P. E., von Appen, W.-J., Albretsen, J., and Sundfjord, A. (2016). Eddy-driven recirculation of atlantic water in fram strait. *Geophysical Research Letters*, 43(7):3406–3414.

Hazewinkel, J. and Winters, K. (2011). PSI of the internal tide on a beta plane: flux divergence and near-inertial wave propagation. *J. Phys. Oceanogr.*, 41(9):1673–1682.

Huang, R. X. (1999). Mixing and energetics of the thermohaline circulation. *J. Phys. Oceanogr.*, 29:727–746.

Huang, R. X. (2010). *Ocean Circulation: wind-driven and thermohaline processes*. Cambridge university press.

Jayne, S. R. (2009). The Impact of Abyssal Mixing Parameterizations in an Ocean General Circulation Model. *J. Phys. Oceanogr.*, 39:1756–1775.

Jochumsen, K., Quadfasel, D., Valdimarsson, H., and Jonsson, S. (2012). Variability of the denmark strait overflow: Moored time series from 1996–2011. *Journal of Geophysical Research: Oceans*, 117(C12).

Johnson, G. C. (2008). Quantifying antarctic bottom water and north atlantic deep water volumes. *J. Geophys. Res.*, 113(C5).

Jónsson, S. (1999). The circulation in the northern part of the denmark strait and its variability, l: 6.

Korobov, A. and Lamb, K. G. (2008). Interharmonics in internal gravity waves generated by tide-topography interaction. *J. Fluid Mech.*, 611:61–95.

Kuhlbrodt, T., Griesel, A., Montoya, M., Levermann, A., Hofmann, M., and Rahmstorf, S. (2007). On the driving processes of the Atlantic meridional overturning circulation. *Rev. Geophys.*, 45:RG2001.

Kunze, E. (1985). Near-inertial wave propagation in geostrophic shear. *J. Phys. Oceanogr.*, 15(5):544–565.

Kunze, E., Firing, E., Hummon, J. M., Chereskin, T. K., and Thurnherr, A. M. (2006). Global abyssal mixing inferred from lowered adcp shear and ctd strain profiles. *J. Phys. Oceanogr.*, 36(8):1553–1576.

Lambaerts, J., Lapeyre, G., Plougonven, R., and Klein, P. (2013). Atmospheric response to sea surface temperature mesoscale structures. *J. Geophys. Res.: Atmospheres*, 118(17):9611–9621.

Laplace, P. S. (1775). Recherches sur plusieurs points du système du monde. *Mémoires de l'Académie Royale des Sciences de Paris*, 88:75–182.

Ledwell, J. R., Montgomery, E. T., Polzin, K. L., St. Laurent, L. C., Schmitt, R. W., and Toole, J. M. (2000). Evidence for enhanced mixing over rough topography in the abyssal ocean. *Nature*, 403(6766):179–182.

Lefauve, A., Muller, C., and Melet, A. (2015). A three-dimensional map of tidal dissipation over abyssal hills. *J. Geophys. Res.*, 120(7):4760–4777.

Lueck, R. and Reid, R. (1984). On the production and dissipation of mechanical energy in the ocean. *J. Geophys. Res.*, 89(C3):3439–3445.

Lumpkin, R. and Speer, K. (2007). Global ocean meridional overturning. *J. Phys. Oceanogr.*, 37(10):2550–2562.

Lutgens, F. K. and Tarbuck, E. J. (2001). The atmosphere.

MacKinnon, J. A., Alford, M. H., Sun, O., Pinkel, R., Zhao, Z., and Klymak, J. (2013). Parametric subharmonic instability of the internal tide at 29 n. *J. Phys. Oceanogr.*, 43(1):17–28.

MacKinnon, J. A. and Winters, K. B. (2005). Subtropical catastrophe: Significant loss of low-mode tidal energy at 28.9. *Geophys. Res. Lett.*, 32(15).

Marshall, J., Adcroft, A., Hill, C., Perelman, L., and Heisey, C. (1997). A finite-volume, incompressible navier stokes model for studies of the ocean on parallel computers. *J. Geophys. Res.*, 102(C3):5753–5766.

Marshall, J. and Schott, F. (1999). Open-ocean convection: Observations, theory, and models. *Reviews of Geophysics*, 37(1):1–64.

Mashayek, A., Ferrari, R., Nikurashin, M., and Peltier, W. R. (2015). Influence of Enhanced Abyssal Diapycnal Mixing on Stratification and the Ocean Overturning Circulation. *J. Phys. Oceanogr.*, 45:2580–2597.

Maslowe, S. (1986). Critical Layers in Shear Flows. *Annu. Rev. Fluid Mech.*, 18:405–432.

Mastropole, D., Pickart, R. S., Valdimarsson, H., Vage, K., Jochumsen, K., and Girton, J. B. (2016). Hydrographic Structure of Overflow Water Passing Through Denmark Strait. pages 1–27.

Maurer, P., Joubaud, S., and Odier, P. (2016). Generation and stability of inertia–gravity waves. *J. Fluid Mech.*, 808:539–561.

Mauritzen, C. (1996). Production of dense overflow waters feeding the north atlantic across the greenland-scotland ridge. part 1: Evidence for a revised circulation scheme. *Deep Sea Research Part I: Oceanographic Research Papers*, 43(6):769–806.

McComas, C. H. and Bretherton, F. P. (1977). Resonant interaction of oceanic internal waves. *J. Geophys. Res.*, 82(9):1397–1412.

Melet, A., Legg, S., and Hallberg, R. (2016). Climatic impacts of parameterized local and remote tidal mixing. *Journal of Climate*, 29(10):3473–3500.

Muller, C. J. and Bühler, O. (2009). Saturation of the internal tides and induced mixing in the abyssal ocean. *J. Phys. Oceanogr.*, 39(9):2077–2096.

Müller, P. and Xu, N. (1992). Scattering of oceanic internal gravity waves off random bottom topography. *J. Phys. Oceanogr.*, 22(5):474–488.

Munday, D. R., Allison, L. C., Johnson, H. L., and Marshall, D. P. (2011). Remote forcing of the antarctic circumpolar current by diapycnal mixing. *Geophys. Res. Lett.*, 38(8).

Munk, W. and Wunsch, C. (1998). Abyssal recipes ii: energetics of tidal and wind mixing. *Deep Sea Research Part I: Oceanographic Research Papers*, 45(12):1977–2010.

Munk, W. H. (1966). Abyssal recipes. *Deap-sea Res.*, 13:707–730.

Newton, I. (1687). Philosophiae Naturalis Principia Mathematica. *Newton's principia*.

Nikolopoulos, A., Borenäs, K., Hietala, R., and Lundberg, P. (2003). Hydraulic estimates of denmark strait overflow. *Journal of Geophysical Research: Oceans*, 108(C3).

Nikurashin, M. and Ferrari, R. (2011). Global energy conversion rate from geostrophic flows into internal lee waves in the deep ocean. *Geophys. Res. Lett.*, 38(8):L08610.

Nikurashin, M. and Ferrari, R. (2013). Overturning circulation driven by breaking internal waves in the deep ocean. *Geophys. Res. Lett.*, 40(12):3133–3137.

Nikurashin, M. and Legg, S. (2011). A mechanism for local dissipation of internal tides generated at rough topography. *J. Phys. Oceanogr.*, 41(2):378–395.

Nikurashin, M., Vallis, G. K., and Adcroft, A. (2012). Routes to energy dissipation for geostrophic flows in the Southern Ocean. *Nat. Geosci.*, 6(1):48–51.

Paparella, F. and Young, W. (2002). Horizontal convection is non-turbulent. *J. Fluid Mech.*, 466:205–214.

Polzin, K. L. (2009). An abyssal recipe. *Ocean Modell.*, 30:298–309.

Polzin, K. L., Toole, J. M., Ledwell, J. R., and Schmitt, R. W. (1997). Spatial variability of turbulent mixing in the abyssal ocean. *Science*, 276(5309):93–96.

Pratt, L. and Whitehead, J. A. (2008). Rotating hydraulics. *Rotating Hydraulics, by LLJ Pratt and JA Whitehead. Berlin: Springer, 2008. ISBN 978-0-387-36639-5*, 1.

Pratt, L. J. and Llewellyn Smith, S. G. (1997). Hydraulically drained flows in rotating basins. part i: Method*. *Journal of physical oceanography*, 27(12):2509–2521.

Rahmstorf, S. et al. (1999). Shifting seas in the greenhouse. *Nature*, 399(6736):523–524.

Rainville, L. and Pinkel, R. (2006). Propagation of low-mode internal waves through the ocean. *J. Phys. Oceanogr.*, 36(6):1220–1236.

Ray, R. D. (1999). A global ocean tide model from topex/poseidon altimetry: Got99. 2.

Richet, O., Muller, C., and Chomaz, J.-M. (2017). Impact of a mean current on the internal tide energy dissipation at the critical latitude. *J. Phys. Oceanogr.*, 47(6):1457–1472.

Samelson, R. M. (1998). Large-scale circulation with locally enhanced vertical mixing. *J. Phys. Oceanogr.*, 28(4):712–726.

Sandstrom, J. W. (1908). Dynamicsche Versuche mit Meerwasser. *Annalen der Hydrographie under Maritimen Meteorologie*, 36:6–23.

Sandstrom, J. W. (1916). Meteorologische Studien im schwedischen Hochgebirge. *Goteborgs K. Vetenskaps-och Vitterhetssamhalles Handl.*, 4:22.

St. Laurent, L. and Garrett, C. (2002). The Role of Internal Tides in Mixing the Deep Ocean. *J. Phys. Oceanogr.*, 32(10):2882–2899.

Stammer, D., Wunsch, C., and Ponte, R. (2000). Dealiasing global altimetric records with a general circulation model. *Geophys. Res. Lett.*, 27:1175–78.

Staquet, C. and Sommeria, J. (2002). Internal gravity waves: from instabilities to turbulence. *Annu. Rev. Fluid Mech.*, 34(1):559–593.

Stern, M. E. (1974). Comment on rotating hydraulics. *geophys. Fluid Dyn.*, 6:127–130.

Talley, L. D. (2008). Freshwater transport estimates and the global overturning circulation: Shallow, deep and throughflow components. *Progress in Oceanography*, 78(4):257–303.

Talley, L. D. (2011). *Descriptive physical oceanography: an introduction*. Academic press.

Talley, L. D. (2013). Closure of the global overturning circulation through the indian, pacific, and southern oceans: Schematics and transports. *Oceanography*, 26(1):80–97.

Talley, L. D., Reid, J. L., and Robbins, P. E. (2003). Data-based meridional overturning streamfunctions for the global ocean. *Journal of Climate*, 16(19):3213–3226.

Toggweiller, J. R. and Samuels, B. (1995). Effect of Drake passage on the global thermohaline circulation. *Deep Sea Res.*, 42:477–500.

Våge, K., Pickart, R. S., Spall, M. A., Moore, G., Valdimarsson, H., Torres, D. J., Erofeeva, S. Y., and Nilsen, J. E. Ø. (2013). Revised circulation scheme north of the denmark strait. *Deep Sea Research Part I: Oceanographic Research Papers*, 79:20–39.

Villar, E., Farrant, G. K., Follows, M., Garczarek, L., Speich, S., Audic, S., Bittner, L., Blanke, B., Brum, J. R., Brunet, C., et al. (2015). Environmental characteristics of agulhas rings affect interocean plankton transport. *Science*, 348(6237):1261447.

Von Appen, W.-j., Mastropole, D., Pickart, R. S., and Girton, J. B. (2016). On the Nature of the Mesoscale Variability in Denmark Strait.

Waterhouse, A. F., MacKinnon, J. A., Nash, J. D., Alford, M. H., Kunze, E., Simmons, H. L., Polzin, K. L., St. Laurent, L. C., Sun, O. M., Pinkel, R., Talley, L. D., Whalen, C. B., Huussen, T. N., Carter, G. S., Fer, I., Waterman, S., Naveira Garabato, A. C., Sanford, T. B., and Lee, C. M. (2014). Global Patterns of Diapycnal Mixing from Measurements of the Turbulent Dissipation Rate. *J. Phys. Oceanogr.*, 44(7):1854–1872.

Whitehead, J., Leetmaa, A., and Knox, R. (1974). Rotating hydraulics of strait and sill flows†. *Geophysical and Astrophysical Fluid Dynamics*, 6(2):101–125.

Wunsch, C. and Ferrari, R. (2004). Vertical mixing, energy, and the general circulation of the oceans. *Annu. Rev. Fluid Mech.*, 36:281–314.

Xie, X., Liu, Q., Shang, X., Chen, G., and Wang, D. (2016). Poleward propagation of parametric subharmonic instability-induced inertial waves. *J. Geophys. Res.*, 121(3):1881–1895.

Yang, J. and Pratt, L. J. (2014). Some Dynamical Constraints on Upstream Pathways of the Denmark Strait Overflow. *Journal of Physical Oceanography*, 44(12):3033–3053.

Yang, J. and Price, J. F. (2000). Water-mass formation and potential vorticity balance in an abyssal ocean circulation. *Journal of Marine Research*, 58:789–808.

Yang, J. and Price, J. F. (2007). Potential Vorticity Constraint on the Flow between Two Basins. *Journal of Physical Oceanography*, 37:2251–2266.

Young, W. R. and Jelloul, M. B. (1997). Propagation of near-inertial oscillations through a geostrophic flow. *Journal of marine research*, 55(4):735–766.

Young, W. R., Tsang, Y.-K., and Balmforth, N. J. (2008). Near-inertial parametric subharmonic instability. *J. Fluid Mech.*, 607:25–49.

université PARIS-SACLAY

ÉCOLE DOCTORALE
Sciences mécaniques et énergétiques, matériaux et géosciences (SMEMAG)

Titre : Influence des ondes océaniques sur le mélange des eaux profondes et la circulation grande-échelle

Mots clés : ondes internes, ondes de Kelvin, ondes topographique de Rossby, mélange profond, courant de débordement

Résumé : Les différents projets présentés dans cette thèse contribuent à la compréhension de plusieurs aspects clés de la circulation océanique. Le premier aspect que nous étudions porte sur les processus physiques à l'origine du mélange lié à la marée; deux processus ont été mis en évidence. Depuis la latitude critique vers l'équateur, la marée interne transfert son énergie à des ondes plus petite échelle via des instabilités triadiques résonnantes impliquant les ondes proche inertielles. Depuis la latitude critique vers le pôle, les ondes de marée interne continuent de transférer leur énergie à des ondes plus petite échelle, mais étonnamment ce transfert se fait entre la marée interne et des ondes évanescentes. Dans la deuxième étude, nous étudions l'effet d'un courant moyen sur la propagation et la dissipation des ondes de marée interne, générées à la topographie dans des simulations haute résolution. Dans ce cas, la dépendance en latitude de la dissipation de la marée interne est plus lisse et plus proche d'une constante. Ce changement de la dépendance en latitude peut être lié au décalage des fréquences des ondes de marée interne par effet Doppler, ce qui induit la génération d'ondes secondaires plus petite échelle. Dans la troisième étude, nous étudions l'effet d'une perturbation générée en amont sur la circulation dans le bassin amont dû à l'interaction entre la perturbation et un seuil hydrauliquement contrôlé. Les ondes de Kelvin et topographiques de Rossby, générées par une variation de l'afflux d'eau dans le bassin amont, perturbent l'écoulement au dessus du seuil et ainsi l'export d'eau. Cette perturbation est due à la réfraction des ondes sur le seuil à chaque passage, une fois qu'elles ont fait le tour du bassin amont.

Title : Impact of oceanic waves on deep waters mixing and large-scale circulation

Keywords : Internal waves, Kelvin waves, topographic Rossby waves, overflow

Abstract : The various projects presented in this thesis contribute to our understanding of various key aspects of the oceanic circulation. The first aspect that we investigate is the physical processes responsible for this tidal mixing, and we identify two processes. Equatorward of the critical latitude, internal tides transfer their energy to smaller-scale waves via triadic resonant instabilities involving near-inertial waves. Poleward of the critical latitude, internal tides still transfer energy to smaller-scale waves, but surprisingly this transfer takes place between the internal tide and evanescent waves. In the second study, we investigate the effect of a mean current on the propagation and the dissipation of internal tides generated at the topography in high-resolution simulations. In that case, the latitudinal dependence of the tidal energy dissipation is found to be smoother and closer to a constant. This change in the latitudinal dependence can be linked to the Doppler shift of the frequency of the internal tides, which impacts the generation of smaller-scale secondary waves. In the third study, we study the effect of an upstream disturbance on the upstream circulation by interaction with a hydraulically controlled sill. The Kelvin and topographic Rossby waves, generated by a change in the upstream inflow, perturb the flow through the channel and hence the water export. This perturbation is due to the refraction of the waves at the sill at each passage, once they go around the upstream basin.

Université Paris-Saclay
Espace Technologique / Immeuble Discovery
Route de l'Orme aux Merisiers RD 128 / 91190 Saint-Aubin,
France